Delft University of Technology

Advancements in Large-Scale Volumetric PIV and PTV

Saredi, E.

DOI
10.4233/uuid:5fc6009a-d2dd-47d9-91d9-ca522d69f91d

Publication date
2023

Document Version
Final published version

Citation (APA)
Saredi, E. (2023). *Advancements in Large-Scale Volumetric PIV and PTV*. [Dissertation (TU Delft), Delft University of Technology]. https://doi.org/10.4233/uuid:5fc6009a-d2dd-47d9-91d9-ca522d69f91d

ADVANCEMENTS IN LARGE-SCALE VOLUMETRIC PIV AND PTV

ADVANCEMENTS IN LARGE-SCALE VOLUMETRIC PIV AND PTV

Dissertation

for the purpose of obtaining the degree of doctor
at Delft University of Technology,
by the authority of the Rector Magnificus Prof.dr.ir. T.H.J.J. van der Hagen,
Chair of the Board for Doctorates,
to be defended publicly on
Wednesday 14th June 2023 at 17:30 hours

by

Edoardo SAREDI

Master of Science in Aerospace Engineering,
Delft University of Technology, The Netherlands
born in Genova, Italy.

This dissertation has been approved by the *promotor* and *copromotor*

promotor: prof. dr. F. Scarano
copromotor: dr. A. Sciacchitano

Composition of the doctoral committee:

Rector Magnificus,	chairperson
Prof. dr. F. Scarano,	TU Delft
Dr. A. Sciacchitano,	TU Delft
Independent members:	
Prof. Dr. S. Discetti,	University Carlos III de Madrid
Assoc. Prof. Dr. D.E. Rival,	Queen's University
Dr. R.P. Stevens,	Alpine F1 Team
Dr. D. Schanz,	German Aerospace Center
Prof. Dr. Ir. J. Westerweel,	TU Delft
Reserve member:	
Prof. Dr. Ir. C.J. Simão Ferreira,	TU Delft

Keywords: Quantitative flow visualization, Particle Image Velocimetry, low-speed aerodynamics, outlier detection, data assimilation.
Printed by: Uitgeverij U2pi- Den Haag, Nederland.
Front & Back: designed by author. Back created from "Wanderer above the Sea of Fog". Caspar David Friedrich, Public domain, via Wikimedia Commons.

ISBN 978-94-6384-456-7

CONTENTS

SUMMARY

Particle Image Velocimetry (PIV) is considered nowadays the state-of-the-art for non-intrusive and quantitative 3D velocity measurements. Its ability to measure the velocity field around complex geometries is a valuable tool that engineers can exploit for aerodynamic design optimization in various domains, such as aerospace, wind turbines and automotive, among others. Despite recent advancements, performing a PIV measurement in the industrial environment remains challenging due to several reasons: achieving large-scale measurements, complex geometries and high Reynolds numbers.

The introduction of helium-filled soap bubbles, new Lagrangian Particle Tracking (LPT) algorithms and Robotic Volumetric PIV has allowed for the measurement of large-scale volumes around complex geometries. However, despite the described advancements, large-scale PIV and LPT measurements for industrial aerodynamics require further development to accelerate their applications.

The first bottleneck considered is the maximum measurable velocity. For aerodynamic flows in the transport sector, the velocity is often larger than 50 m/s when considering aircraft and race cars. To apply the mentioned techniques, acquisition frequencies higher than the one commonly available are needed. The double-frame timing strategy, characterized by image pairs with a small time separation, is detrimental to the measurement accuracy, especially when low-aperture systems, such as Robotic Volumetric PIV, are considered. This research has led to the development of novel acquisition strategies (chapters 3 and 4) that improve the accuracy of double-frame velocity measurements suited for high-speed applications ($U_\infty > 50$ m/s).

Another current topic of research concerns the detection of data outliers in PIV measurements, which affect their reliability and trustfulness. In this thesis (chapter 5) a novel approach to outliers detection from time-averaged three-dimensional PIV data is introduced. The principle invokes the physical mechanism of turbulence transport and is based on the agreement of the measured data to the turbulent kinetic energy (TKE) transport equation. The application of this new criterium to several experimental databases shows that spurious data can be detected more easily and unambiguously as an outlier along with a low fraction of false positives.

This research also attempts to decrease the gap between Computational Fluid Dynamics' (CFD) and experiments' aerodynamic data. In chapter 6, the application of PIV data for data assimilation is discussed. Data assimilation is a discipline in which observation and numerical or theoretical models are combined. This can be performed with two possible aims: improving the observation with physics-based models or increasing the capability of the model to represent reality. In this thesis, the latter is considered. A novel state observer technique is investigated for the assimilation of three-dimensional velocity measurements into computational fluid dynamics simulations based on Reynolds-averaged Navier–Stokes (RANS) equations. The state observer approach locally forces the solution to comply with the reference value, with increasing benefits when the density of forced points, or forcing density, is increased.

SAMENVATTING

Particle Image Velocimetry (PIV) wordt tegenwoordig beschouwd als de state-of-the-art voor niet-opdringerige en kwantitatieve 3D-snelheidsmetingen. Het vermogen om het snelheidsveld rond complexe geometrieën te meten, is een waardevol hulpmiddel dat ingenieurs kunnen gebruiken voor aerodynamische ontwerpoptimalisatie in verschillende domeinen, zoals onder andere ruimtevaart, windturbines en auto's. Ondanks de recente vooruitgang blijft het uitvoeren van een PIV-meting in de industriële omgeving om verschillende redenen een uitdaging: het uitvoeren van grootschalige metingen, complexe geometrieën en hoge Reynoldsgetallen.

De introductie van met helium gevulde zeepbellen, nieuwe Lagrangian Particle Tracking algoritmen en Robotic Volumetric PIV hebben het mogelijk gemaakt om grootschalige volumes rond complexe geometrieën. Ondanks de beschreven vorderingen moeten grootschalige PIV- en PTV-metingen voor industriële aerodynamica echter verder worden ontwikkeld om hun toepassingen te versnellen.

Het eerste knelpunt dat wordt overwogen, is de maximaal meetbare snelheid. Voor aerodynamische stromingen in de transportsector is de snelheid vaak groter dan 50 m/s wanneer het gaat om vliegtuigen en raceauto's. Om de genoemde technieken toe te passen, zijn acquisitiefrequenties nodig die hoger zijn dan de algemeen beschikbare. De timingstrategie met dubbel frame, gekenmerkt door beeldparen met een kleine tijdsafstand, is nadelig voor de meetnauwkeurigheid, vooral bij systemen met een laag diafragma, zoals Robotic Volumetric PIV. Dit onderzoek heeft geleid tot de ontwikkeling van nieuwe acquisitiestrategieën (hoofdstukken 3 en 4) die de nauwkeurigheid verbeteren van dubbel-frame snelheidsmetingen die geschikt zijn voor snelle toepassingen ($U_\infty > 50\text{m/s}$).

Een ander actueel onderzoeksonderwerp betreft de detectie van gegevensuitschieters in PIV-metingen, die hun betrouwbaarheid en betrouwbaarheid beïnvloeden. In dit proefschrift (hoofdstuk 5) wordt een nieuwe benadering geïn-

troduceerd voor het detecteren van uitschieters uit tijdgemiddelde driedimensionale PIV-gegevens. Het principe beroept zich op het fysische mechanisme van turbulentietransport en is gebaseerd op de overeenstemming van de gemeten gegevens met de turbulente kinetische energie (TKE) transportvergelijking. De toepassing van dit nieuwe criterium op verschillende experimentele databases toont aan dat valse gegevens gemakkelijker en ondubbelzinnig kunnen worden opgespoord als een uitschieter, samen met een laag percentage fout-positieven.

Dit onderzoek probeert ook de kloof tussen de aerodynamische gegevens van CFD's en experimenten te verkleinen. In hoofdstuk 6 wordt de toepassing van PIV-data voor data-assimilatie besproken. Data-assimilatie is een discipline waarin observatie en numerieke of theoretische modellen worden gecombineerd. Dit kan worden uitgevoerd met twee mogelijke doelen: het verbeteren van de waarneming met op fysica gebaseerde modellen of het vergroten van het vermogen van het model om de werkelijkheid weer te geven. In dit proefschrift wordt aan dat laatste gedacht. Een nieuwe toestandswaarnemertechniek wordt onderzocht voor de assimilatie van driedimensionale snelheidsmetingen in computationele vloeistofdynamica-simulaties op basis van Reynolds-gemiddelde Navier-Stokes (RANS)-vergelijkingen. De toestandswaarnemerbenadering dwingt de oplossing lokaal om te voldoen aan de referentiewaarde, met toenemende voordelen wanneer de dichtheid van geforceerde punten, of forceerdichtheid, wordt verhoogd.

ACKNOWLEDGEMENTS

This thesis marks the end (maybe for now, who knows?) of my academic path. It is the summary of all the work that I have done in the last five years, the work that I accomplished thanks to the help of several people. In this section, I intend to thank them all for their support. The first thanks go to my supervisory team: Fulvio, Andrea and Robbie. Fulvio and Andrea, I consider myself really lucky to have worked with you all these years. I enjoyed every day in the lab, learning from you, following your suggestions and debating openly about how to proceed with the research. I really hope to work together in the future. Speaking about the future (which is more of a present while I am writing this) I really have to thank the remaining member of my supervisory team, Robbie. Without your trust and esteem, I would not have had the opportunity to perform this PhD. You have been a source of inspiration since my internship. I am sure you will continue having this role in the future. During these years, I really enjoyed working in the High-Speed Laboratories of TU Delft. As many people know (I repeated this statement several times, sorry for that) I felt really at home inside those walls. Part of this feeling comes also from the people I had the luck to work with within those rooms. Firstly, I would like to thank all the staff of the laboratories: Colette, Frits, Henk-Jan, Peter, Dennis, Nico and Stefan. Several times I came to your office asking if I could ask a quick question (several times they were actually more than one) and you were always ready to help. My PhD colleagues have been for sure a mainstay of my nice time at Delft. Our lunch debates on every possible subject, sometimes really politically correct, sometimes a bit less will remain a vivid and amazing memory. I will never forget the hours, days actually, spent in the wind tunnels together trying to understand why something was not working. A lot of stressful moments, but definitely a lot of laughs. Alessandro, Alex, Ata, Babak, Beto, Christoph, Constantin, Gabriel, Giulio, Giulia, Haris, Jane, Jordi, Kherlen, Kushal, Luis, Ming, Mohamed, Sagar, Tiago, Thomas, Tyler, Varun, Xiadong, Yi, Wencan, Zeno, thank you really. We will see each other all at the first concert of Ata. Home sweet home, they say. It could not be more true in my case. After changing one house per year, during my PhD, I have finally found my safe harbour, shared with a group of amazing people: Arunnino and Diana, Fra and Angies. Thank you for all the nice moments we lived together, hoping to share even more in the future (India, here we come!). This period in Delft also gave me the possibility to meet a group of people that is now a fundamental part of my life. The fact that we see each other every year, even if we are spread around Europe, is a symbol of the relationship that was born in these years. I have been really lucky to share part of this path with you. Among this group, one person stems, Bea. I must thank you for the support you have always given me along this path, even if we are thousands of km apart. I cannot count all the times you spurred me when I was reluctant to write (my worst enemy, writing). Thank you for everything, really. Speaking about writing, I must thank also those who helped me with this dissertation, checking the quality of my writing style (low as you know) and giving plenty of suggestions on how to improve it. So, merci beaucoup Fio, je ne sais pas comment te remercier assez. Finally, I must thank the people who supported me even before Delft. Lu and G, the sister and the brother I always wanted and my roots in Genova. All of this would have not been possible without the constant support from my parents. I am really lucky to be your son and I hope to demonstrate daily how much I admire you. The last lines are dedicated to the ones who left us while I was walking this path. Giovanni, Mariuccia, and Piera, this thesis is dedicated to you. What can I say nonno? A Saredi is defending a PhD? É proprio Repubblica oggi.

1

INTRODUCTION

1.1. BACKGROUND

Paris, 1873. The French novelist Jules Verne is publishing one of the most iconic books ever written, "Around the World in Eighty Days". In this fictional novel, the main character, the wealthy English gentleman Phileas Fogg gets involved in an argument at the gentlemen club, the Reform Club, where he spends his days. He is convinced that it is possible to travel around the Earth in only eighty days. He is ready to gamble half of his fortune over this bet. From that moment his journey starts and it will end exactly 80 days later, seeing the gentlemen winning the bet against the skeptical colleagues of the club. Even if this was based on the imagination of the author, Verne paid attention to how he described a plausible scenario, considering the available transport methods of that time. The adventures described in the book inspired several people to attempt a trip similar to Fogg's. One of them was Nellie Bly, who only sixteen years later performed the same trip described in the book and came back to the starting point on the seventy-second day. This success proved that Verne's prediction was not too wrong after all. And nowadays? How long would it take for a traveller to perform a voyage around the world? Of course between Verne's and our current world, the means of transport have changed drastically. Within the last century, the speed at which the common person travels has increased dramatically. Carriages, horses and steamboats have been replaced by high-speed trains, reliable cars and intercontinental flights. If today we would plan a trip around the Earth, the latter would be the best option. Considering that the circumference of the Earth is around ≈ 40000 km at the equator and a cruise speed of 1000 km/h for a common commercial airplane, our trip would last only 2 days, 26 times faster than Nellie Bly. A step in this direction is surely the introduction of the direct flight between London and Sydney announced by the airline Qantas and operative from 2025. Passengers will be able to travel between these two cities with a single direct flight of approximately 20 hours.

This long travel achievement derives from the tremendous progress that has been made in science and technology in the last century. One of the sectors that

Figure 1.1: Portrait of the development performed in the last century in different fields. A large stake in this development comes from aerodynamic studies.

have been developed the most is aerospace, which spawned entire industries such as road transport, aviation and energy production through the exploitation of wind power. A considerable portion of this progress stems from advancements in fluid dynamics, more specifically in aerodynamics. Figure 1.1 presents a portrait of the evolution of the design in the mentioned fields. Race cars, airplanes and wind turbines have changed their shape following the dictates of aerodynamic researchers and engineers. Researcher objectives change depending on the considered sector: race cars have to be faster and safer; airplanes have to become more efficient and wind turbines need to be upscaled to deliver more and more energy. The tools that researchers and engineers can use to perform aerodynamic research and development are very diverse and will be discussed in the next section.

1.2. THE TOOLS FOR THE AERODYNAMIC DEVELOPMENT

Let's consider for instance the case of F1 race cars. In order to progress and reach the designs shown in figure 1.1 (top), engineers can exploit three different sources of data: full-scale real-life tests, computer-based modelling, using computational fluid dynamics (CFD), and scaled wind tunnel experiments. A representation of the three methodologies is presented in figure 1.2. The results obtained by these methodologies are then used to maximize the performance of the car, by increasing the vertical force, referred to as downforce. This allows the car to drive through the corners faster while decreasing the aerodynamic drag, which slows the car down in a straight line. All three approaches have their advantages and drawbacks, briefly presented and discussed in the next sections.

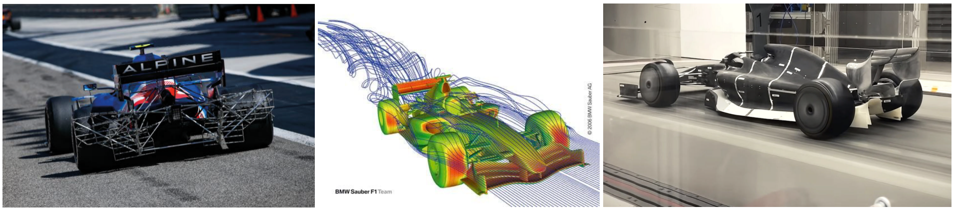

Figure 1.2: The three different sources of data available to engineers and researchers: (from left to right) track tests; numerical simulations; wind tunnel measurements.

FULL-SCALE TESTING

The first approach, the full-scale test, gives the highest level of realism since there is neither modelling nor scaling assumptions involved. Despite this advantage, they are not suited for the design phase due to the high cost of production of the full-scale parts and the difficult integration of the measurement devices in an in-situ experiment. Field tests are usually performed when the geometry definition comes to a final stage, where only a few options have to be evaluated. Furthermore, data achieved with this method are compared to those obtained by the other two sources of data, in order to evaluate their ability to reproduce real scenarios.

COMPUTER BASED MODELLING

In CFD simulations, the Navier-Stokes (N-S) equations, which govern the flow behaviour, are discretized and then solved in the volume of interest. Several methodologies which perform these calculations have been developed to date. The most common rely on the partition of the volume of interest in small elements where the flow quantities of interest (velocity, pressure, density, etc) are calculated. The computational cost of these calculations depends heavily on the required level of detail. For race-car aerodynamics, as for many other industrial applications, the high Reynolds number and the complex geometries do not allow the spatio-temporal treatment of the flow, a methodology known as direct numerical simulation (DNS). For this reason, simplifications are needed. The most common approach, aiming at the time-averaged flow properties, relies on the complete modelling of turbulence. This resolves only for the large scales of the flow field. The latter approach is called Reynolds-averaged N-S (RANS) solution. Due to their low computation cost, RANS simulations are considered to be the workhorse for aerodynamic engineering for many years to come (Xiao, Cinnella, 2019). The described numerical simulations allow for a versatile exploration of the design space, with multiple geometries evaluated at the same time. Furthermore, the availability of dense information in terms of variables gives the opportunity for engineers to look at the complete picture of what is happening in the volume of interest. The increased computational power of modern calculators led to the idea that CFD would have become the only tool needed to perform aerodynamic development. A notable case is that of the F1 team Manor. In 2010 they decided to rely only on CFD to aerodynamically develop the car. The car never scored a point and the team ranked last in that year's championship. However, the assumptions needed for resolving the equations reduce the fidelity level of the obtained results. For this reason, experimental data, obtained either in a field test or in a wind tunnel, are needed in order to calibrate the parameters of the models employed.

WIND TUNNEL MEASUREMENTS

Another possibility to acquire experimental data is performing wind tunnel experiments. Contrarily to track tests, wind tunnel measurements have the characteristic that the environment and the operating conditions are precisely controlled. In wind tunnels, a (usually scaled) model of the geometry of interest is operated to investigate its aerodynamic behaviour putting in motion the flow around it. Several techniques have been developed to investigate the aerodynamic performances of the model. These spanned from direct force measurements to more complex optical techniques for flow diagnostics. In the next sections, a survey on the available techniques is presented.

FROM FORCE MEASUREMENTS TO FLOW VISUALIZATION AND OPTICAL DIAGNOSTICS

A primary objective of aerodynamic research is to evaluate the forces acting on the body. A direct measurement is the most traditional, yet very common approach. However, direct measurements of the forces alone do not provide information about the physical behaviour of the flow and the phenomena that generate those forces. For this reason, researchers have pointed their attention to studying the flow around the model, trying to identify the most relevant quantities. The simplest experimental approach is flow visualization (Merzkirch, 2012). Among these techniques, the most common ones are the recording of smoke streaklines and the imaging of oil patterns on the surface. Examples of this approach are shown in figure 1.3. Their analysis allows the identification of coherent structures or large scales phenomena, such as flow separation and flow transition.

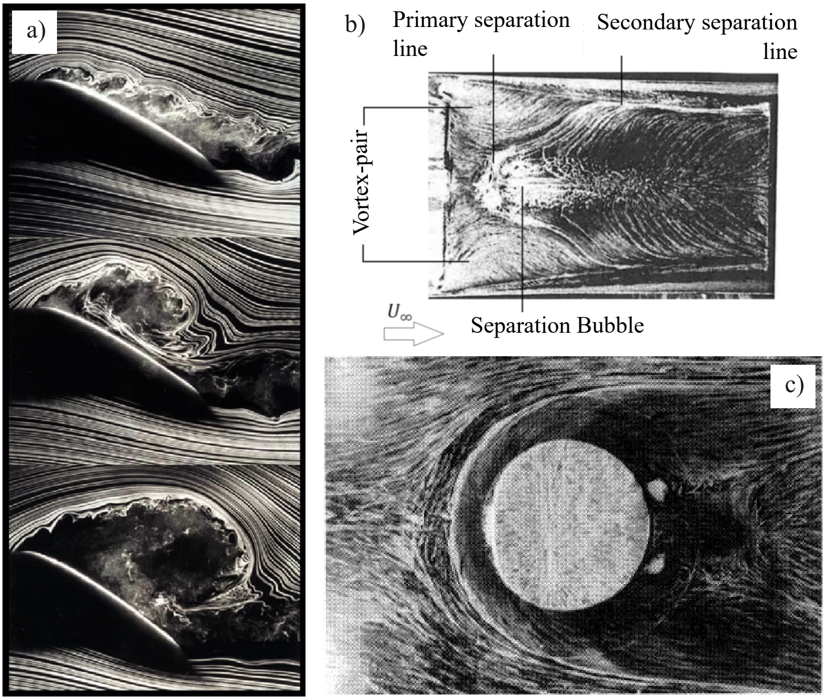

Figure 1.3: Example of flow visualization: a) dynamic stall on an airfoil pitching (Schreck, Robinson, 2007); b) Oil flow patterns on the diffuser ramp surface in maximum downforce configuration (Ehirim et al., 2019); c) horse-shoe vortex effect in the flow around a cylinder stemming from the ground (measurement by N. Hölscher, Ruhr-Universitat Bochum).

The mere visualization, however, even if insightful, is often not sufficient when a quantitative characterization of the underlying aerodynamic phenomena is needed. To fill this gap, several techniques have been devised in the last century that allow the quantitative measurement of different flow properties, such as flow pressure, temperature and most importantly flow velocity. Among these quantities, the availability of a full-field description of the velocity field can be depicted as the desired outcome, since it is the most frequent variable in the N-S equations.

A first distinction among quantitative measurement techniques can be done between intrusive and non-intrusive ones. Among the former, pitot-tube probes and hot-wire anemometry are the most common choices (Tropea et al., 2007). They deliver a pointwise measurement of the velocity field with a relatively low setup complexity. Their main shortcomings are the limited directional information and their inadequacy to detect flow reversal. Furthermore, the effect of their placement in the flow field can generate unpredictable interferences of the measured flow field. Laser Doppler velocimetry (LDV, Yeh, Cummins, 1964) overcomes this limitation and does not require the insertion of a physical probe in the flow field. LDV is able to perform 1D, 2D and 3D point measurements of velocity at high frequency. The main shortcoming of LDV is the high complexity of both the setup and operation, factors that limited its spread in the industrial environment.

QUANTITATIVE FLOW VISUALIZATION

As mentioned before, a key aspect of aerodynamics measurements is the ability to measure a large portion, if not the entire, of the volume of interest. In regards to this, all three mentioned experimental techniques are able to measure the velocity field only at a single point. In the case of pitot tubes, multiple sensors can be mounted in a complex array, but still suffer from limited spatial resolution due to the appearance of reciprocal interference when placed too close to each other.

The advent of Particle Image Velocimetry (PIV) has allowed researchers and engineers to perform full-field, non-intrusive, velocity measurements. Since its appearance, several developments and advancements have been presented, allowing PIV to be applied not only in a research laboratory but also in industrial facilities. This transition usually brings an increase in requirements in terms of both measured volume and flow speed, as described by Cardano et al. (2008) when analysing its application in the automotive environment. The developments needed to fulfil some of these new requirements will be the object of this dissertation.

1.3. PARTICLE IMAGE VELOCIMETRY

Particle Image Velocimetry is an optical, quantitative and non-intrusive field measurement technique based on the imaging of particle tracers, embedded in the flow. The terminology *particle image velocimetry* appears for the first time in Adrian (1984) and it is considered a development of the older *laser speckle velocimetry* introduced by Meynart (1983). At its introduction, PIV was used to evaluate two velocity components on a planar domain. Further developments have allowed increasing the range of measurability, both in terms of dimension, moving from a planar (2D) to a volumetric (3D) domain, from two to three velocity components and allowing the measurement of fast temporal variations of the velocity field. Textbooks that cover the subject are due to Raffel et al. (2018) and Adrian, Westerweel (2011). Even before discussing the required elements and the working principle of PIV, a schematic representation of the available PIV systems and their capability is presented in figure 1.4. The working principle of this technique, the classical 2D approach, is here examined. Figure 1.5 briefly shows the setup for a PIV recording. The main elements of such a system are:

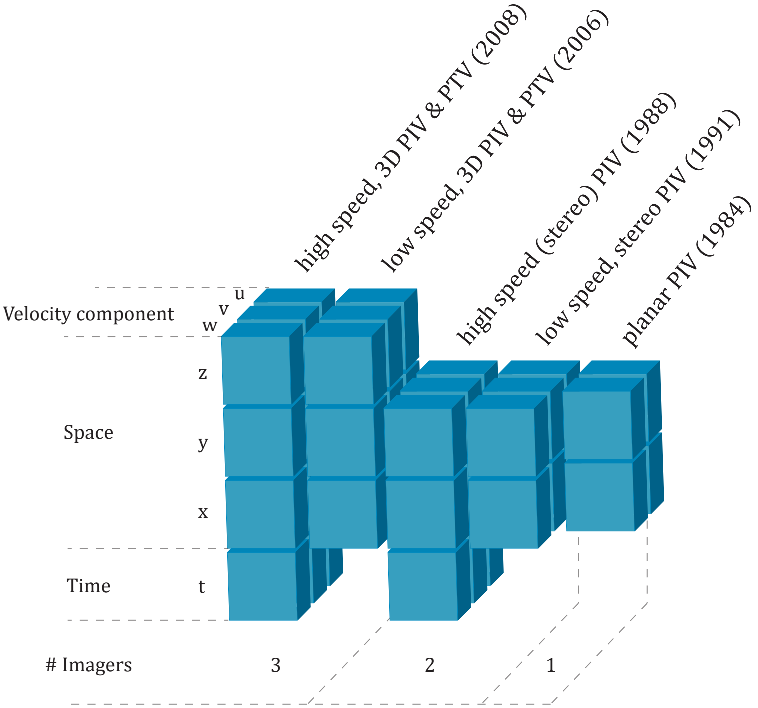

Figure 1.4: Illustrative description of PIV systems requirement in terms of imagers versus the number of measured components. In order of time appearance: Adrian (1984), Vogel, Lauterborn (1988), Arroyo, Greated (1991), Elsinga et al. (2006) and Schröder et al. (2008). The illustration is adapter from Hinsch (1995), Scarano (2013) and Jux (2022).

.

- light source, commonly a pulsed laser, lately LEDs;

- seeding particles, which allow to "see" the flow and whose nature varies depending on the application and the fluid of interest;
- imaging setup by means of electronic imagers (CCD or CMOS) and a system of lenses for the imaging hardware;
- data processing based on image cross-correlation or particle image pursuit (tracking);

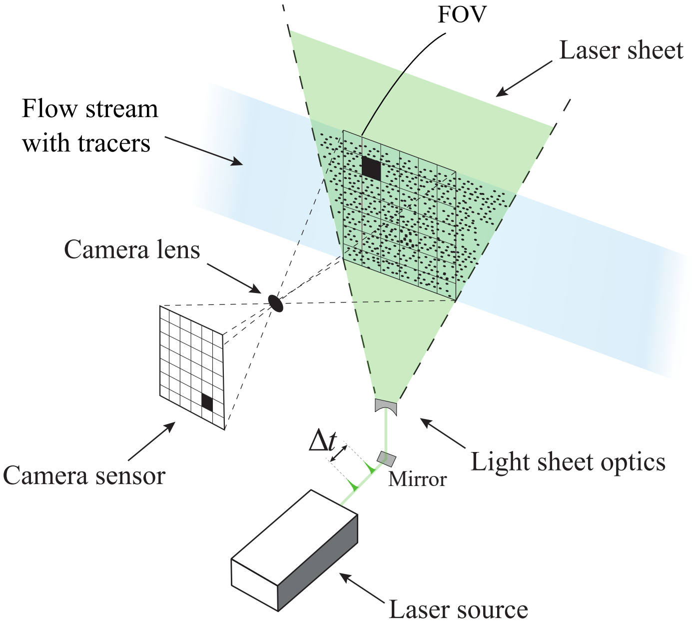

Figure 1.5: Schematic representation of the classical setup of a planar PIV (2D-2C) experiment.

The operating principle can be described as follows: tracers, usually micron-sized particles, are inserted in the flow in a location and modality which minimize flow disturbance, usually in the settling chamber if the test is performed in a wind tunnel. The region of interest is then illuminated by the light source at two or more subsequent time instants. The illumination strategy is a key factor for a PIV experiment since its feasibility and accuracy vary according to the chosen strategy. A more detailed analysis of the available time strategies is presented in chapter 2, while further advancements are presented in chapters 3 and 4. The light scattered by the particles is then captured by the imaging system, formed by one or more cameras. Through computer processing, the evaluation of the motion of the particle between two subsequent frames is performed and the flow velocity is obtained. The described setup allows the evaluation of two components (2C) in a two-dimensional domain (2D). PIV is not free from errors, which can be catalogued in bias and random. False velocity vectors are defined as outliers and need to be detected and excluded. How to individuate them is still, nowadays, a field of research. Further descriptions of the state-of-the-art techniques for outlier detection are given in section 1.7.

A popular approach to quantify the level of precision achieved by a PIV experiment is by evaluating the dynamic velocity range DVR, defined by Adrian (1997) as:

$$\mathrm{DVR} = \frac{U_{max}}{U_{min}} \tag{1.1}$$

where U_{max} is the maximum measured velocity and U_{min} is the minimum measurable velocity fluctuation that can be distinguished by the noise level. Its determination and how to increment it will be a core topic of this thesis. While the working principle has remained unaltered since the introduction of PIV, several developments have increased both the measurable velocity components and the dimension of the region of interest.

Among them, the first worth mentioning is the application of the stereoscopic principle to PIV measurements, which allowed the evaluation of the out-of-plane component (*stereoscopic-PIV* by Arroyo, Greated, 1991; Willert, 1997; Soloff et al., 1997 and Prasad, 2000). Since its introduction, this technique has been applied to several different kinds of scenarios, such as: boundary layers studies (Barros, Christensen, 2014; Alvarez, Christensen, 2013), bluff body wakes investigations (Grandemange et al., 2012; Spoelstra et al., 2019) and turbomachinery (Li et al., 2019; Wein et al., 2020). Figure 1.6 shows an example of application of stereo PIV by Spoelstra et al. (2019). The authors employed the 2D-3C PIV to evaluate the streamwise velocity component, which is then used to determine the drag of an on-site running cyclist through the application of the control volume approach. Several developments have been presented for both planar and

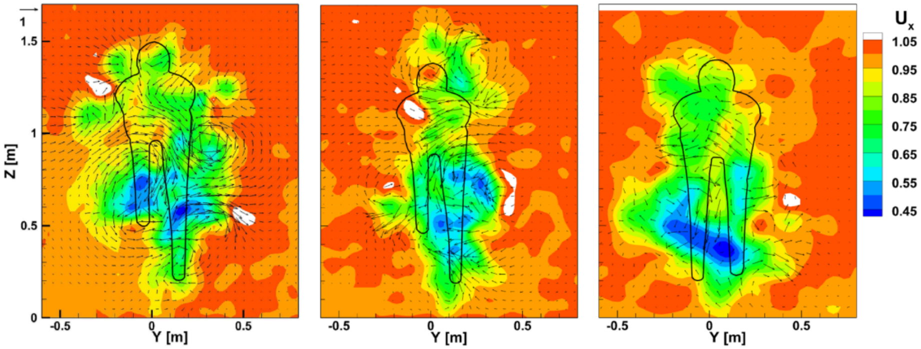

Figure 1.6: Example of the use of stereo PIV reproduced from Spoelstra et al. (2019). The three figures show the normalized instantaneous streamwise velocity captured at the back of a cyclist at different positions. In their work, this information was used by the authors to perform on-site drag measurements applying the control volume approach.

stereo PIV but they are still nowadays limited to measuring the velocity field in a thin 2D measurement plane. For the majority of engineering applications, the flow is characterized by complex 3D patterns and phenomena that can be fully investigated using a 3D-3C version of PIV.

1.4. VOLUMETRIC PARTICLE IMAGE VELOCIMETRY

In the last decades, several approaches to obtaining optical 3D-3C measurement techniques have been presented. In the works of Arroyo, Hinsch (2007) and Brücker (1997) the main strategies used at the beginning of the 2000s are reviewed. Three methodologies are identified: three-dimensional particle tracking velocimetry (3D PTV; Maas et al., 1993), scanning light-sheet PIV (SLS; Brücker, 1995), and multi-plane stereo PIV (Kähler, Kompenhans, 2000). Shortly later, another technique has been presented: tomographic PIV by Elsinga et al. (2006). An in-depth analysis of all these techniques is out of scope in this work, however, their main concepts are described here.

THREE-DIMENSIONAL PTV

Three-dimensional PTV relies on the same concept as 2D PTV: instead of evaluating the cross-correlation on a group of particles through the windowing, each of the tracers is followed along with the frames. In order to be able to perform the

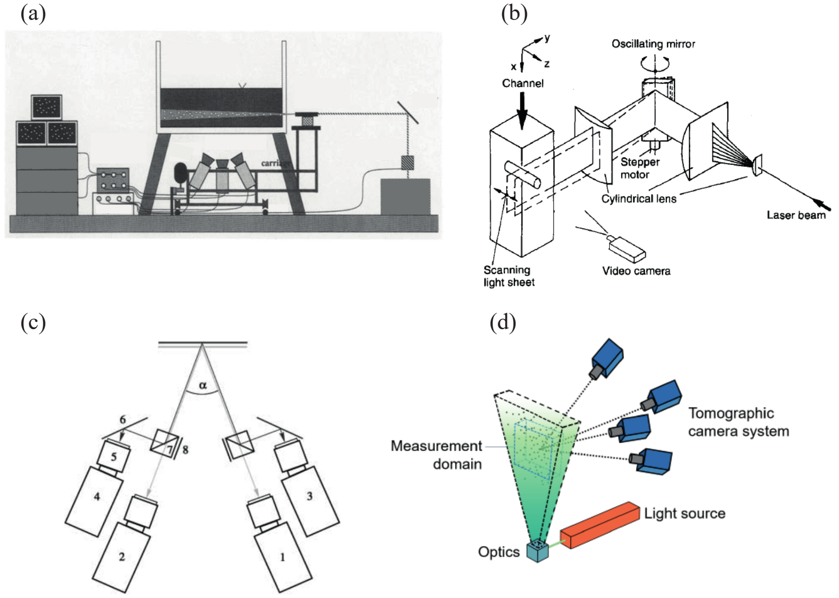

Figure 1.7: Panel with the illustration of the setup of: (a) 3D PTV (Maas et al., 1993); (b) scanning PIV (Brücker, 1995); (c) multi-plane stereo PIV (d) tomographic PIV (Elsinga et al., 2006).

particle pairing, particle detection and triangulation has to be performed. In the work of Maas et al. (1993) particle triangulation is performed from the views of three cameras and approximately 1000 particles could be unambiguously identified and tracked. The limitation of this technique is the maximum particle density achievable, 0.001 particles per pixel (ppp), which translates into 1000 particles imaged into 10^6 pixels, which limits the maximum spatial resolution.

SCANNING LIGHT-SHEET PIV

Scanning light-sheet PIV, introduced by Brücker (1995) as a time-resolved technique, relies on the idea of performing 2D measurements on several different planes very close to each other by shifting the laser light sheet by rotating or galvanometric scanning mirrors, as shown in figure 1.7, top-right. The methodology was proven by analyzing the flow around a finite cylinder at a Reynolds number of 300 in a water channel. Due to the time needed to shift the laser sheet, of the order of tens of milliseconds, its application is limited to relatively low-speed flows (1-10 cm/s), where the times scales involved are higher than the time needed to scan the volume.

MULTI-PLANE STEREO PIV

Multi-plane stereo PIV comes as the natural evolution of the stereo PIV presented the decade before. Its working principle relies on the idea of illuminating several adjacent planes with multiple stereo-PIV systems. To enforce optical separation between the light scattered by the different planes, polarization or different wavelengths can be employed. Due to the small distance between two subsequent planes, the normal velocity gradient can be calculated, overcoming the main limitation of the standard stereo-PIV.

The main drawbacks of this method are the high requirements in terms of hardware (for each plane an entire stereo setup is needed) and the high level of precision required for the calibration procedure, due to the small distance between the measurement planes. The concept of slicing the volume of interest with different measurements has also been employed in cases where the time resolution was not a concern. Cardano et al. (2008), Nakagawa et al. (2016) and Mead et al. (2015) are examples where this approach has been employed.

The development of tomographic PIV by Elsinga et al. (2006) can be seen as the real breakthrough to fully 3D instantaneous velocity measurements. Adopting known concepts from medical tomography, the particle spatial distribution is reconstructed starting from multiple 2D views acquired with 3 or more cameras, with a setup similar to the one shown in figure 1.7, bottom-right. Once the volumetric reconstructed light distribution is obtained for each time instant, 3D cross-correlation is then employed to obtain the 3D-3C velocity field. This technique allowed for measurement with a larger volume of interest and higher resolution compared to the other introduced 3D methods. An extensive review of the tomographic approach can be found in Scarano (2013).

Figure 1.8 presents two results obtained respectively by scanning stereo-PIV (Nakagawa et al., 2016) and tomographic PIV (Scarano, Poelma, 2009). In the former, authors investigated the effects of aerodynamic spoilers on the near-wake of a 28% CFRP model, a benchmark geometry for passenger cars. A traversing

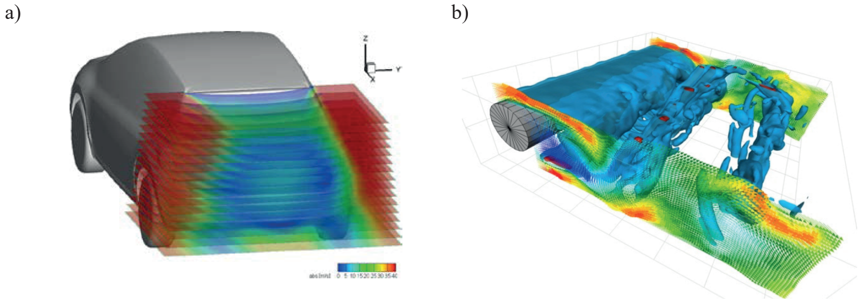

Figure 1.8: Example of application of techniques able to measure the velocity field in a volume: (left) scanning-PIV (Nakagawa et al., 2016) and (right) tomographic PIV (Scarano, Poelma, 2009).

system allowed measuring sequentially several planes with a planar PIV setup. The scanning approach allows obtaining a picture of the entire wake of the car, as visible in figure 1.8 (left), but suffers from two main drawbacks: the impossibility of measuring the entire wake instantaneously and the limited resolution in the direction perpendicular to the measurement plane that limits the capability in terms of gradient calculation. The tomographic approach, applied in the latter study, overcomes these two limitations, by being able to measure the entire 3D flow field instantaneously, as shown in figure 1.8 (right).

While tomographic PIV has been considered after its presentation as the state-of-the-art volumetric PIV technique, some limitations still limit its use, such as:

- The complexity of the setup and the lengthy calibration procedures
- The high requirements in terms of processing time and computer memory
- The maximum achievable measurement volume

Regarding these points, researchers have proposed different solutions, which are presented in the following sections.

1.5. COMPACT VOLUMETRIC SYSTEMS

Given the complexity of the setup of the techniques presented in the previous section, several techniques based on a more compact system or the use of single cameras have been presented, such as holographic PIV (J. Zhang et al., 1997;

Sheng et al., 2008), defocusing PTV (Cierpka et al., 2010), plenoptic PIV (Lynch et al., 2012) and coaxial volumetric velocimetry (Schneiders et al., 2018).

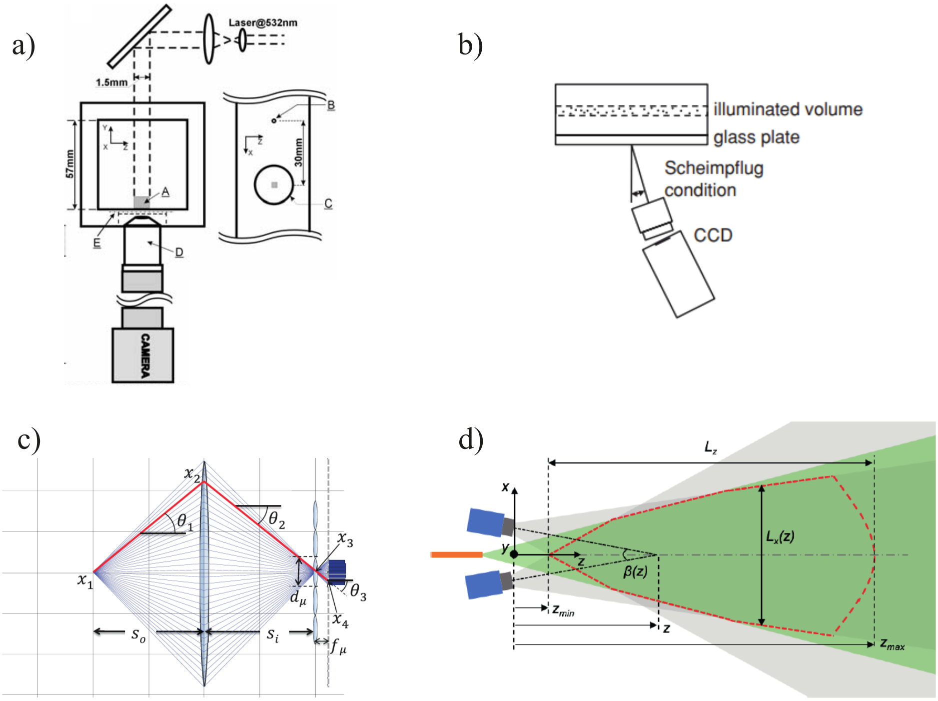

Figure 1.9: Panel with the illustration of the setup of: (a) holographic PIV (Sheng et al., 2008); (b) defocusing PTV (Cierpka et al., 2010); (c) plenoptic PIV (Lynch et al., 2012); (d) coaxial volumetric velocimetry (Schneiders et al., 2018).

The holographic PIV (HPIV) principle is based on the interference of coherent light scattered by a particle with a reference beam. The interference allows the encoding of the amplitude and the phase of the scattered light onto a sensor plane. The measured encoding, or hologram, is used to reconstruct the three-dimensional particle field. Based on the hologram's interaction with the reference beam, two different methodologies have been presented: in-line (Sheng et al., 2008) and off-axis (J. Zhang et al., 1997). Due to the lower sensor resolution requirement, the former is preferred, since digital cameras can be used instead of holographic films. The imaging and illumination setup of the experiment presented by Sheng et al. (2008) is shown in figure 1.7 (bottom-left). However, the resolution requirements preclude its use in all but small-scale laboratory scenarios, even if the application of advanced digital filtering to the standard holographic reconstruction has shown promising results in extending the measurement volume, as shown in Sun et al. (2020).

Another proposed approach to evaluate the flow in a 3D domain is referred to as general defocusing particle tracking (GDPT), in which the particle depth position is determined by looking at the defocusing patterns of the corresponding particle images in a single-camera setup. Several different methodologies have been developed along this line. Willert, Gharib (1992) proposed a three-pinhole mask to more efficiently read out the defocusing information to increase the accuracy in the in-depth direction. The radial intensity profiles of axisymmetric particle images have also been proposed (Z. Zhang, Menq, 2008; Loenhout et al., 2012). Finally, the astigmatic aberration, obtained by a cylindrical lens, has been exploited to obtain the particle depth position based on its characteristic elliptical shape (Cierpka, Kähler, 2012; Rossi, Kähler, 2014).

The application of plenoptic cameras to the PIV experiment has been investigated by Lynch et al. (2012) and is still nowadays an active area of research, as described by Fahringer et al. (2015). This kind of camera is able to store multiple views of the same scene, adding to the spatial distribution of light and also the angular one, allowing the 3D reconstruction. This ability is permitted by the addition of a microlens array placed in front of the image sensor, as the one shown in figure 1.9, top-right. The extension of this technique to a multi-camera system has been introduced by Jones et al. (2018) and has shown promising results in increasing the accuracy of the reconstructed light distribution.

Another approach to simplify the measurement setup has been presented by Schneiders et al. (2018) by the name of Coaxial Volumetric Velocimetry (CVV). The measurement system is derived from the concept of tomographic PIV, with multiple cameras imaging the measurement volume. The characteristics that differentiate this approach from the classical tomographic PIV are the compactness of the system, due to the small tomographic aperture between the cameras, and the coaxial arrangement of illumination and imaging, as shown in figure 1.9, bottom-right. This arrangement has then been used by Jux et al. (2018) to create the Robotic Volumetric PIV system.

As previously mentioned, the techniques described in this section present a lower setup complexity with respect to the 3D approaches presented previously. The cost of this complexity reduction, however, is the increase of the uncertainty in the velocity determination along the depth direction, a drawback shared by all the compact 3D methodologies. More specifically, while the uncertainty on the particle position determination along the in-plane components is proportional only to the particle image diameter d_τ (Adrian, 1984):

$$\varepsilon_x = \varepsilon_y = \frac{c_\tau d_\tau}{M} \tag{1.2}$$

the uncertainty along the coaxial component is dominated by the tomographic aperture β:

$$\varepsilon_z = \frac{2\varepsilon_x}{\beta} \tag{1.3}$$

where β represents the largest angle between cameras, as shown in Fig.1.9. In the previous equations, c_τ is a coefficient dependent on the methodology followed to detect the particle centroid with values varying between 0.1 and 0.2; M is the magnification factor.

As consequence, having in mind equation 1.1, when considering the coaxial component, a lower DVR is achieved. The exploitation of the expected time coherency for time-resolved measurement is a common strategy to limit the detrimental effect just described. The techniques described in the next section are an example of this approach.

1.6. LARGE SCALE PIV

In section 1.4, several limitations characteristic of Tomographic PIV were presented. One of them regards the maximum achievable measurement volume, typically limited to a size of a few hundred cubic centimetres (Scarano, 2013). Nowadays this limit has been overcome, as is testified by the work of Schröder et al. (2022), where the authors studied the airborne transport mechanisms of aerosol particles inside a room of approximately 12 m^3. This upscale of the measurement volume has been permitted by several distinct advancements:

1. the adoption of Helium-filled soap bubbles (HFSB) as flow tracers;

2. the development of efficient 3D Lagrangian Particle Tracking algorithms;
3. the introduction of Robotic Volumetric PIV, when considering flow statistics.

In the following part of this section, each of these advancements is presented.

HELIUM FILLED SOAP BUBBLES

The correct choice of seeding particles is a fundamental step in the design of a PIV experiment. Two aspects have to be addressed during this choice. Firstly, their dynamic behaviour: their mechanical properties affect their ability to follow the flow, which is crucial since the flow velocity is the quantity of interest. Secondly, their optical properties, which affect their ability to scatter enough light to the cameras to form bright images. A good compromise between the two mentioned aspects has to be achieved in order to perform correctly a PIV experiment.

In order to evaluate the dynamic behaviour of tracers, it is common practice to evaluate the time they need to adjust their velocity when they encounter any change in the flow velocity. This ability is quantified by the particle response time τ_p (Raffel et al., 2018). When considering small and spherical particles, their time response reads:

$$\tau_\mathrm{p} = \frac{d_\mathrm{p}^2}{18\mu_\mathrm{f}} \frac{\rho_\mathrm{p}}{\rho_\mathrm{f}} \tag{1.4}$$

The condition in which equation 1.4 is valid is called Stokes flow and it occurs when the force acting on the particle while moving inside the fluid is only of viscous nature, neglecting all the other effects given by buoyancy and gravity.

The acceptable value of τ_p varies based on the application in which the tracers are used. In order to evaluate if a tracer will follow the flow with enough fidelity it is a common approach to calculate the Stokes number, defined as:

$$S_k = \frac{\tau_\mathrm{p}}{\tau_\mathrm{f}} \tag{1.5}$$

where τ_f is a characteristic time of the considered flow. Tracers are considered appropriate when $S_k < 0.1$.

Considering equation 1.4, since both μ_f and ρ_f are characteristic of the fluid, it becomes clear that to reduce τ_p two strategies are available: opting for smaller particles (lower d_p) or selecting neutrally buoyant particles. This condition is achieved when the particle density is approximately equal to the fluid density ($\rho_\text{p} \approx \rho_\text{f}$).

While the latter condition is commonly achievable when PIV is applied to liquid fluids (e.g. water), when considering air flows, this requirement is far more difficult to meet. In order to balance the difference in density, commonly, tracers with a small diameter ($d_\text{p} \approx 1\mu$m) have been employed. Among the possible solutions, it is worth mentioning oil or DEHS (Di-ethyl-hexyl-sebacate) droplets and metal powders (e.g. Alumina or Titania) can also be used. The drawback of this approach is the reduction of the light scattered by the particles which is proportional to the particle diameter d_p. This has been one of the major limiting factors in the development of PIV for large-scale applications.

In the last decade, helium-filled soap bubbles (HFSB) have emerged as neutrally buoyant particles suitable for air flows. The neutrally buoyant condition is achieved thanks to the balance between the internal gas, helium, which is lighter than air, and the thin layer of soap that forms the external wall of the bubble, which is heavier than air. Faleiros et al. (2018) reported, for bubbles with a diameter $d_\text{p} = 550\ \mu$m, a density equal to $\rho_\text{p} = 1.1 \pm 0.05$ Kg/m^3, confirming the neutrally buoyant assumption at atmospheric conditions. Their response time have been reported by Faleiros et al. (2018) as $\tau_\text{p} = 30 \pm 20\ \mu$s and by Scarano et al. (2015a) as $\tau_\text{p} = 20 \pm 10\ \mu$s.

As previously mentioned, the diameter of the tracer also affects the amount of light scattered. The larger the tracer, the more light will be scattered and vice versa. Being PIV based on the recording of the movement of these tracers, a good signal-to-noise ratio between the scattered light and the background is a requirement for a good successful measurement. For an in-depth focus on this topic, more interested readers are referred to Melling (1997), who performed an extensive study on the optical characteristics of tracers.

The importance of the scattering intensity achieved by a tracer increases even more when a 3D measurement is considered. This effect is caused by two main factors: the increase of the $f_\#$ (f-stop, the ratio between the focal length f and the lens aperture diameter D) and the decrease of light intensity proportional to the dimensions of the measurement volume. While the latter is straightforward due to the fixed amount of energy produced by the illuminator, the former is here explained in more detail.

To record correctly the particles illuminated in the volume, the depth of focus δz has to be greater or equal to the depth of the measurement volume Δz, with the former that can be estimated with the following approximation:

$$\delta z = 2 f_{\#} d_{\mathrm{diff}} (M+1)/M^2 \tag{1.6}$$

Furthermore, when the particle image is diffraction limited, also its diameter d_{diff} is proportional to $f_{\#}$, following the relation:

$$d_{\mathrm{diff}} = 2.44 f_{\#} (M+1) \lambda \tag{1.7}$$

where the λ is the wavelength of the incident light. Combining equation 1.6 and equation 1.7 it is obtained that the focal depth is proportional to $f_{\#}^2$. Furthermore, the light that passes through the lens is actually limited and proportional to $f_{\#}^{-2}$. Combining the two previous expressions, the following proportionality between depth of focus and light intensity can be derived:

$$I \propto \delta z^{-4} \tag{1.8}$$

From the latter, the importance of high-efficiency scattering tracers for 3D experiments comes clear. This further justifies the usage of helium-filled soap bubbles for this purpose.

The production of the helium-filled soap bubbles is usually achieved by an orifice-type, coaxial nozzle, whose initial design was presented by Bosbach et al. (2009). Figure 1.10 shows the cross-section of a typical generator and a shadowgraph image of a nozzle in a production regime.

As shown in figure 1.10, the three fluids have to be supplied to the nozzle in order to produce continuously bubbles. A fluid supply unit (FSU) is designed for this scope and Faleiros et al. (2019) studied the effects of different mass flows in terms of bubble production rate and bubble dimension. The results showed that

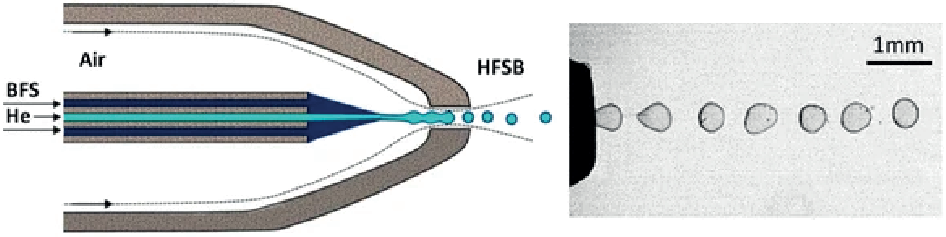

Figure 1.10: (Left) Schematic representation of the cross-section of a nozzle producing helium-filled soap bubbles. (Right) Shadowgraph of a working nozzle. Images reproduced from Faleiros et al. (2018).

a production rate between 10^4 and 7×10^4 bubbles/s can be achieved by varying the design and the operating conditions. Such a large number of bubbles however is usually not able to seed the measurement volume entirely. For this reason, multiple nozzles are operated together. Several different prototypes have been presented in the literature. The first system presented by Scarano et al. (2015b) was a piston–cylinder device where the HFSB were produced and accumulated into a chamber for 30 seconds and then ejected by the moving cylinder. The stream with air and bubbles was transported into the settling chamber where a group of orifices, mounted on an aerodynamic rake, was used to spread the tracers within a stream-tube. The original system inspired the adoption of different evolved designs, such as the ones mentioned by Faleiros (2021), with the producing nozzles directly integrated into the aerodynamic rake, or by Gibeau, Ghaemi (2018), where the producing nozzles were placed vertically and in serial to increase at will the seeding concentration.

PARTICLE TRACKING METHODS

Between the limitations of tomographic PIV presented in section 1.4, the requirements in terms of processing time and computer memory have been pointed to as the bottleneck for the further diffusion of the technique (Schanz et al., 2016). Two works that have allowed a noticeable improvement in this matter are the iterative particle reconstruction (IPR) presented by Wieneke (2013) and the Shake-The-Box algorithm presented by Schanz et al. (2016).

The reconstruction of the volumetric light distribution is a relatively expen-

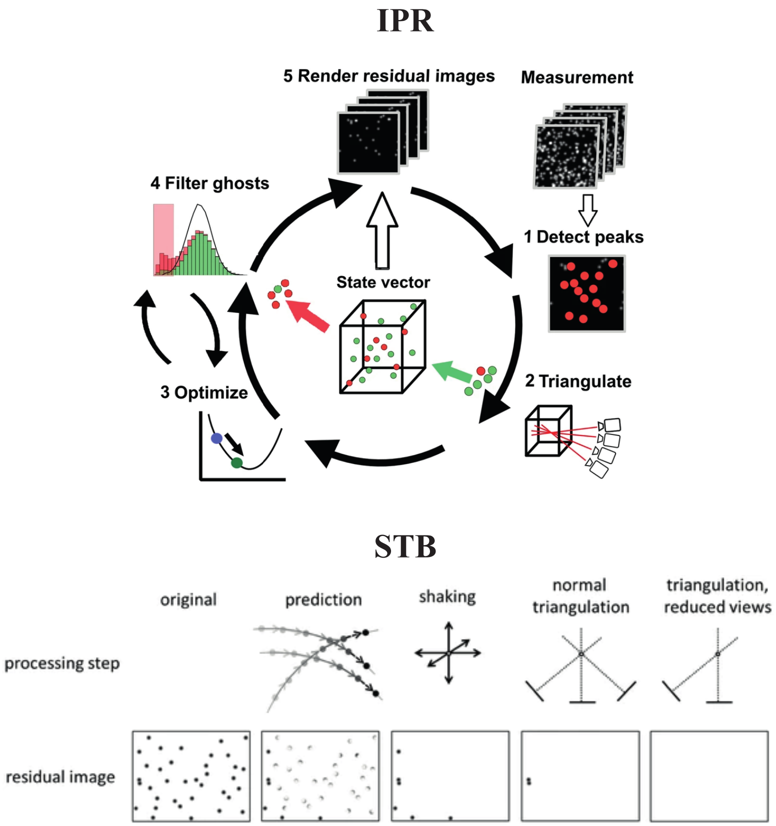

Figure 1.11: Graphical representation of the working principle of: (left) the latest version of IPR; (right) STB. Images reproduced from Jahn et al. (2021) and Schanz et al. (2016).

sive step for tomographic PIV (Scarano, 2013). The 3D-PTV approach previously described does not suffer from this drawback since only the particle position has to be determined.

The approach proposed by IPR allowed for overcoming this limitation. In his work, Wieneke (2013) demonstrated the ability of IPR to manage 5% particle per pixel (ppp), similar to that usually presented in tomographic PIV experiments.

The main concept behind IPR is the use of an iterative approach in which, after a first determination of the particle positions in real space through classical triangulation, the particles are reprojected onto the image planes and compared with the original images. The particle position is then optimized in order to minimize the difference between the reprojected images and the raw images. This further optimization step increases the accuracy of the particle location determination and increases the maximum particle density allowed (Jahn et al., 2021).

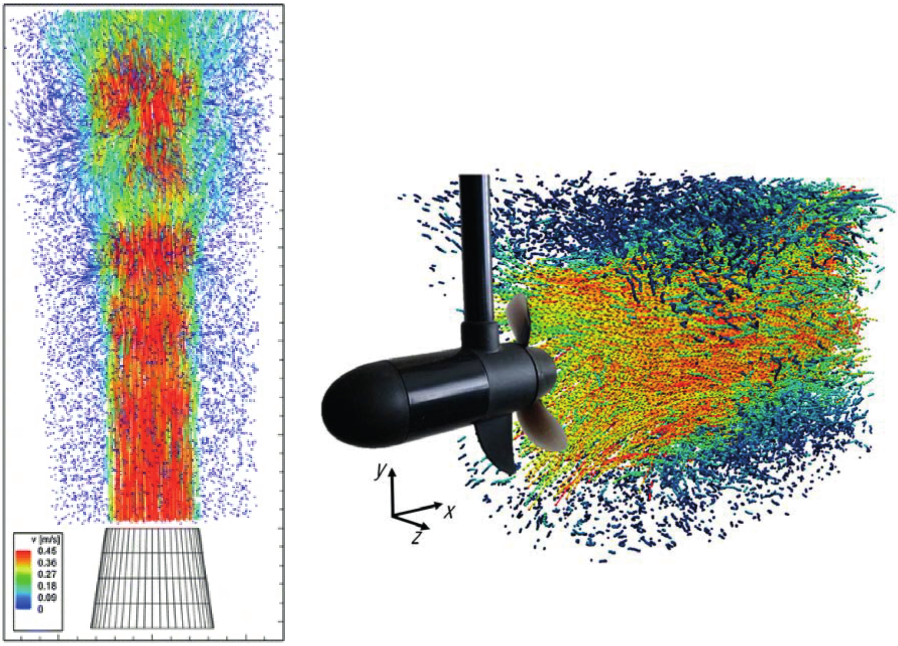

Figure 1.12: Particle tracks obtained by STB in different scenarios: circular jet flow (Schanz et al., 2016); flow around a propeller (from LaVision GmbH website); near wake of a cubic object (Schröder et al., 2020).

The ability of IPR to work with high particle density has been further exploited by the tracking algorithm Shake-The-Box, which permits to perform a robust particle tracking when time-resolved images are available. A panel of results of STB across a wide gamut of scenarios is proposed in figure 1.12. Due to the prediction step, where the history of the particle motion is used to strengthen the particle location determination, the application of the original version of STB is limited to time-resolved datasets. This characteristic limits the applicability of this algorithm in terms of measurable velocities, usually around 30 m/s with the commonly available hardware. A possible solution to overcome this limitation is the adoption of new timing strategies, such as the four-pulses approach proposed by Novara et al. (2016). These types of approaches are discussed more in-depth in chapter 4.

ROBOTIC VOLUMETRIC PIV

Even when using HFSB, illuminating and imaging a volume of $\sim O(\mathrm{m}^3)$ in combination with the presence of complex geometries is not straightforward. As seen in the previous section, the light scattered by the particles reduces with the increase of the measurement volume. This effect limits the maximum achievable measurement volume with a single illuminator. Furthermore, even when the light intensity is enough to illuminate such a big volume, the maximum ppp resolvable by the modern tracking algorithms remains limited to 0.15 and this poses a hard limit on the maximum achievable particle density. Finally, the presence of complex geometries, often non-transparent, forces the use of multiple acquisition and illumination devices, with an increase in both the cost and complexity of the setup.

The introduction of Robotic Volumetric PIV (Jux et al., 2018) has permitted to perform measurements of flow statistics around complex shapes in a such large measurement volume. This technique relies on the combination of the coaxial volumetric velocimetry (Schneiders et al., 2018), described in section 1.5, and robotic manipulation. Its main principle is depicted in figure 1.13.

The entire measurement domain is divided into subvolumes, each measured subsequently by the coaxial velocimeter. The robotic actuation allows moving from one volume to the next without the need for any calibration or imaging adjustment, decreasing the procedure's complexity. The technique has been applied successfully to study the flow around complex geometries, such as a full-scale cyclist (Jux et al., 2018), a full-scale isolated bicycle wheel (Jux, 2022), a gust-loaded wing (Mertens et al., 2022) and a swimmer's hand (Berg et al., 2021).

As presented in the previous section, the drawback of such an arrangement for imaging devices is the low tomographic aperture. It causes a detriment in the

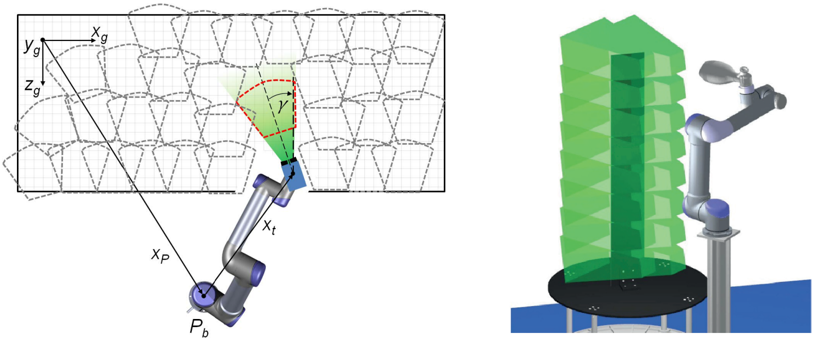

Figure 1.13: (Left) Illustration of the working principle of robotic volumetric PIV (Jux et al., 2018). (Right) Practical example of the application of the principle: the flow around a flexible structure is investigated by merging the data obtained by several volumes scanning the entire measurement domain (Mitrotta et al., 2022).

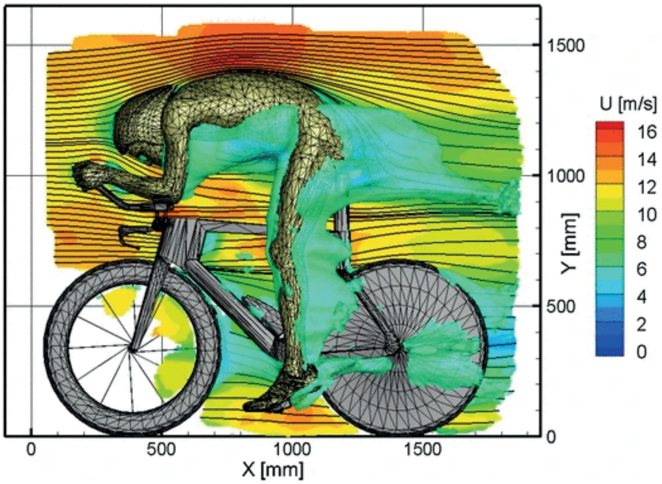

Figure 1.14: Examples of the application of Robotic Volumetric PIV on a full-scale cyclist (Jux et al., 2018).

in-depth accuracy of particle location, which leads to a decrease in the maximum achievable DVR. The use of the time resolution by applying STB can limit this effect and has been applied in all the mentioned examples. However, this solution is only applicable when the flow velocity is low enough to allow time-resolved measurement. This limits the use of the technique to relatively low flow veloci-

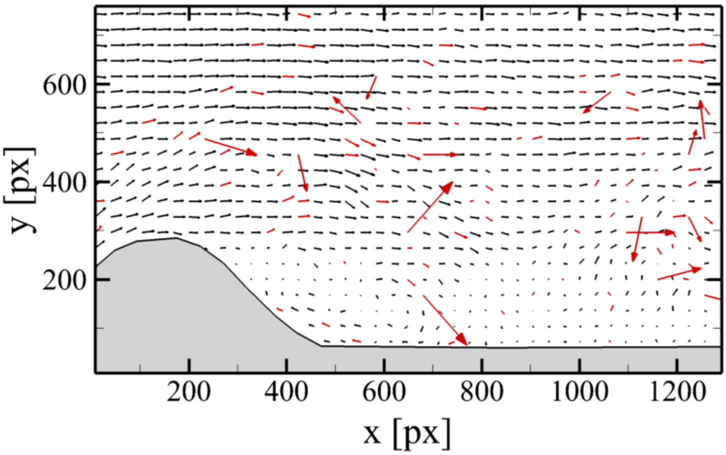

Figure 1.15: Velocity field affected by the presence of outliers (red vectors). Their algorithmic identification is still a field of research in PIV. Figure reproduced from Sciacchitano (2014).

ties, typically below 30 ∼ 40 m/s, depending on the available hardware components.

1.7. THE PROBLEMS OF OUTLIERS IN PIV

Any measurement technique is prone to errors, which can be of random or biased nature. In the previous sections, several PIV methodologies have been presented, based either on cross-correlation or particle tracking. The results obtained by both approaches can present outliers, defined as spurious velocity vectors that exhibit large unphysical variations in magnitude and direction from neighbouring valid vectors (Westerweel, 1994). Their identification is a crucial part of the experimental process, which justifies the research of further advancement in this topic.

Among the factors leading to the occurrence of an outlier, there are light reflections from solid surfaces or background, poor illumination, shadow regions, inhomogeneous flow seeding, inadequate image recording and interrogation (Hart, 2000; Lazar et al., 2010; Sciacchitano, 2019; among others). Most methods presented in the literature focus on the detection of outliers in the instantaneous flow field (Higham et al., 2016) and the state-of-the-art approach is based on the universal outlier detection (UOD, Westerweel, Scarano, 2005), which generalises the median detector presented earlier by Westerweel (1994). Duncan et al. (2010) further extended the UOD approach for unstructured data such as those obtained by Particle Tracking Velocimetry (PTV) or spatially adaptive interrogation algorithms. Masullo, Theunissen (2016) dealt with the relevant problem of clusters of false vectors and proposed to combine a spatial coherence estimator with a Gaussian-weighted distance-based averaging median.

Proper orthogonal decomposition (POD) has also been considered as a basis to detect outliers (Wang et al., 2015; Higham et al., 2016), using the difference between a low-order reconstruction and the measured flow field as an indicator of the presence of outliers in the instantaneous snapshots. The latter approach was also proven effective in detecting clustered outliers, compared to the UOD.

Despite all the presented advancements, UOD remains nowadays the most applied outlier detection method due to its low level of complexity. After the advent of 3D measurements, UOD has been easily upgraded to cope with the third dimension, being even implemented in commercial softwares. However, the growing availability of 3D measurements opens scenarios in which constitutive equations are used to detect the presence of outliers. For this reason, part of the research presented in this thesis will explore this direction of development.

1.8. PIV DATA ASSIMILATION FOR CFD

In this section, the use of PIV data as ground truth for improving computer simulation, a procedure referred to as data assimilation, is discussed.

The advances in computational fluid dynamics (CFD) coupled with the increasingly affordable computational power have made CFD one of the main tools for aerodynamic study and design optimization for industrial problems (Xiao, Cinnella, 2019). The computational cost of high-fidelity simulations (i.e. LES, DNS), instead, remains relatively high for their use in optimization studies, especially for high Reynolds number flows. As a result, CFD analysis makes most often use of the simplified approach offered by the Reynolds-averaged Navier-Stokes (RANS) formulation (Argyropoulos, Markatos, 2015; Ferziger et al., 2020).

Considered to be the workhorse in aerodynamic engineering for many years to come (Xiao, Cinnella, 2019), RANS solvers model the entire turbulent spectrum, achieving lower computational cost and higher robustness with respect to mentioned higher fidelity models. The cost of the amount of required modelling is the aforementioned lower accuracy (Davidson, Peng, 2003). Several sources of uncertainty are presented in literature; those stemming from the choice of the turbulence model and its parameter, nowadays based mainly on expert judgment, are reported to often dominate the overall uncertainty of the simulation (Xiao, Cinnella, 2019).

Conversely, the experimental approach offers accurate measurements, directly from scaled models. When flow quantities are obtained such as velocity or pressure, the measurements usually suffer from limited spatial range and spatiotemporal resolution. For this reason, it should be retained in mind that a single experiment is often insufficient for the analysis of the flow problem, which renders the simulations necessary for a complete description of the aerodynamic behaviour.

Experimental data is often used a-posteriori, to verify the validity of a given simulation, or more specifically, the adequacy of turbulence models parameters, also referred to as “calibration” (Duraisamy et al., 2019; Da Ronch et al., 2020). The latter approach is often iterative and several simulations are conducted until model calibration is achieved. In order to overcome the above limitations, direct integration of experimental data within CFD simulations has been considered. The resulting process is called data assimilation (DA). This approach aims to produce a more accurate flow simulation, which is compliant with the data gathered during an experiment.

Originally introduced in the fields of meteorology and oceanography, as reviewed by Navon (2009), DA has seen a growing number of applications in fluid mechanics (Hayase, 2015). Among the DA methodologies presented in the literature, three main categories have emerged: variational methods (Foures et al., 2014; Symon et al., 2017; among others), Kalman filter (KF; Kalman, 1960; Kato et al., 2015) and state observer methods (reviewed in Hayase, 2015).

Variational methods are based on the application of optimal control theory to find the minimum of the error function between the simulation and a reference, herein represented by the experimental data. The calculation of the adjoint and the need to solve an optimization problem entails a relatively large computational cost. KF and state observer techniques are sequential algorithms, which means that the result of the previous iteration is used at each following iteration. The solution of the assimilated simulation is expected to asymptotically converge to the reference along the simulation (Hayase, 2015). A comparison between a variational method and a KF application can be found in Mons et al. (2016).

If the equations of state observer and KF are compared, a certain similarity can be noted (Utkin et al., 2017). KF can be considered a type of state observer method too, but designed for stochastic systems, while state observer techniques are typically applied to deterministic systems. While in a deterministic system, the variables of interest are represented by a scalar or a vector at each point, in a stochastic system they are represented by probability density functions, with a correspondent mean and standard deviation. Between the three of them, state observer methods require both a computational cost and an implementation effort that are significantly lower compared to variational methods, making them attractive for aerodynamic design and optimization (Hayase, 2015).

2

THESIS OBJECTIVES AND OUTLINE

2.1. VELOCITY RANGE OF ROBOTIC VOLUMETRIC PIV

The introduction of Robotic Volumetric PIV, coupled with STB and the use of HFSB has opened the possibility of doing time-average PIV measurements at scales that reach or surpass meter scale; however, the introduction of these methods is relatively new and presents challenges for its applications.

The compact arrangement of the velocimeter features a very small tomographic aperture ($\beta = 8°$), with larger uncertainty along the coaxial direction. Time-resolved measurements can limit the effect of the lower DVR for the axial component, however, the use of a time series requires the rapid acquisition of images, such to track particles from one frame to another with a low risk of false pairing. This condition sets a limit on the resolvable flow velocity. With the current state-of-the-art hardware, both illumination and imaging, time-resolved measurement can be performed up to ~ 30 m/s. Even with future developments increasing such limits, the time-resolved strategy may always pose a limit on the measurable velocity.

In order to deploy this technique for flows of industrial interest, a new acquisition and processing approach is to be developed, in particular an acquisition strategy that enhances the measurement DVR for double-frame LPT measurements.

This limitation has driven the first part of the research proposed in this thesis. After having evaluated the performance of the standard double-frame single-exposure approach, the thesis builds upon that method by considering multi-step and multi-exposure approaches, with the aim to compensate for the effects due to the small tomographic aperture.

2.2. PHYSICS-INFORMED OUTLIER DETECTION FOR FLOW STATISTICS

As with every measurement method, PIV is not immune to errors. The sources of these errors are various and not always easily detectable. Reflections, uneven seeding, calibration errors, and out-of-plane particle motion (for 2D PIV) are among the most common sources of errors in PIV. Outliers are one of the possible forms of errors. Because they are large errors, which differ more than 100% from the true velocity vectors, they have a dramatic impact on the statistics. The presence of outliers has a twofold negative impact on the PIV results: it can lead to misinterpretation of the results and it can reduce the level of trustworthiness of the entire measurement campaign.

These effects are even more pronounced in an industrial environment where, in opposition to what is done in academia, the person that is looking at the PIV data is often not the same that was responsible to acquire and produce those data. For this reason, in order to affirm PIV as a reliable tool for aerodynamic development, a robust outlier detection scheme is needed. Until now, the state-of-art outlier detection method is an extension to 3D of a 2D method based on statistics of neighbours presented by (Westerweel, Scarano, 2005). A more in-depth description of the method is presented in 5. The availability of the third component, both in terms of spatial and velocity information, opens the possibility of the use of constitutive equations for the detection of outliers.

This has been the starting point of the research presented in this thesis on the detection of an outlier for 3D PIV results. Focus has been posed on understanding which fundamental equation better detects the presence of outliers and how to robustly employ them.

2.3. PIV DATA ASSIMILATION FOR CFD

As discussed in the previous chapter, experimental results are one of the three sources of information engineers can use during aerodynamic development. It becomes clear that the integration of all the sources is fundamental to achieving a streamlined and effective development cycle.

Several integration strategies have been presented in the literature, spanning from a simple comparison to the integration of measurement into a numerical simulation. Nowadays, PIV data are mainly used as a calibration tool for numerical simulation parameters. The availability of dense and reliable 3D measurements, achieved through the developments discussed in the previous sections, opens the possibility to study a new way of coupling measurements and simulations, with the first being included in the solving stage of the second, through the data assimilation process. Among all the available methodologies to perform data assimilation, state observer approaches have demonstrated their attractiveness due to their low computation cost and implementation complexity. The objective of the research performed on this topic is to develop a framework, based on the state observer concept, that uses 3D time-averaged experimental data to improve the accuracy of RANS simulations.

2.4. OUTLINE

Chapter 3 and **Chapter 4** introduce novel acquisition strategies aimed at increasing both the maximum measurable flow speed and the accuracy of the evaluated velocity field. After a theoretical explanation of the efficacy of the proposed methodology, both are tested on experimental and synthetic data.

Chapter 5 presents a novel methodology to perform outlier detection on time-averaged velocity data. The method is then applied to three different experimental datasets and its results are compared to the state-of-the-art technique of outlier detection in PIV.

Chapter 6 introduces a new data assimilation approach to enhance the accuracy of RANS simulations via the use of 3D-PIV data.

Chapter 7 summarizes the findings of the thesis and presents an outline of possible future developments.

3

MULTI-STEP DUAL TIMING FOR PTV

Parts of this chapter have been published in:

- Saredi, E, Sciacchitano, A & Scarano, F (2020) Multi-Δt 3D-PTV based on Reynolds decomposition. *Meas. Sci. Tech.* 31(8):084005

3.1. INTRODUCTION

As discussed in chapter 1, the introduction of Coaxial Volumetric Velocimetry (CVV, Schneiders et al., 2018), in combination with the use of helium-filled soap bubbles as flow tracers for large-scale measurements (Bosbach et al., 2009), has reduced some requirements of system calibration and optical access for three-dimensional flow measurements. When combined with robotic manipulation, CVV becomes suited to automated measurements over large volumes and around complex objects. Since CVV is based on the time resolved analysis of high-speed recordings of particle tracers' motion using STB (Schanz et al., 2016)), it requires high-speed PIV equipment. In the case of CVV measurements, presently, available compact CMOS cameras do not exceed 1,000 Hz, resulting in a maximum flow speed for measurements up to approximately 10 m/s.

Experiments at higher flow velocity are hampered by the above limitations unless based on dual-frame image recording (e.g. by frame-straddling), where image separation Δt is of the order of microseconds. This acquisition strategy however suffers from a limited achievable DVR due to the low particle displacement and the lack of time resolution. The DVR issue is exacerbated for CVV where the in-depth velocity component is about 10 times less accurate than the other two components due to the low tomographic aperture (Schneiders et al., 2018).

A method is investigated here to perform 3D-PTV analysis in double-frame mode and restore a DVR comparable to that achieved with time-resolved multi-frame techniques. The approaches reported in literature aiming at increasing the DVR of PIV either increase the maximum particle image displacement or decrease the minimum resolvable displacement. To enlarge the maximum resolvable displacement, Fincham, Delerce (2000) developed a multi-Δt approach on three-frame recordings separated by Δt and $2\Delta t$. Cross-correlation at separation Δt produces a predictor for the analysis at time separation $2\Delta t$. Multi-Δt acquisitions have been also used to quantify uncertainties (Nogueira et al., 2009 and Nogueira et al., 2011 for peak locking). Multi-Δt recordings analysis has been exploited by Scharnowski et al. (2019) to quantify flow turbulence intensity from PIV measurements. With the aim of increasing the DVR, Hain, Kähler (2007) and Persoons, O'Donovan (2010) have developed several multi-frame approaches for time-resolved recordings, where the time separation is locally optimized based on the flow conditions or the cross-correlation signal-to-noise ratio. Conversely, as far as the reduction of the minimum resolvable velocity is concerned, techniques of correlation averaging have proven to be effective. The pyramid correlation (Sciacchitano et al., 2012) further expands the method through a linear combination of correlation maps obtained at different time separations. Nonlinear motions were taken into account by Lynch, Scarano (2014) and later by Jeon et al. (2014) with a least-squares approach. For Particle Tracking Velocimetry (PTV), Cierpka et al. (2013) showed that the use of four or more time steps in combination with a multi-Δt image analysis greatly enhances a reliable particle pairing even with high levels of the seeding concentration. From the above discussion, it emerges that multi-frame approaches (recordings that encompass more than two snapshots) have been most pursued to increase the dynamic velocity range of PIV and PTV techniques. In the present chapter, we investigate the use of multi-step analysis of double-frame recordings making use of a variable time separation between exposures. The work focuses on the potential to increase the DVR of measurements and a specific discussion is made for low-aperture 3D-PTV systems like CVV and astigmatism PTV (Cierpka et al., 2011).

3.2. TWO-FRAME PARTICLE TRACKING PRINCIPLES

Particle tracking principles are amply discussed in the literature (Malik, Dracos, 1993; Pereira et al., 2006; amongst others). Here, fundamental definitions and properties are recalled for use in the discussion presented further. Let us consider particle tracers distributed in the physical space of coordinates X, Y, Z. When at uniform concentration C, the average distance λ between neighbouring particles, following Pereira et al. (2006), reads as:

$$\lambda = \sqrt[3]{\frac{3}{4\pi C}} \tag{3.1}$$

The nearest neighbour (NN) principle is arguably the simplest approach to pair subsequent images of a particle tracer. Considering a particle displacement $\mathbf{\Delta X}$ occurring between two subsequent frames with time separation Δt, the ratio $\gamma = |\mathbf{\Delta X}|/\lambda$ between the displacement and the mean particle distance determines the probability of obtaining a correct pairing between the two images of the same particle.

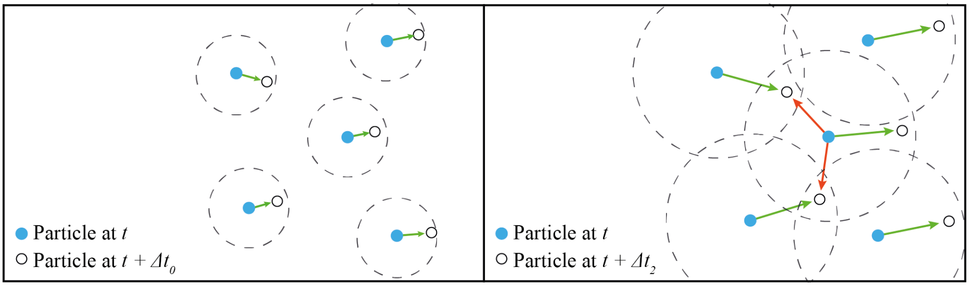

Figure 3.1: Particle images from double-frame recordings. Left: length travelled by particles between first and second exposure is smaller than the distance λ separating neighbouring particles ($\gamma < 1$). Right: particles displacement (green arrows) exceeds the inter-particle distance ($\gamma > 1$) and the search radius R_S includes more than one candidate for pairing.

A schematic illustration is given in figure 3.1, where the condition of $\gamma < 1$(left) yields a high probability of successful pairing. Conversely, when $\gamma > 1$ (right), the increased search region leads to false pairing when the NN principle is applied. The nearest neighbour algorithm is usually coupled with a condition of maximum search distance (Pereira et al., 2006), here referred to as search radius R_S. The above discussed condition for a high probability of correct detection translates into a relationship between the search radius and the average particle distance, more specifically:

$$|\mathbf{\Delta X}| < R_S < \lambda \tag{3.2}$$

Several criteria to optimize the choice of R_S are given in literature. Malik and Dracos (1993) proposed the following:

$$R_S = \frac{1}{3}\lambda \tag{3.3}$$

From the above, it can be concluded that choosing a particle displacement significantly smaller than the particle distance is a favourable condition to correct particle pairing. However, the accuracy of the instantaneous velocity measurement directly depends upon the length of the particle displacement. The dynamic velocity range, defined by equation 1.1, can be rewritten considering the characteristics of the optical setup used as (Adrian, 1997):

$$\mathrm{DVR} = \frac{M\,\Delta t\, V_{max}}{c_\tau\, d_\tau} \tag{3.4}$$

where the minimum measurable displacement is a function of the particle image diameter d_τ and the uncertainty c_τ of the particle image centroid position (Adrian, 1991). A theoretical limit for DVR can be formulated considering equations 3.2 and 3.4:

$$\mathrm{DVR}_0 = \frac{M\lambda}{c_\tau\, d_\tau} \tag{3.5}$$

Equation 3.5 expresses the trade-off between the DVR and the instantaneous tracers' concentration, through the parameter λ. As an illustration of the above, reference data on the probability of correct pairing using double-frame recordings with the nearest neighbour principle is obtained with a Monte Carlo simulation. In a volume $150 \times 30 \times 30$ mm^3, N = 50 particles are randomly distributed, resulting in the average concentration C = 0.4 particles/cm^3. From equation 3.1 the mean particle distance is λ = 8.6 mm. The relative displacement parameter γ is varied in the interval [0.01 - 2.75] by changing the particle displacement $\mathbf{\Delta X}$. Particles are paired with the nearest neighbour algorithm and the fraction of correct pairing η_p is evaluated. Statistical results are achieved by repeating the random simulation 10,000 times. For $\gamma < 0.2$, the correct pairing is higher than 99% (see the grey curve in figure 3.9-left). When $\gamma > 0.20$, false pairings start appearing. If the criterion prescribed by Malik, Dracos (1993) is chosen, $\gamma = 0.3$, the ratio of corrected pairings reads $\eta_p = 0.98$, in agreement with the results obtained by the latter authors. If we now assume $\sigma_s = c_\tau d_\tau = 0.1$ mm as the uncertainty of the particle displacement estimation, it follows that, for a displacement of 8 mm, DVR $\approx$ 80. However, for the given concentration of 0.4 particles/cm^3, the latter displacement corresponds to $\gamma = 1$, leading to a probability of false pairing of approximately 50%. Conversely, imposing a correct pairing probability of 98% leads to a value of $\gamma = 0.3$ and a corresponding DVR < 30. From this discussion, considering a given particle concentration, it comes clear that there is a fundamental limit in the trade-off between robustness and DVR. When robustness is guaranteed (figure 3.1-left) a lower DVR is returned, with particle displacement comparable to the particle diameter. A higher DVR (figure 3.1-right) comes at the cost of pairing reliability, unless the process makes use of a predictor for the particle displacement, as discussed in the next section.

3.2.1. PARTICLE PAIRING AIDED WITH A DISPLACEMENT PREDICTOR

The use of multi-step analysis of particle motion has been demonstrated to effectively improve the probability of correct pairing even at high concentrations of particles (Bastiaans et al., 2002; among others). The super-resolution method proposed by Keane et al. (1995) makes use of cross-correlation analysis to produce a predictor for the displacement of individual particles inside the interrogation window. Particle pairing is then obtained based on a nearest neighbour search in the second exposure at a position given by the predictor. For low image-density recordings typical of 3D PTV measurements, however, the cross-correlation approach becomes unsuited due to two main reasons:

1. the particle field is often represented in the physical space by their positions and not by voxel intensities;
2. with a large inter-particle distance, a low signal-to-noise ratio is expected.

Here, similarly to the super-resolution method, an estimator of the tracer velocity is considered based on a first level analysis that yields an estimation of the particles time-average velocity and expected level of fluctuations. This is based on the Reynolds decomposition of the local flow velocity:

$$\mathbf{V} = \overline{\mathbf{V}} + \mathbf{V}' \tag{3.6}$$

where the bold face indicates that the symbol represents a vector. The time average velocity $\overline{\mathbf{V}}$ is determined from the previous analysis performed at short time separation as detailed in the next section. Such time-average velocity is used to offset the search region by an amount corresponding to the local mean predicted displacement $\overline{\boldsymbol{\Delta X}}_{pred} = \overline{\boldsymbol{V}} \cdot \Delta t$. In the turbulent flow regime, the actual position of an individual tracer will not coincide with the position predicted with the time average. Let's define such discrepancy by the average positional disparity vector, which reads as:

$$\overline{\boldsymbol{\Delta}\mathbf{X}'} = \boldsymbol{\sigma}_{\mathbf{V}} \Delta t \tag{3.7}$$

where $\sigma_{\mathbf{V}}$ is the velocity standard deviation and Δt the pulse separation time. This way, the choice of the search radius R_S needs to account only for the expected fluctuations since the displacement due to the mean velocity is considered with the predictor. The search radius follows the relation:

$$R_S > |\overline{\mathbf{\Delta X'}}| \tag{3.8}$$

It is proposed more specifically that $R_S = 2|\overline{\mathbf{\Delta X'}}|$, corresponding to a confidence level of 95% when the fluctuations follow a Gaussian distribution. Since the second part of equation 3.2 is still valid also when a predictor is available, consequently, the use of a mean velocity predictor turns the restriction posed in equation 3.2 into:

$$|\overline{\mathbf{\Delta X'}}| < \lambda \tag{3.9}$$

As a result, for a given velocity field, the value of the time separation Δt can be increased by a factor $V_{max}/|\boldsymbol{\sigma}_{\boldsymbol{V}}|$ when a predictor for the mean displacement is available. Due to the velocity prediction, the occurrence of correct pairings is no anymore directly related to the particle displacement, but it is proportional to the ratio between the radius of search R_S and the mean particle distance λ. The dynamic range of a velocity measurement making use of a predictor, therefore, reads as:

$$\mathrm{DVR} = \frac{V_{max} M \lambda}{|\boldsymbol{\sigma}_{\boldsymbol{V}}| c_\tau d_\tau} \tag{3.10}$$

It can be concluded that making use of a predictor permits to increase the DVR according to:

$$\mathrm{DVR}_{pred} = \frac{V_{max}}{|\boldsymbol{\sigma}_{\boldsymbol{V}}|}\mathrm{DVR}_0 \tag{3.11}$$

with respect to the case of a single-step. As an illustration, if the method is used to measure a turbulent flow with fluctuations of the order of 10% of the maximum velocity, equation 3.11 indicates a potential order of magnitude increase of the velocity dynamic range. One should retain in mind, however, that the above analysis relies on a number of hypotheses: 1) the increase of time separation shall remain limited to the range where truncation errors are negligible with respect to random errors (Boillot, Prasad, 1996); 2) the operations that determine the mean velocity predictor (binning process discussed in section 3.3) are performed at a sufficient spatial resolution and with statistical convergence of the velocity and its fluctuations to reliably apply Reynolds decomposition. As shown by Hain, Kähler (2007), the truncation error appears in presence of acceleration in the flow. The truncation error scales with the square of the pulse separation time Δt when the velocity is evaluated with a central-difference scheme. This appears to be problematic along curved streamlines (radial acceleration) and when the flow rapidly decelerates or accelerates (tangential acceleration). Let us consider the former case within the core of a steady vortex, where the flow rotates like a rigid body. A relative error on the velocity magnitude due to truncation lower than 10% corresponds to a pulse separation time of $1/4T$, where T is the core turnover time. The flow vorticity ω is often monitored with PIV measurements ($T = 4\pi/\omega$); imposing a time separation one order of magnitude smaller than the reciprocal of the local flow vorticity can be seen as a conservative criterion to prevent that truncation errors affect the measurement accuracy.

3.3. MULTI-STEP ALGORITHM

The approach here presented relies on the acquisition of two or more sets of double-frame images with varying (increasing) pulse separation time. In this section, the case in which two sets are acquired is considered, with respectively pulse separation time Δt_0 and Δt_1, with $\Delta t_0 < \Delta t_1$. The analysis of the data at Δt_0 features high robustness but low precision and is used for a first estimate of time-averaged and fluctuating velocity with criteria defined in equations (3.1-3.5). These estimates are then used to aid the analysis at separation Δt_1.

The analysis of the dataset Δt_0 is described first: the 3D particle detection is based on the iterative particle detection algorithm (IPR, Wieneke, 2013). Particle pairs are determined by selecting the closest (in 3D space) particle between the two frames (nearest neighbour approach, Pereira et al., 2006). The search radius R_S here needs to account for the maximum expected particle displacement (equation 3.2). The result of this evaluation yields the instantaneous flow velocity. For each particle, the velocity vector is placed at the midpoint between the two positions. The time-averaged velocity field is reconstructed with the binning procedure as described by Agüera et al. (2016) : 1) all the velocity vectors pertaining to the series of recordings are combined into a single ensemble, which

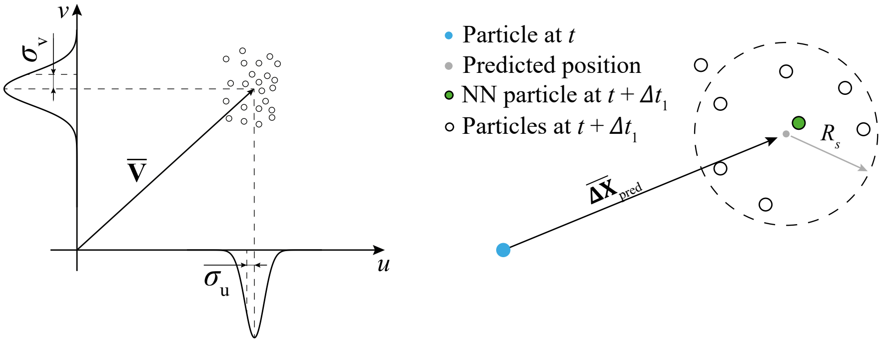

Figure 3.2: (left) Velocity samples collected in one bin, yielding the average velocity vector $\overline{V}$ and the standard deviation of its component σ_V of the velocity are evaluated. (right) Prediction of particle displacement based on the time-averaged velocity, search area based on R_S and particle pairing based on NN detection.

increases the spatial density of the velocity information; 2) the measurement volume is divided into sub-volumes (bins) with dimension $L_{bin} \sim O(10^{-2}\mathrm{m})$ arranged on a Cartesian grid. Similar to what is done in PIV image processing, overlap between adjacent bins (e.g. by 75%) decreases the distance between neighbouring vectors. The data captured inside a single bin features a cloud of velocity samples as a result of local turbulence and the measurement uncertainties (figure 3.2 - left). Performing the Reynolds decomposition (equation 3.6), one obtains the average displacement $\overline{\mathbf{\Delta X}_0}$ and its fluctuations $\overline{\mathbf{\Delta X}'_0}$. The latter is evaluated using equation 3.7 and the subscript is related to the fact that the quantities are obtained analysing images with time separation Δt_0.

In order to decrease the error due to unresolved velocity gradient, the velocity samples are weighted according to their distance with respect to the centroid of the bin. A Gaussian weighting function is applied, following the approach proposed by Agüera et al. (2016). The Gaussian is then centred in the bin center and has a standard deviation equal to half of the bin size. In the second stage, recordings acquired at a time separation $\Delta t_1 > \Delta t_0$ are interrogated making use of the above results. Also in this case, particle detection is performed using IPR, resulting in a cloud of particles for both exposures of all the recordings. Considering the particles triangulated in the first exposure, the time-averaged velocity field measured in the previous stage is interpolated at particle positions and the predicted displacement is calculated through a linear scaling (homothety) and reads as:

$$\overline{\mathbf{\Delta X}}_{pred} = \overline{\mathbf{\Delta X}}_0 \frac{\Delta t_1}{\Delta t_0} \tag{3.12}$$

Similarly, the choice of the search radius is locally determined based on the estimated level of velocity fluctuations:

$$R_S = 2|\overline{\mathbf{\Delta X}}'_0| \frac{\Delta t_1}{\Delta t_0} \tag{3.13}$$

In synthesis, both average displacement and the radius of search are obtained through homothety with the coefficient given by the ratio of time separation, as shown in figure 3.3.

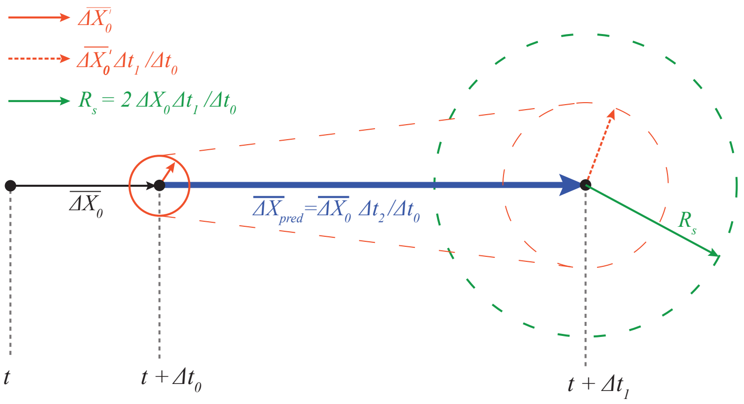

Figure 3.3: Homothety process whereby the displacement $\overline{\mathbf{\Delta X}}_0$ and the fluctuations $\overline{\mathbf{\Delta X}}'_0$ obtained analysing the short Δt acquisition are used to extrapolate the predicted particle displacement $\overline{\mathbf{\Delta X}}_{pred}$ and the radius of search R_S for a longer time separation between recordings.

Then, the NN criterion is applied between the predicted arrival position and the particles detected within the spherical search volume of radius R_S at the second exposure (see figure 3.2-right). After pairing, the binning procedure yields again data on a Cartesian grid. The logic of the entire algorithm is illustrated in figure 3.4 and comprises the following operations:

1. acquisition of multiple double-frame datasets with increasing time separation;
2. 3D particle detection by IPR at Δt_0;
3. particle pairing with NN principle;
4. ensemble-average of sparse velocity vectors within bins;
5. displacement predictor and search radius are built upon the Reynolds decomposition of the velocity inside the bin;
6. step 2 is repeated at Δt_1;
7. the predictor for displacement and fluctuations is applied at the position of the tracers;
8. step 3 is repeated based on the predicted position and the search radius;
9. step 4 yields data on a Cartesian grid, with time separation Δt_1.

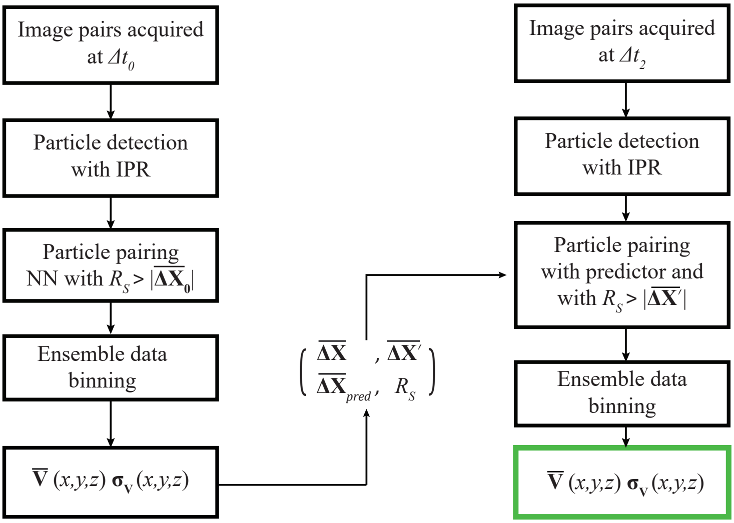

Figure 3.4: Schematic description of the operations composing the multi-step analysis (two steps currently considered).

3.3.1. CHAIN-VARIANT OF THE MULTI-STEP ALGORITHM

Inferring a displacement predictor and search radius from measurements at the shortest pulse separation time requires a robust and accurate estimate. The value of R_S may, however, be affected by high relative uncertainty. When amplified by the homothety the uncertainty may lead to overestimating the value of R_S, in turn increasing the false detection probability at time separation Δt_1. This effect is mitigated if one or multiple additional steps are included between Δt_0 and Δt_1, as shown in figure 3.5. As presented in the previous section, R_S is built from $\overline{\mathbf{\Delta X}'}$, more specifically from the standard deviation $\boldsymbol{\sigma}_\mathbf{V}$, that can be decomposed as (Sciacchitano, Wieneke, 2016):

$$\boldsymbol{\sigma}_\mathbf{V} = \sqrt{\boldsymbol{\sigma}^2_{\mathbf{V},turb} + \boldsymbol{\sigma}^2_{\mathbf{V},err}} \tag{3.14}$$

While the first term under the square root, representing the physical flow fluctuations ($\mathbf{\Delta X}'_{turb}$), scales linearly with Δt, the fluctuations associated to measurement noise ($\mathbf{\Delta X}'_{err}$) can be considered independent of the particle displacement.

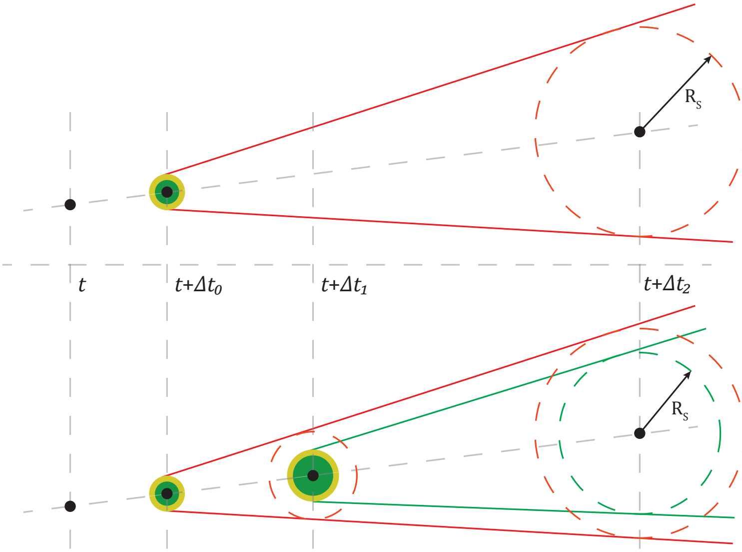

Figure 3.5: (top) Linear extrapolation of R_S from the fluctuations measured at time separation Δt_0. (bottom) Fluctuations overestimation is reduced using a chain-like multi-step algorithm. Red lines represent the value predicted by homothety in a single-step algorithm.

Given the above, any measurement with time separation larger than Δt_0 yields an estimation of the velocity fluctuations that is less affected by $\boldsymbol{\sigma}_{\mathbf{V},err}$. By this method, the choice of the search radius R_S for the final and largest time separation becomes significantly less affected by noise, reducing the search area and the probability of erroneous pairing.

3.4. APPLICATION TO TURBULENT WAKE FLOWS

Two experiments dealing with the wake of bluff objects have been conducted at the Aerodynamics Laboratory of the Aerospace Engineering Department of TU Delft. In the first experiment, a large aperture tomographic setup is used, whereas the second experiment makes use of a robotic volumetric PTV.

3.4.1. NEAR-WAKE OF TRUNCATED CYLINDER

The turbulent flow developing behind a truncated cylinder interacting with a flat plate turbulent boundary layer was described in the study of Schneiders et al. (2016). The experiments were performed in a low-speed wind tunnel with a cross section of $0.4 \times 0.4\text{m}^2$ at free-stream velocity of 5 m/s. A flat plate produces a turbulent boundary layer of approximately 25 mm thickness 1 meter downstream of its leading edge. A truncated cylinder of 100 mm diameter and height is placed in the symmetry plane of the plate. The Reynolds number based on the cylinder diameter is $Re_D = 3.5 \times 10^4$. The measurement volume was $30 \times 15 \times 20\text{cm}^3$ and is schematically represented in figure 3.6. The use of helium-filled soap bubbles as flow tracers was necessary to produce sufficient light scattering over such volume. The data consist of three sequences of 2,000 frames acquired at 2 kHz (Δt_0 = 0.5 ms) with four high-speed CMOS cameras (Photron FastCAM SA1, 1024 × 1024 pixels) subtending a solid angle of approximately 40 × 40 square degrees. The particle image recordings were evaluated with the algorithm Shake-The-Box (STB, Schanz et al., 2016). The velocity field obtained with STB is considered as reference to evaluate the performances of the multi-step analysis based on double-frame recordings.

The STB algorithm makes use of long tracks produced by a particle imaged at multiple time instants. In this case, a particle has been considered valid if it was tracked for at least six timesteps. Given the track length and the least-squares

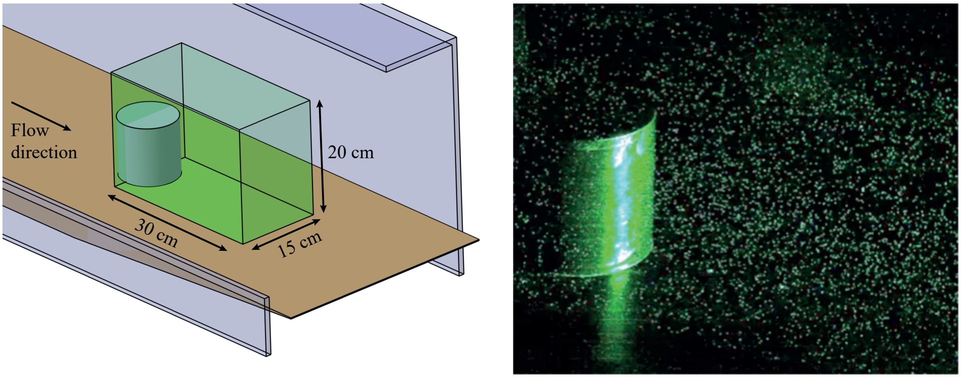

Figure 3.6: (left) Schematic setup in the test section, with measurement volume, shaded in green and channel cut-out for clarity. (right) Sample raw-image (adapted from Schneiders et al. 2016).

fit used to model the trajectory, a high measurement precision is achieved (estimated in the order of 10^{-3} m/s), as discussed in Schanz et al. (2016). To apply the proposed method, a double-frame dataset has been constructed from the original multi-frame recordings. Particles detected at the time step t by STB have been considered for the first frame, assigning to the second frame the particles found at the time step $t + \alpha \Delta t_0$, with α=[1,2,3]. The algorithm STB assigns a unique track ID number to each particle tracked across the domain. This number permits to evaluate if the particle pairing performed by the proposed method is correct. The results obtained by STB and with the dual-frame analysis are subject to the same binning process to yield the velocity distribution on a Cartesian grid, as described in section 3.3. Volumes $2 \times 2 \times 2$ cm^3 have been considered, with an overlap factor of 75%. The final vector pitch is then 0.5 mm.

The flow field around the cylinder exhibits large vortices and separated regions (figure 3.7, left), making it well suited to analyse the accuracy and robustness of the tracking algorithm under varying flow properties. The near-wake is characterized by regions of high fluctuations due to the interaction between the shear layers created at the sides, shown in figure 3.7 (right), and the two counter-rotating vortices that originate from the top of the object. Figure 3.8 reports the probability density function of the streamwise velocity in a small domain of the flow outer stream (indicated with region A in figure 3.7), where STB measurements yield a mean velocity of 5.72 m/s. The double-frame image analysis yields a sim-

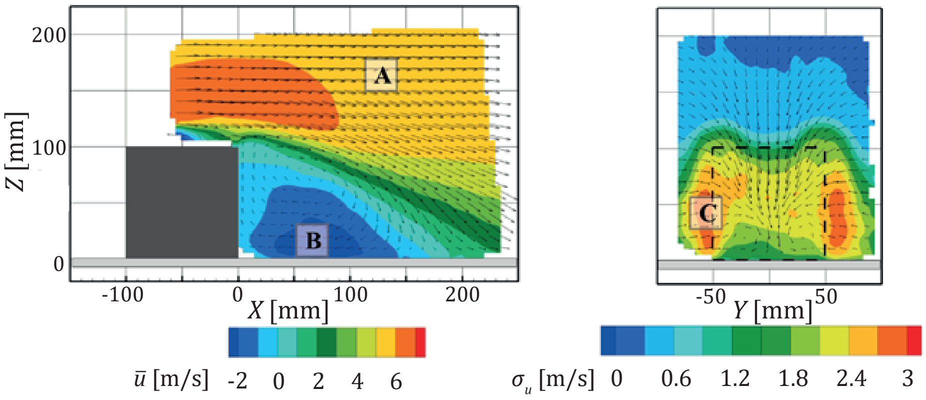

Figure 3.7: (left) Contour of the averaged streamwise component $\overline{u}$ of the velocity in the mean plane (Y = 0 mm). (right) The contour of the standard deviation of the stream-wise component of the velocity σ_u at the plane X = 100 mm.

ilar value when the multi-step algorithm is used. The single-step analysis at time separation Δt_0 exhibits a significant velocity bias (mean velocity of 5.5 m/s) and a dispersion one order of magnitude larger than the STB measurement (1.49 m/s and 0.16 m/s, respectively). The single-step analysis at larger time separation is directly compromised by a large number of spurious pairs (71.5%), leading to very large bias and random errors.

Two kinds of analysis are conducted based on the Reynolds averaged predictor. In both analyses, the velocity predictor is built from the time-average velocity and the velocity fluctuations are evaluated with the Δt_0 single-step analysis. In the first case, indicated with Δt_0 multi-step in Tab. 3.1, the time separation $\Delta t_1 = \Delta t_0$, whereas in the second analysis, indicated with $3 \cdot \Delta t_0$ multi-step, $\Delta t_1 = 3 \cdot \Delta t_0$.

Table 3.1: Comparison of double-frame analysis with STB in terms of mean velocity, standard deviation and percentage of correct pairs. Data relative to the outer stream (region A from figure 3.7 - left).

	STB	Δt_0 single-step	Δt_0 multi-step	$3 \cdot \Delta t_0$ single-step	$3 \cdot \Delta t_0$ multi-step
$\overline{u}$ [m/s]	5.72	5.50	5.72	2.06	5.72
σ_u [m/s]	0.16	1.49	0.18	3.78	0.15
% correct pair [-]	-	92	99	28	99

Both multi-step methods yield a major reduction of the number of spuri-

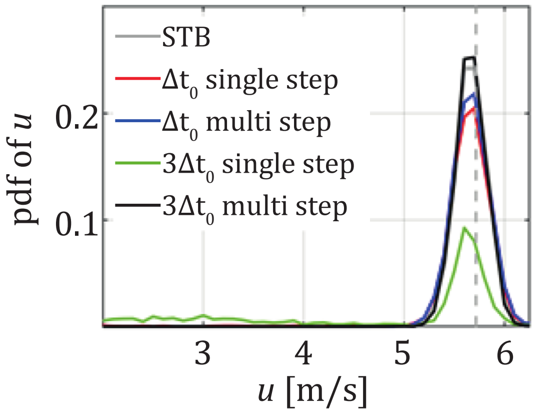

Figure 3.8: Relative probability of the streamwise component of the velocity in region A of figure 3.7. STB (grey) single-step with $\Delta t = \Delta t_0$ (red), multi-step with $\Delta t_1 = \Delta t_0$ (blue). Single-step with $\Delta t = 3 \cdot \Delta t_0$ (green) multi-step with $\Delta t_1 = 3 \cdot \Delta t_0$ (black). The dotted grey line shows the average velocity component obtained by STB.

ous pairs, leading to a probability of correct pairing of 99%. Furthermore, the mean velocity and the velocity fluctuations evaluated with these analyses agree well with the reference data. Nevertheless, the Δt_0 multi-step analysis exhibits slightly larger fluctuations than the reference and $3 \cdot \Delta t_0$ multi-step analysis due to the larger relative uncertainty of the measured displacement, thus confirming the enhanced precision achievable with a larger time separation. Figure 3.9 (left) illustrates the correct pairing probability η_p versus the relative displacement γ evaluated in the regions A, B and C shown in figure 3.7. The Monte-Carlo (MC) simulation of the free-stream flow is taken as the reference behaviour. Although reproducing a similar trend, the correct pairing probability η_p obtained with MC simulation slightly overpredicts the results obtained by the single-step approach in the free-stream domain. The most evident behaviour observed by this analysis is that the regions with an increased level of turbulent fluctuations exhibit a more rapid drop in correct pairing probability when the single-step time separation is increased.

The introduction of the displacement predictor based on the Reynolds average increases the percentage of correct pairing in all the considered regions of the flow: in the free-stream (region A) Δt can be extended up to 8 times with the

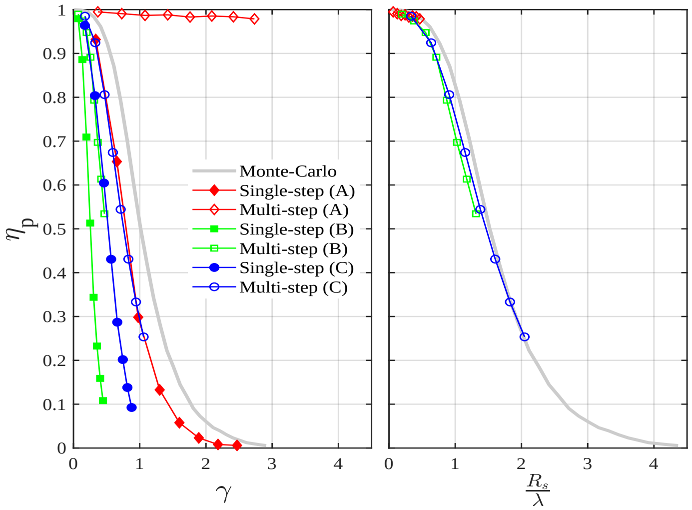

Figure 3.9: (left) Correct pairing probability η_p versus the ratio γ between the particle displacement and the mean particle distance. Results were obtained with single-step analysis and comparison to the Monte Carlo simulation of free-stream conditions. (right) η_p variation with the ratio between search radius and mean particle distance (legend same as for left figure). Data obtained by multi-step analysis with $\Delta t_1 = 3 \cdot \Delta t_0$.

probability of correct pairing remaining above 98%. In the turbulent regions, such as the recirculation region in the wake (region B), and the lateral shear layer (region C), the use of the predictor yields benefits up to $\Delta t_1 = 3 \cdot \Delta t_0$. The latter behaviour is consistent with equation 3.11, given the higher level of velocity fluctuations in the object wake. figure 3.9 (right) shows the probability of correct pairing ratio η_p with respect to the ratio R_S/λ for the multi-step analyses. The curves collapse approximately onto the same behaviour, indicating a universal relation between R_S/λ and the probability of successful pairing. Considering $\eta_p = 0.95$ as the acceptance criterion, the corresponding search radius becomes approximately $R_S = 0.5\lambda$. The latter may be proposed as a design criterion to choose the upper limit of Δt_1 for a given experiment comprising recordings at different values of the time separation. Given the spatial variability of the flow properties, a single optimum value for Δt_1 cannot be identified.

figure 3.10 shows the spatial distribution of η_p at the plane Y = 0 mm, while increasing Δt. The single-step analysis rapidly degrades in regions of large displacement. For instance, when $\Delta t = 3 \cdot \Delta t_0$, only the low-velocity region in the

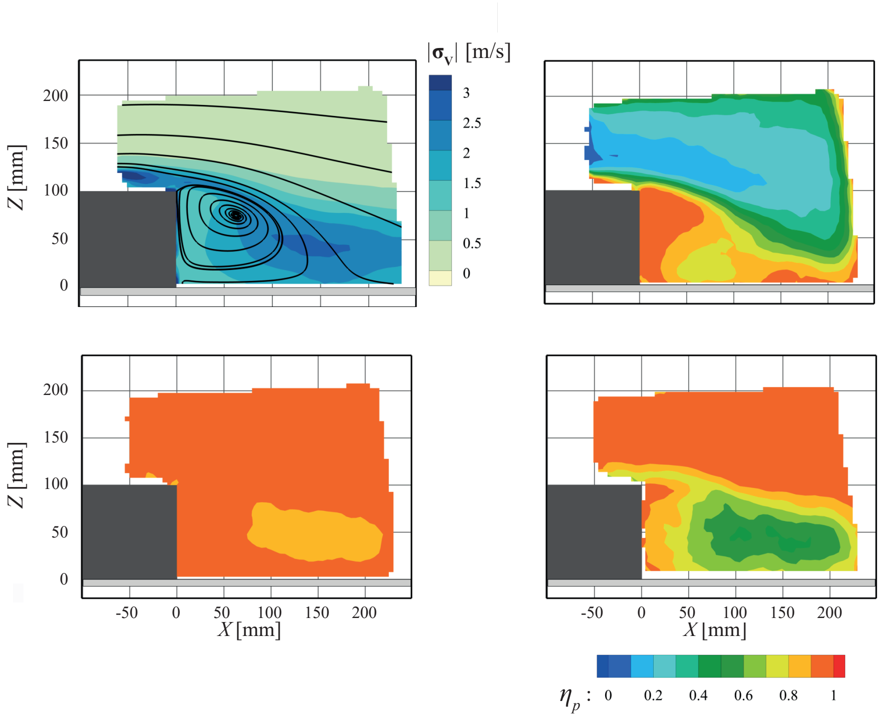

Figure 3.10: (top-left) Contour of the magnitude of the fluctuations $|\boldsymbol{\sigma}_\mathbf{V}|$ given by STB at Y = 0 mm with overlaid surface streamlines. Contour of correct pairing ratio η_p at Y = 0 mm given by the proposed methodology for: (top-right) single-step with $\Delta t = 3 \cdot \Delta t_0$ (bottom-left) multi-step with $\Delta t_1 = 3 \cdot \Delta t_0$ (bottom-right) multi-step with $\Delta t_1 = 6 \cdot \Delta t_0$.

near wake exhibits a high percentage of correct pairing (top-right). The use of the predictor for the case $\Delta t_1 = 3 \cdot \Delta t_0$ (bottom-left) leads to $\eta_p > 0.9$ in most of the flow field, except for the wake with high fluctuations (see figure 3.10 top-right), where $\eta_p > 0.7$. Further extension of the pulse separation time (figure 3.10 bottom-right) results in frequent false pairing, mostly in the wake, which is due to the condition given by equation 3.2 not being respected. The results shown until now are obtained by applying the pairing strategy on particles previously detected by the Shake-the-Box algorithm, which is also considered unaffected by the phenomenon of ghost particles (Schanz et al., 2016). Therefore, by knowledge of the particle tracks, it has been possible to distinguish correct and incorrect particle pairings for the double-frame analysis. A more realistic situation has been simulated using the Iterative Particle Reconstruction algorithm proposed by Wieneke (2013), thus following the steps illustrated in the flow chart of figure 3.4.

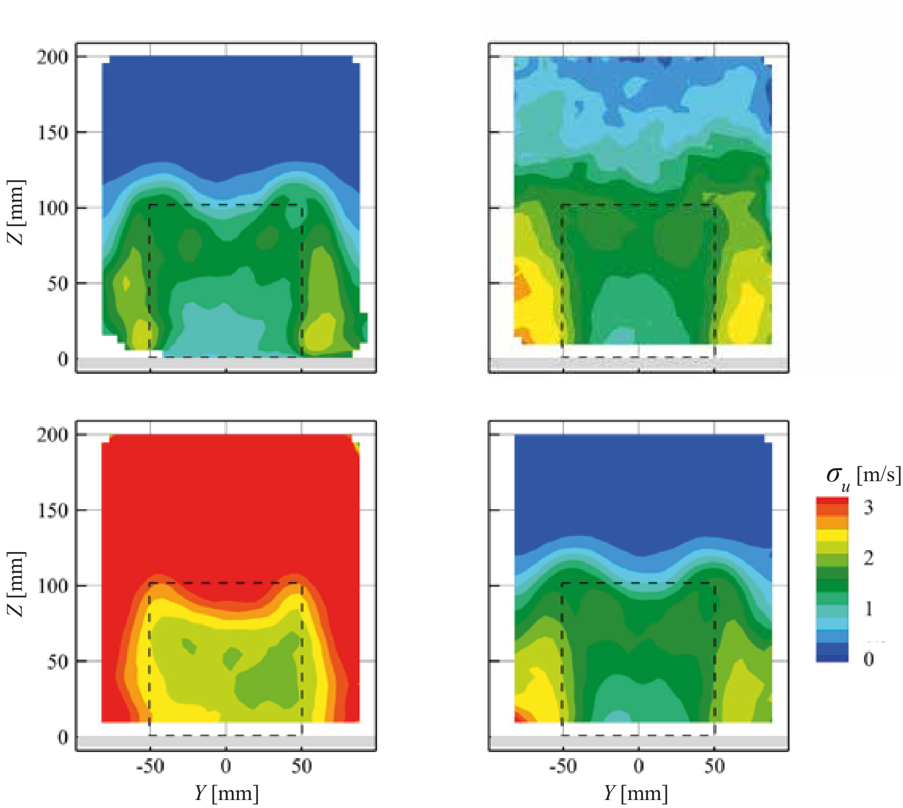

Figure 3.11: Contours of the standard deviation of the streamwise velocity fluctuations at X = 100 mm. (top-left) STB (top-right) single-step with $\Delta t = \Delta t_0$ (bottom-left) single-step with $\Delta t = 3 \cdot \Delta t_0$ (bottom-right) multi-step with $\Delta t_1 = 3 \cdot \Delta t_0$.

The standard deviation of the streamwise velocity component at X = 100 mm, illustrated in figure 3.11 (bottom-left), shows that the single-step algorithms yield spurious fluctuations due to a significant percentage of incorrect pairings. The level of fluctuations is clearly unacceptable for $\Delta t = 3 \cdot \Delta t_0$, where the velocity standard deviation in the outer region exceeds 50% of the free-stream value. Conversely, the adoption of the multi-step Δt methodology suppresses the spurious velocity fluctuations due to incorrect pairing, yielding measured fluctuations of the same order as the reference ones obtained by STB. It must be noticed that in the regions of highest flow fluctuations, namely the two free-shear layers at the sides of the models $Y = \pm 60$ mm, the difference between the multi-step analysis and the reference data is the largest. As indicated by equation 3.11, the increase of the local turbulence intensity reduces the maximum achievable extension of Δt. The effects of the chain-variant method have been assessed considering the same final pulse separation time $\Delta t = 3 \cdot \Delta t_0$. The chain algorithm permits to decrease R_S in most of the flow field, with the maximum decrease that occurs in the free-stream, where $R_S = 1.7$ mm for the dual-step algorithm and $R_S = 0.8$ mm for its the chain-variant. For what concerns the standard deviation of the velocity, due to the limited time increase, no substantial differences are noticed.

3.4.2. COAXIAL VELOCIMETRY IN THE NEAR-WAKE OF AHMED BODY

Experiments are performed in the Open Jet Facility (OJF) of TU Delft Aerospace Engineering Laboratories. The near-wake of the Ahmed body (Ahmed et al., 1984) at a free-stream velocity of 12 m/s and a turbulence intensity of 0.5% (Lignarolo et al., 2015) is investigated by robotic volumetric PTV (Jux et al., 2018). The Reynolds number based on the height H of the model is $\mathrm{Re}_H = 115,000$ and the selected slant angle is 25°.

Table 3.2: Measurement parameters for Ahmed body experiment.

Seeding	HFSB, ~ 300 μm diameter
Illumination	Quantronix Darwin-Duo Nd:YLF laser (2 x 25 mJ @ 1 kHz)
Recording Device	LaVision MiniShaker S system: 4 x CMOS cameras 800 × 600 @ 511 Hz 4.6 μm pitch
Imaging	f = 4 mm, $f_\# = 8$
Acquisition frequency	Time-resolved $f_{TR} = 700$ Hz; Double-frame $f_{DF} = 300$ Hz
Pulse separation time	Time-resolved: $\Delta t = 1/f_{TR} = 1.43$ ms Double-frame: $\Delta t = [61, 122, 244, 488, 610]$ μs
Magnification factor	~ 0.01 at 40 cm distance
Number of images	8000

The considered volume is 200 × 200 × 450 mm^3, obtained from a single view of the CVV system (figure 3.12). Both time-resolved and double-frame acquisitions have been performed. For the former, the acquisition frequency is $f = 700$ Hz. In double-frame mode, sets of image pairs are acquired at a rate of 340

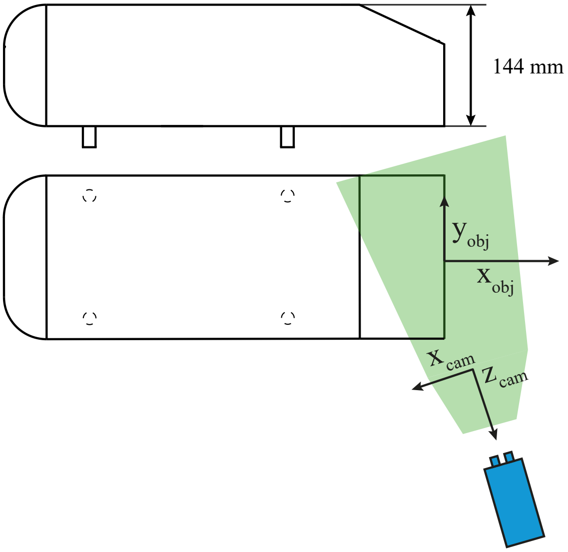

Figure 3.12: Side and top view of the Ahmed body with the measurement domain (green shade). Object and camera coordinate systems are shown.

Hz. The time-resolved dataset is analysed with the STB algorithm from LaVision DaVis 8.1 software. Multiple datasets with $\Delta t_0 = 61\mu$s and larger separation $\Delta t = [2,4,6,8,10] \cdot \Delta t_0$ were acquired. The minimum pulse separation time is selected for a conservative value of $\gamma = 0.07$, guaranteeing a high probability of correct pairing at Δt_0. For the binning process, $2 \times 2 \times 2$ cm^3 volumes have been considered, with an overlap factor of 75%. The final vector pitch is then 0.5 mm. Two different coordinate systems are here considered: the camera and the object one. While the camera coordinate system follows the movement of the robot, the object coordinate system is stationary and has the X axis aligned with the incoming free stream velocity vector, as shown in figure 3.12. The wake of the Ahmed body features the so-called C-pillar vortices: a set of counter-rotating large-scale streamwise vortices emanating from the upstream edge of the slant. As they develop downstream, the C-pillar vortices interact with the recirculation region at the back of the object, creating a complex 3D flow field. The organization of the velocity field is illustrated at $X_{obj} = 0.5H$ in figure 3.13. The presence of the two vortical structures is confirmed by the vectors in the velocity slice and by the

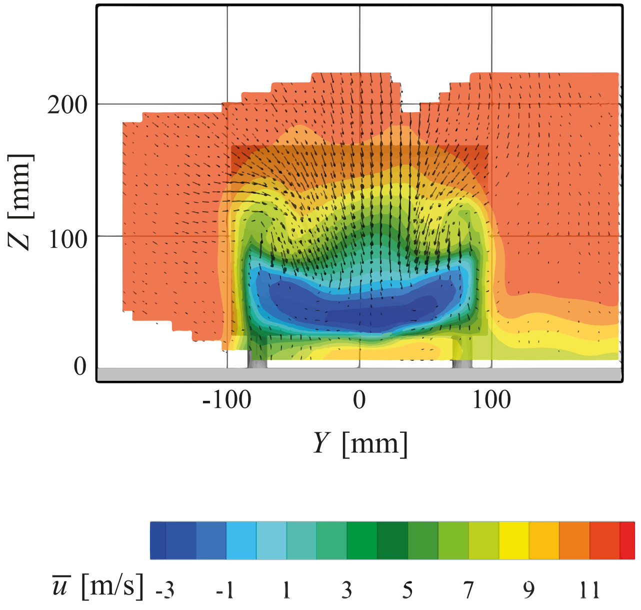

Figure 3.13: In-plane velocity vectors and colour contours of cross-plane velocity at X_{obj} = 0.5 H. Results obtained from STB and time averaged over bins of 20 mm side length.

iso-surface of mean streamwise vorticity $\overline{\omega}_x = \pm 250$ Hz shown in figure 3.16 (top-left). The robotic system is characterized by the ability to measure multiple portions of the flow that can be stitched together to obtain the final global average velocity field. For this reason, two relevant coordinate systems are mentioned: the global (object) and the intrinsic (CVV) one, shown schematically in figure 3.12. The following analysis is performed using the CVV coordinate system in order to analyse the properties of the in-plane and the coaxial velocity components separately. A theoretical estimate of the DVR is given, based on the characteristics of the coaxial velocimeter. Considering a $c_\tau = 0.2$, the resulting error on particle position is $\varepsilon = 0.13$ mm along x- and y- directions, which becomes $\varepsilon = 2.2$ mm in the depth (viz. coaxial) direction (Schneiders et al. 2018). The above translates in terms of velocity uncertainty relative to free-stream value with $\varepsilon_u = \varepsilon_v = 0.26$ for a single-step double-frame measurement with $\Delta t = \Delta t_0 = 61\mu$s. For a time-resolved measurement with particle tracks comprising 5 samples of the particle position, the uncertainty reduces to $\varepsilon_u = 0.0025$ (0.25%). From the above, a DVR of 4 and 400 can be inferred for the double-frame single-step and STB analysis (with 5 recordings separated by 1.43 ms each) respectively. This large difference is the result of two factors: the STB analysis encompasses a significantly longer time separation (approximately 23 times larger than Δt_0 for double-frame); second, the velocity measurement is the result of a least-squares polynomial fit that reduces random errors. The multi-step analysis based on Reynolds average predictor allows an increase in the time separation, therefore increase of DVR, but only from the former of the two factors. In the present case the recordings with the longest pulse separation time, $\Delta t = 10 \cdot \Delta t_0$, potentially lead to a DVR = 40. However, along the coaxial direction, the DVR remains fairly limited (DVR ~ 3-5), considering the small angular aperture of the coaxial velocimeter.

Table 3.3: Comparison of STB with double-frame analysis, in terms of mean velocity, standard deviation along X_{cam} and Z_{cam} directions. Data relative to a $2 \times 2 \times 2$ cm^3 region in the outer stream.

	$\overline{u}$	$\lvert\Delta u\rvert$ [m/s]	$\lvert\Delta u\rvert$ [%]	σ_u [m/s]	$\lvert\Delta\sigma_u\rvert$ [%]
STB	-11.34	-	-	0.29	-
Δt_0 single-step	-11.15	0.20	1.8	1.16	300
Δt_0 multi-step	-11.22	0.12	1.1	0.63	110
$2\Delta t_0$ multi-step	-11.17	0.17	1.5	0.62	110
$6\Delta t_0$ multi-step	-11.32	0.02	0.01	0.54	80
$10\Delta t_0$ multi-step	-11.18	0.16	1.5	0.34	14
	$\overline{w}$ [m/s]	$\lvert\Delta w\rvert$ [m/s]	$\lvert\Delta w\rvert$ [%]	σ_w [m/s]	$\lvert\sigma_w\rvert$ [%]
STB	2.71	-	-	0.51	-
Δt_0 single-step	1.11	1.60	60	7.77	1400
Δt_0 multi-step	1.18	1.53	56	2.04	300
$2\Delta t_0$ multi-step	1.04	1.67	62	2.24	340
$6\Delta t_0$ multi-step	1.73	0.99	36	1.57	200
$10\Delta t_0$ multi-step	1.96	0.75	28	1.45	185

The probability density of x- and coaxial-component in the outer flow region are shown in figure 3.14. Synthesis of the results in terms of mean and standard deviation are presented in Table 3.3 for the different methods. The reference is assumed to be the time-resolved analysis from STB, which also exhibits the lowest dispersion of the velocity data.

The single-step analysis of double-frame recordings at time separation $\Delta t_0 =$

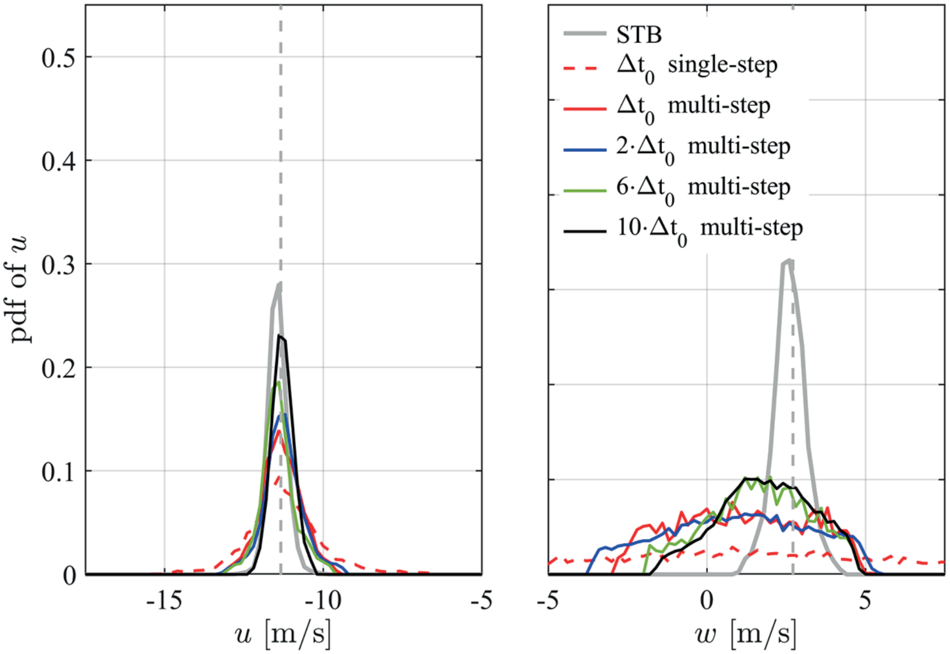

Figure 3.14: Relative probability of (left) the u component in the intrinsic reference frame and (right) the w component in the intrinsic reference frame in a small free-stream region in the near field from the cameras. Comparison between the results obtained by STB and different methodologies herein presented. The mean value obtained by the reference is underlined by the grey dotted line.

61μs, exhibits the widest dispersion of the data, with σ_u being approximately four times larger than that given by STB. The multi-step analysis progressively reduces the data dispersion by increasing Δt_1. A standard deviation 14% higher than the reference is obtained when $\Delta t_1 = 10 \cdot \Delta t_0$. Along the coaxial direction, a much wider data dispersion is observed and the single-step analysis with $\Delta t = \Delta t_0$ returns almost a flat distribution. Increasing the time separation by the multi-step analysis, although the overall uncertainty remains large: at $\Delta t_1 = 10 \cdot \Delta t_0$, the coaxial velocity component is underestimated by approximately 30%. The analysis until now has been carried out in the outer region, where the maximum displacement is expected. The high particle displacement corresponds to high values of γ, leading to an increase in false pairing appearance.

The amplitude of velocity fluctuations plays a crucial role in determining the

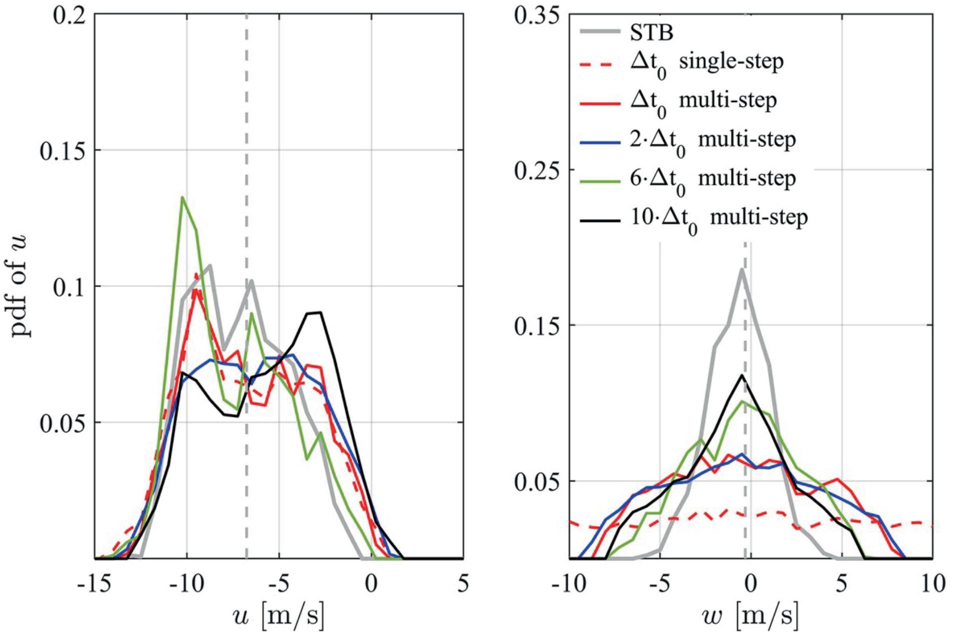

Figure 3.15: Relative probability of (left) the u and (right) w components (in the CVV reference frame) in the C-pillar region. Comparison between STB and multi-step analysis. The mean value obtained with STB is the vertical dashed grey line.

success rate of correct pairing, even when a predictor velocity is available. For this reason, a region of strong spatial and temporal and fluctuations has been considered in the shear region of the C-pillar vortices. The probability distribution of u and w is analysed and shown in figure 3.15. The smaller displacement and the relatively low particle concentration yield $\gamma = 0.04$ for $\Delta t = \Delta t_0$. In this region, given the wider dispersion of the value due to the physical fluctuations exhibited by the flow, the in-plane and coaxial components show similar behaviour and the results are more closely comparable to those obtained with STB. A tenfold increase of the pulse separation time returns a velocity distribution not affected by false pairing ($R_S/\lambda = 0.4$ for $\Delta t_1 = 10 \cdot \Delta t_0$). A final analysis is made to inquire into the measurements of the three-dimensional vorticity field, often inspected to understand the topology of vortices emanating from complex bluff bodies. Figure 3.16 shows the three-dimensional distribution of the time-average streamwise vorticity $\overline{\omega}_x$ by two iso-surfaces selected at ±250 Hz. The comparison is made between STB, single-step ($\Delta_t = \Delta t_0$) and two multi-step analyses: $\Delta t_1 = \Delta t_0$ and $\Delta t_1 = 10 \cdot \Delta t_0$ respectively. The C-pillars vortices visualisation using the single-step analysis suffers from random fluctuations appearing in the entire measurement domain. These fluctuations are mostly associated with the large uncertainty on the coaxial component (and its spatial derivative) that takes part in the formulation of the streamwise vorticity. The multi-step analysis at shortest time separation exhibits some noise reduction, ascribed to the reduction of incorrect pairings when a displacement predictor and a smaller search radius are used. When the pulse separation is extended, with $\Delta t_1 = 10 \cdot \Delta t_0$, noisy fluctuations are considerably attenuated and a more regular vorticity iso-surface is obtained, in better agreement with the STB analysis.

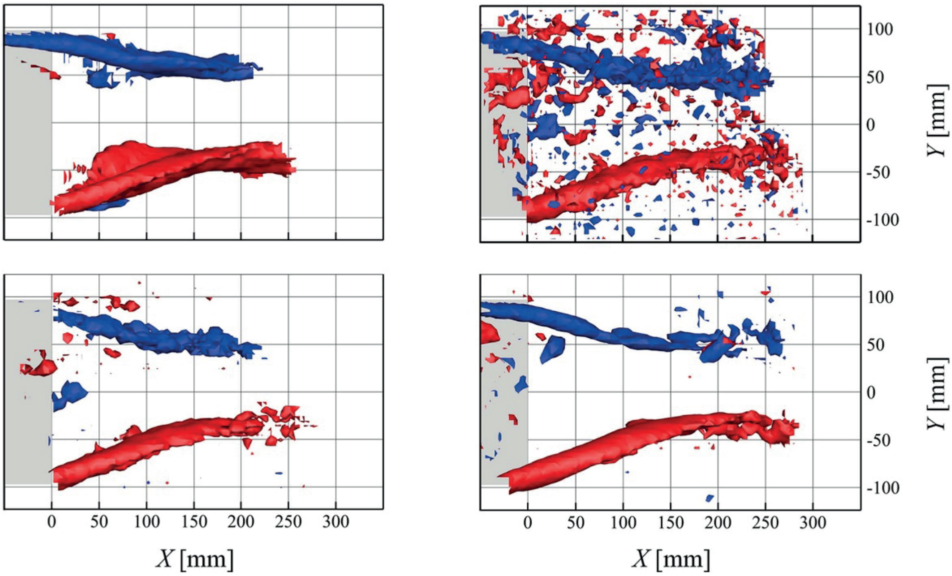

Figure 3.16: Iso-surface of $\overline{\omega} = \pm 250$ Hz (blue: positive, red: negative) in the object reference frame. Top-left: STB; top-right: single-step at Δt_0; bottom-left: multi-step with $\Delta t_1 = \Delta t_0$; bottom-right: multi-step with $\Delta t_1 = 10\Delta t_0$.

3.5. CONCLUSIONS

A novel method for the analysis of 3D PTV experiments based on double-frame recordings has been proposed, which is based on Reynolds decomposition. The method yields the time-average velocity field from the analysis of the instantaneous particle velocity, (compared to other multi-frame methods proposed in literature, like from Hassan, Canaan, 1991; and Schanz et al., 2016). In the multi-δt method two or more sets of recordings are necessary to produce, firstly, a robust displacement predictor, based on a short-time separation, and, secondly, to extend the displacement with a data set obtained at a larger time separation. A theoretical analysis shows that the DVR of the multi-step method can be significantly higher than single step analysis in flows with low to moderate turbulence. A chain-like variant of the multi-step method has the additional benefit of reducing the bias that overestimates the amplitude of turbulent fluctuations. Two experimental databases are used to assess the multi-Δt method and compare it to the time-resolved analysis made with the STB algorithm. The multi-step analysis clearly extends the DVR of the single-step analysis. The fundamental limit to extending the time separation for the multi-step method lies in the condition where the displacement dispersion caused by the turbulent velocity fluctuations becomes comparable to the inter-particle distance. A-posteriori analysis suggests $R_S < 0.5\lambda$ as the experiment design criterion for the optimal extension of the time separation, which corresponds to the condition $\mathit{\Delta} t_{1max} = 0.25\lambda/|\sigma_V|$.

4

ADAPTIVE MULTI-EXPOSURE TIMING FOR PTV

4.1. BACKGROUND

In the previous chapter, a new methodology to increase the DVR of double-frame PTV measurements has been presented. Due to the nature of its multiple datasets with increasing pulse separation time, it shares the limitations characteristic of double-frame measurements. Firstly, the particle velocity is determined using only two positions, it is not possible to perform a polynomial fit, reducing the achievable precision of the velocity determination. Furthermore, due to the linear nature of the velocity determination, the truncation error starts increasing with longer pulse separation times (Boillot, Prasad, 1996). Finally, the flow acceleration cannot be determined, making impossible the calculation of the pressure field (Oudheusden, 2013). Another possible approach to cope with high-speed flows relies on the use of multi-exposure recordings, which allow increased measurement accuracy due to tracking particles at multiple time instants, as well as the determination of the particle's accelerations and in turn the pressure field. The proposal of a new multi-exposure, multi-step strategy is the topic of this chapter.

Two versions of the STB algorithm adopting this strategy have been developed by Novara et al. (2016) and Sellappan et al. (2020), respectively. The difference between the two presented methodologies lies in the adopted timing strategy to obtain the four particle positions across the two frames, as discussed in the next section. The application of these methodologies has been presented copying with velocities ranging from 35.5 m/s to 290 m/s by Novara et al. (2019) and Godbersen, Schröder (2020), respectively. However, both the mentioned methodologies make use of fixed time separations among the pulses, thus leading to increased measurement accuracy only locally and not in the entire flow field. Additionally, they suffer from the presence of overlapping particle images in regions of low flow velocities, leading to erroneous particle reconstructions and velocity measurements. Furthermore, no theoretical analysis of the achievable DVR has been presented in the literature, leaving the question of the optimal selection of the time separation among pulses unanswered. The current chapter aims at solving the limitations of current multi-pulse PTV approaches by proposing a multi-step multi-exposure algorithm with adaptive time separation. The approach, based on a learning paradigm similar to the one applied in chapter 3, guarantees that the measurement accuracy is maximised in the entire flow domain and that no overlapping particle images are present even in regions of low flow velocities. Additionally, a theoretical framework is developed for the evaluation of the maximum DVR achievable with the different PTV strategies. In order to prove the effectiveness of the proposed methodology, an experimental dataset concerning the flow around a truncated cylinder at Re= 3.3×10^5 is considered. The state-of-the-art methodology Shake-The-Box is used to produce the ground truth that is taken as a reference.

4.2. DVR OF TIME-RESOLVED PTV APPROACHES

The use of multiple positions of the same particle has been proven effective in increasing the precision of the velocity determination (Cierpka et al., 2013; Lynch, Scarano, 2013; Schanz et al., 2016; amongst others). This can be achieved by acquiring time-resolved data or multi-exposed images. In order to define the achievable DVR in this situation, let us consider a case where the same particle is imaged k times, each with a time separation of Δt, by using one of the two mentioned approaches. The obtained discrete particle positions can be used to build a track, which can be regularized through a polynomial regression, as shown in figure 4.1. The advantages of using multiple discrete particle positions to evalu-

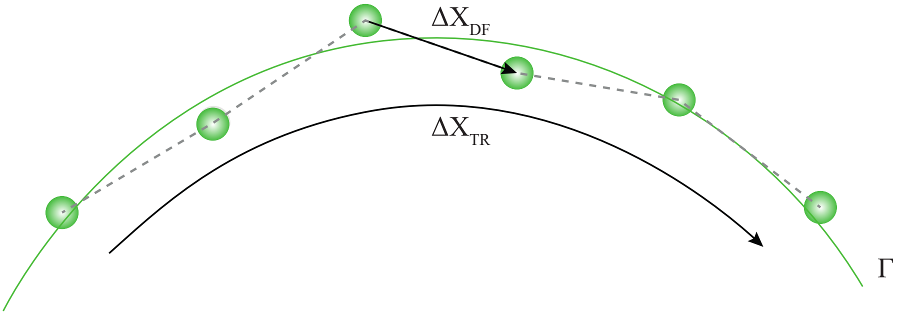

Figure 4.1: Schematic representation of particle track evaluated at a discrete number of positions. While the grey line represents the displacement evaluated with a double-frame single exposure analysis, the green line shows the streamline obtained through a second-order polynomial regression.

ate the particle velocity arise from two main factors: the total evaluated displacement increases and the effect of random errors on the particle position determination is reduced. For k successive particle image recordings, the displacement increases by a factor k with respect to the dual-pulse analysis, whereas the positional uncertainty decreases by $c_\alpha/\sqrt{k}$ (Lynch, Scarano, 2013), with c_α being a coefficient dependent upon the track regularization technique used. Combining these two effects, the achievable DVR for k recordings of the particles' positions is:

$$\mathrm{DVR}_{\mathrm{ME}} = \frac{k\sqrt{k}|\Delta\mathbf{X}_{\mathrm{max}}|}{c_\alpha \varepsilon_x} \tag{4.1}$$

where the ME subscript stands for multi-exposure. Comparing equation 3.5 and equation 4.1, it is possible to evaluate the DVR gain G_{DVR} when multiple exposures of the same particle are considered:

$$G_{\mathrm{DVR}} = \frac{\mathrm{DVR}_{\mathrm{ME}}}{\mathrm{DVR}_{\mathrm{DF}}} = \frac{k\sqrt{k}}{\sqrt{2}c_\alpha} \tag{4.2}$$

From equation 4.2, it can be concluded that the achievable increase of DVR scales as $k^{(3/2)}$, in line with what already theorized for analysis based on cross-correlation (Lynch, Scarano, 2013). The DVR expressions defined in equation 1.1 and equation 4.1 take into consideration the maximum particle displacement and are truly representative of the entire measurement only for a homogeneous flow field (e.g. grid turbulence). In many cases of interest, the velocity and the acceleration vary largely across the field, with the effect that regions at lower velocities are affected by larger relative errors. In this context we define a local principle for the dynamic velocity range:

$$\mathrm{DVR}(x) = \frac{|\Delta\mathbf{X}_{\mathrm{max}}(x)|}{\sigma_{\Delta X}} \tag{4.3}$$

which represents the inverse of the local relative uncertainty of the velocity (viz. displacement). In order to evaluate the measurement accuracy in the entire domain, the local DVR values defined by equation 4.3 shall be averaged over the entire measurement volume:

$$\overline{\mathrm{DVR}} = \frac{1}{\mathcal{V}} \int_{\mathcal{V}} \mathrm{DVR}(x) \, d\mathcal{V} \tag{4.4}$$

where $\mathcal{V}$ represents the total measurement volume and $d\mathcal{V}$ is the sub-volumes in which the DVR is calculated. A common approach to obtaining particle tracks composed of multiple particle positions is the adoption of a time-resolved (TR) image acquisition strategy. The development in terms of illumination and acquisition hardware has permitted the introduction of tracking algorithms capable of following each particle for several time instants. The maximum resolvable velocities are dependent on multiple factors, such as particle density and maximum frequencies of the illuminators and the cameras. To enable flow measurements at relatively high velocity ($U_\infty > 50$ m/s), aside from the double-pulse single-exposure measurements that are always possible, strategies that imply the use of multi-exposed pair of images have been presented and are discussed in the next section.

4.3. APPROACHES FOR MULTI-EXPOSURE PTV

Two different multi-exposure PTV strategies have been presented in the literature by Novara et al. (2016) and Sellappan et al. (2020), respectively. Both are based on a two-frame acquisition strategy, with two dual-cavity lasers used to produce four pulses (I-IV), and two exposures in each of the frames. The main difference between the two presented methods lies in the chosen timing strategy, as graphically described in figure 4.2. While Novara et al. (2016) applied a short-long-short timing strategy, with the inter-frame pulse separation time Δt_0 larger than the intra-frame pulse separation time Δt_1, Sellappan et al. (2020) proposed a long-short-long pulse separation time strategy, with $\Delta t_0 < \Delta t_1$. In both cases, the particle position is determined by using the Iterative Particle Reconstruction method (Wieneke, 2013), as implemented in the Davis software from LaVision. For both approaches, the particle pairing is divided into two different steps: the definition of a two-pulse track and then the combination of two two-pulse tracks in a four-pulse track. In the method presented by Novara et al. (2016), two-pulse tracks are created for each of the frames (pairs I-II and III-IV) and linear extrapolation is used to determine the potential middle point of the sequence. Due to the direction ambiguity created by the analysis of two exposure on the same frame, for each two-pulse track, two possible middle points have to be evaluated. When two pairs are matched across the frames, as shown

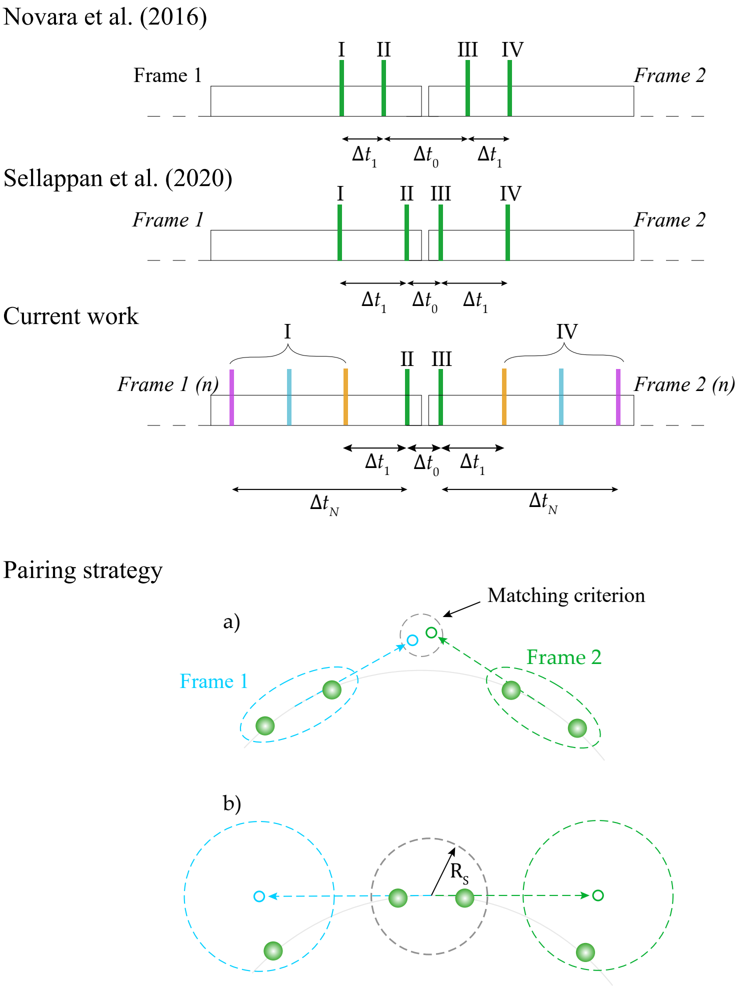

Figure 4.2: (Top) Timing strategies of multi-exposure acquisitions presented by Novara et al. (2016), Sellappan et al. (2020) and the current chapter. Δt_0 represents the inter-frame time separation, while $[\Delta t_1 \dots \Delta t_N]$ represent the intra-frame pulse separation times. (Bottom) Schematic representation of the different pairing strategies presented by: (a) Novara et al. (2016) and (b) Sellappan et al. (2020).

in figure 4.2, the position of the particles is fitted using a second-order polynomial regression and the velocity is evaluated at the middle point of the particle track. Sellappan et al. (2020) modified the algorithm by adopting the mentioned long-short-long pulse separation time strategy. In this case, as the first step, a two-pulse track is created across frames, pairing particles at locations II and III.

The fact that the two-particle positions are on subsequent frames eliminates the directional ambiguity present in the method from Novara et al. (2016). Furthermore, the increase in the time separation between the two pulses recorded on the same frame leads to an increase in the accuracy of the determination of the velocity and the acceleration along the track (Novara et al., 2019). The two-pulse pair is then extrapolated forward and backwards in time, where the particle positions at instants I and IV are then researched in spherical volume. Once all four particle positions are determined, a second-order polynomial regression is used to determine the middle point particle position and the corresponding velocity and acceleration.

The choice of Δt_0 and Δt_1 is crucial for both methodologies since a compromise between accuracy and robustness has to be made. Due to the choice of a single pair of pulse separation times $[\Delta t_0, \Delta t_1]$ for the entire measurement volume, the common strategy is to select the maximum allowed displacement from which, given the expected maximum velocity, a suitable T can be calculated, where $T = \Delta t_0 + 2\Delta t_1$. As previously discussed, this choice creates an inhomogeneity of the measurement accuracy, because low-velocity regions will feature smaller particle image displacements and therefore higher relative uncertainties. Additionally, in these regions, the possibility of particle image overlap arises. Overlapping particle images are a well-known problem since the advent of PIV and several solutions have been presented in the literature (Adrian, 1986; among others). Considering the acquisition strategy proposed by Sellappan et al. (2020), figure 4.3 shows three possible scenarios with decreasing flow velocity. The appearance of one of these scenarios depends on the ratio between the particle displacement $\Delta t|\mathbf{u}|$ and the particle image diameter d_τ. Scenario (a) describes the desired situation to obtain both an accurate particle position and velocity determination and is achieved when $\Delta t_0|\mathbf{u}| \gg d_\tau$, with $\Delta t_1 > \Delta t_0$. The pulse separation times Δt_0 and Δt_1, however, cannot be extended indefinitely, due to the appearance of false pairing (Saredi et al., 2020) and truncation errors (Boillot, Prasad, 1996). Considering scenario (b), even if the particle images corresponding to pulses II and III overlap, this does not prevent the particle pairing since they are located on different frames. However, the small displacement between the particle positions II and III causes a low accuracy of the velocity vector

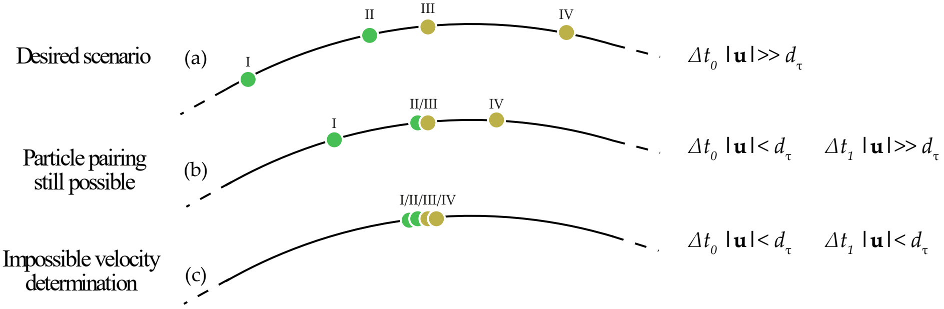

Figure 4.3: Example of three possible scenarios obtained by a double-frame double-exposure acquisition strategy at different flow velocities.

used to predict the particle positions at I and IV, increasing the probability of false pairings. Scenario (c) describes instead the situation when all four particle images overlap. In this case, particle position determination within each frame is not possible anymore. For this reason, it becomes clear that it is desirable to obtain scenario (a) in the entire measured volume. This is not achievable with a single combination of Δt_0 and Δt_1.

4.4. ADAPTIVE MULTI-STEP MULTI-EXPOSURE PTV

Recalling the definition of equation 4.3 we propose a method that homogenizes the relative error by producing a rather constant local particle displacement $|\Delta\mathbf{X}|$. This principle directly mimics the concept anticipated by Hain, Kähler (2007) but in the context of Lagrangian particle tracking with multi-exposed images. The main ingredients of this technique are the availability of a predictor, in terms of time-average velocity $\overline{\mathbf{V}}_{\text{pred}}$ and fluctuations root-mean-square $\mathbf{V}'_{\text{pred}}$, and a strategy to vary the pulse separation time pairs $[\Delta t_0, \Delta t_1]$ across the measurement campaign. To obtain the former, a multi-step approach is considered, similar to the one presented in the previous chapter. First, a double-frame single-exposure acquisition is performed and processed to produce a first estimation of the velocity field. The Lagrangian information obtained from the analysis of the double-frame single-exposure images is mapped onto a uniform Eulerian grid following the ensemble averaging procedure presented by Agüera et al. (2016), thus yielding the velocity predictor $\overline{\mathbf{V}}_{\text{pred}}$. The analysis of the velocity predictor in the measurement volume allows the determination of the time interval boundaries (T_{min}, T_{max}) for the successive multi-exposure image acquisition, based on the ratio between the desired displacement $|\Delta\mathbf{X}|_0$ and the local flow velocity. The procedure implemented to determine the suitable pulse separations is as follows. The distribution of the absolute velocity obtained by the analysis of the predictor velocity field is divided into N intervals, ranging between 0 and $\overline{\mathbf{V}}_{\mathrm{max}}$ with a decreasing reference velocity V_n is assigned to the nth interval. The definition of the desired displacement allows evaluating the required total time T for each interval through the equation:

$$T_n = \frac{|\Delta\mathbf{X}|_0}{V_n} = \Delta t_0 + 2\Delta t_1 \tag{4.5}$$

Once the total time for each interval is set, N acquisitions are performed with the pair $[\Delta t_0, \Delta t_1]_n$ varying accordingly to respect the indications given by equation 4.5. To select which tracks have to be considered for each measurement, a spatial map is created starting from the Eulerian grid on which $\overline{\mathbf{V}}_{\mathrm{pred}}$ was mapped. A value of T_n is assigned to each sub-volume of the Eulerian grid and only the tracks that come from the corresponding acquisition are then considered. Finally, the same binning procedure (Agüera et al., 2016) is applied to obtain the final time-average velocity field. In summary, the proposed methodology is schematically represented in the flowchart presented in figure 4.4.

4.5. EXPERIMENTAL ASSESSMENT

An experiment is conducted in the Aerodynamics Laboratory of TU Delft to assess the effectiveness of the proposed methodology. The near-wake of a 10 cm diameter truncated cylinder, characterized by a height/diameter ratio of 1, is investigated in a low-speed wind tunnel (W-Tunnel) equipped with an open test section of 60 × 60 cm^2. The free-stream velocity is set to 5 m/s, which implies a Reynolds number based on the cylinder diameter D equal to 3.3×10^4. The cylinder is positioned in the mid-span of a flat plate, equipped with a tripping device past the leading edge to force laminar to turbulent boundary layer transition. The shape of the plate leading edge is cubic super-elliptical of axis ratio 6 to minimize flow separation occurrence (Narasimha, Prasad, 1994). A measure-

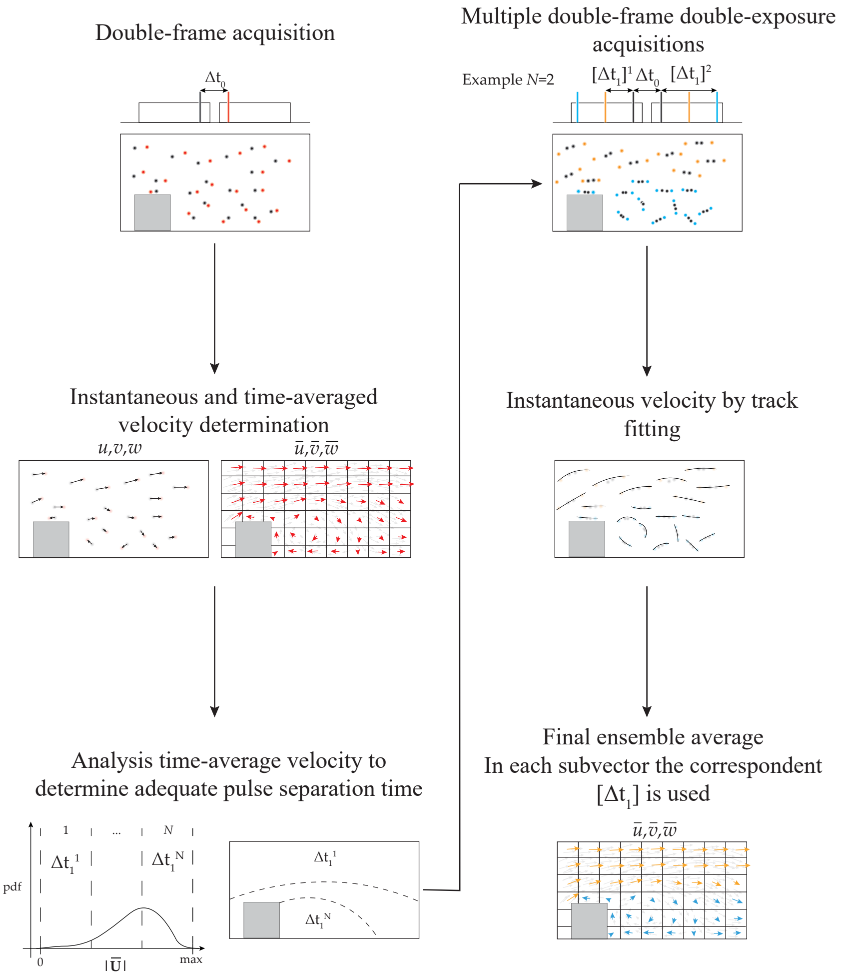

Figure 4.4: Schematic representation of the flowchart of the methodology proposed in this chapter.

ment volume of $25 \times 20 \times 20$ cm^3 captures the near-wake of the truncated cylinder. The measurement setup is shown in figure 4.5. The flow is seeded with helium-filled-soap-bubbles (HFSB), generated by a 50×100 cm^2 seeding rake positioned in the settling chamber of the wind tunnel. The generator contains 200 bubble-producing nozzles, which nominally produce 30,000 bubbles per second each (Faleiros et al., 2019). In order to control the mass flow of soap, air and helium,

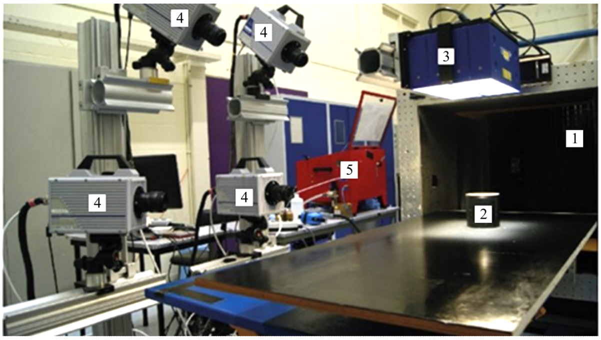

1. Wind tunnel exit
2. Truncated cylinder
3. LED arrays
4. Cameras
5. HFSB FSU

Figure 4.5: Picture of the experimental setup used to study the near wake of a square cylinder.

a homemade fluid supply unit (FSU) is used. Two LaVision LED-Flashlight 300 illumination units positioned above the cylinder illuminate the measurement region, imaged by four Photron Fast CAM SA1 cameras (CMOS, 1024 × 1024 pixels, 12 bits). Three of the cameras are equipped with 50 mm objectives, while one (the closest to the cylinder) is equipped with a 35 mm objective. To evaluate the performances of a new algorithm it is common to use synthetic datasets for which a reference is available and the comparison between the results of each technique is easily comparable. Several examples of this strategy are presented in the literature (Sciacchitano et al., 2012; Novara, Scarano, 2013; amongst others). One conclusion from these works is that replicating the measurement error in a synthetic dataset is far from being straightforward. For this reason, for this study, a full experimental assessment has been performed. The needed reference has been created by sampling the flow with a relatively high frequency at 5 kHz ($\Delta t = 0.2$ms) to create relatively long tracks (more than 20 expositions). The acquired images (2 datasets of 7000 images each) have been then processed with the PTV algorithm STB. For each of the reconstructed particle tracks, particle positions have been fitted with a least-square regression, as discussed by Schanz et al. (2016). The tracks obtained from the two acquisitions have been then combined, obtaining 5×10^5 tracks in total, which are considered as references for the application of the other approaches. To apply both the standard double-frame

PTV, the 4-pulses approach by Sellappan et al. (2020), hereafter referred to as static 4P-2F, and the method proposed in this study, referred as adaptive 4P-2F, double-frame datasets are needed. In order to be able to quantitatively evaluate the performances of the different approaches, the particle reconstruction in a 3D space, usually performed by IPR, has been substituted with direct input from the tracks computed by STB. For each of the tracks, the raw particle positions at the select time instants are considered, as schematically shown in figure 4.6, and used to evaluate the velocity according to each of the analyzed methods. The main difference between the static and the adaptive 4P-2F methods is visualized in figure 4.6. While in the region characterized by a high particle displacement, such as the freestream, the two methods adopt the same pair of pulse separation times $[\Delta t_0, \Delta t_1]$, the inter-frame pulse separation time Δt_1 is increased for the adaptive 4P-2F where the displacement decreases, such as in the recirculation or separation regions. The results obtained by applying the different timing schemes are presented in the next section.

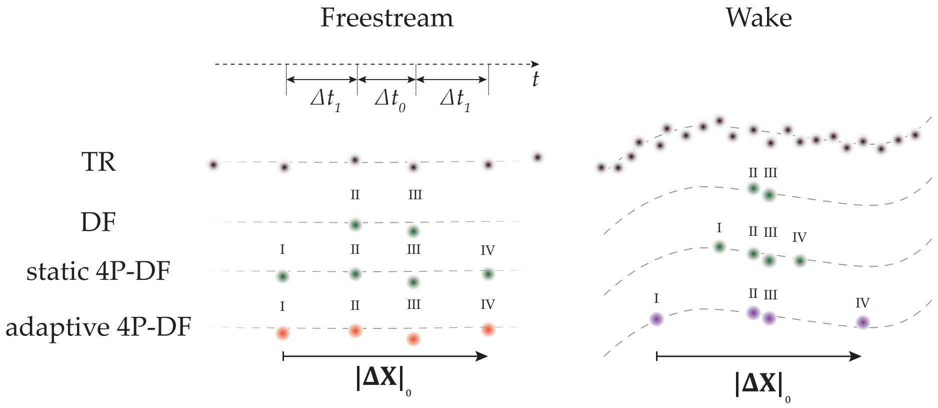

First Frame: I and II
Second Frame: III and IV

Figure 4.6: Schematic representation of the mechanism behind the particle selection to generate the multi-frame datasets from the STB tracks. The difference between the static and the adaptive 4P-DF emerges in the region of low velocity, where the intra-frame pulse separation time Δt_1 is increased to obtain a constant particle displacement $|\Delta \mathbf{X}|_0$.

4.6. RESULTS

Applying STB to all the acquired time-resolved images, a total of 5.5×10^5 tracks were obtained. A subsample of them is presented in figure 4.7 (left), where the lines are coloured based on the particle velocity. Figure 4.7 (right) shows the velocity field along the centre plane obtained by ensemble averaging the Lagrangian particle velocities in subvolumes of $3 \times 3 \times 3$ cm^3 with an overlap of 75%, producing a final grid with a vector pitch of 7.5 mm. The flow in the back of the cylinder shows the characteristics of the near wake of a bluff body. A region of reverse flow is visible on the top surface of the cylinder, with the flow separating at the leading edge. Above the separation region, accelerated flow is measured. This is due to the streamline curvature due to the flow separation on the top surface. The near-wake of the cylinder is characterized by the presence of a recirculation region that extends until $X/D = 1.5$.

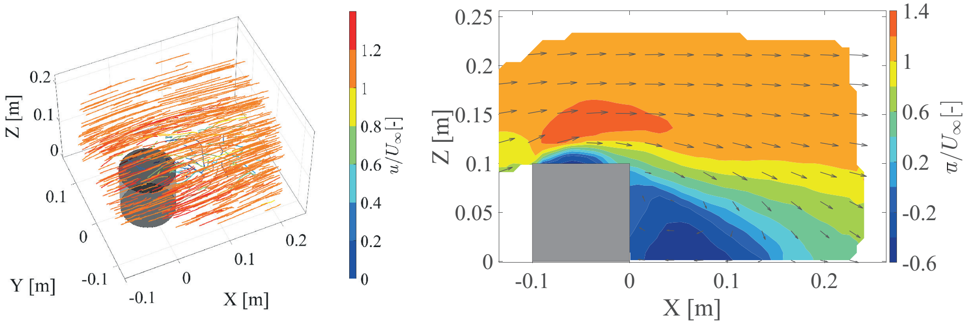

Figure 4.7: (left) Snapshot of a subset of the instantaneous Lagrangian particle tracks coloured by their normalized streamwise velocity. (Right) Representation of the time-average velocity field $\overline{u}$ normalized by the freestream velocity U_∞ along the plane $Y = 0$ mm.

Figure 4.8 (left) presents the fluctuating component of the streamwise velocity obtained by STB. It is noticeable the effect of the shear layer that is caused by the separation at the leading edge of the top surface of the cylinder, where the fluctuating component overcomes 50% of the freestream velocity. Moving downstream, the shear region diffuses and increases its size while decreasing the level of fluctuations to 35% at the centre of the recirculation region. figure 4.8 (right) illustrates the spatial distribution of the local DVR evaluated by equation

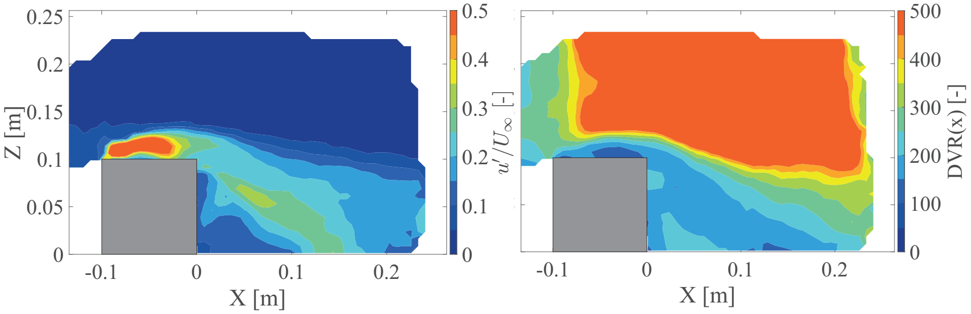

Figure 4.8: (Left) Contour of the root-mean-square of the normalized streamwise velocity fluctuations u'/U_∞ given by STB at $Y = 0$ mm. (Right) Contour of the local DVR for STB at $Y = 0$ mm.

4.3. In order to determine the relative uncertainty of the velocity, the relative uncertainty of the particle position ε_x is needed. To evaluate the latter, the average of the discrepancy between the raw and the fitted particle position is used, following the equation:

$$\varepsilon_x = \frac{1}{k}\sum_{i=1}^{k} |\mathbf{X}_{\mathrm{i,raw}} - \mathbf{X}_{\mathrm{i,fit}}| \tag{4.6}$$

The value of DVR depends on the local particle displacement and varies between $O(10^3)$ in the freestream region, where the displacement is maximum, to $O(10^2)$ in the separation region above the top surface of the cylinder. The low uncertainty of the velocity determination allows to use of the STB particle tracks as a reference for the evaluation of the three mentioned techniques: double-frame single exposure (DF), 4-pulse double-frame with fixed time separation (static 4P-2F) and the proposed adaptive algorithm based on 4-pulse double-frame with variable time separation recordings (adaptive 4P-2F).

The first method analyzed is the double-frame single exposure (DF), with a pulse separation time $\Delta t_0 = 2\Delta t_{STB}$. To evaluate the precision of the measurement, two different parameters are here calculated: the local DVR evaluated following equation 4.3 and the local difference between the reference and the calculated field, evaluated as:

$$\Delta = |u_{DF} - u_{STB}| \tag{4.7}$$

which is calculated for each track. To evaluate the spatial variation of Δ, its value is spatially averaged through the same ensemble process described for the veloc-

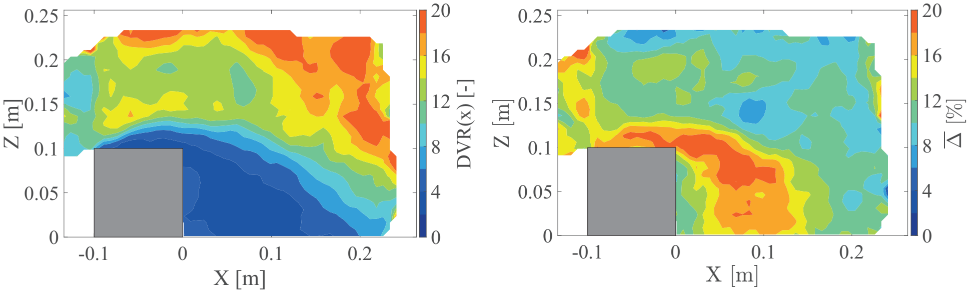

Figure 4.9: (Left) Contour of the local DVR obtained by DF at $Y = 0$ mm. (Right) Contour of the mean deviation $\overline{\Delta}$ between DF result and the reference, as a percentage of the freestream velocity.

ity.

Figure 4.9 (left) shows the spatial distribution at $Y = 0$ mm of the local DVR evaluated as prescribed by equation 4.3. Its value varies drastically within the measurement volume, reaching its maximum in the freestream region (DVR $\sim$ 20). In the near wake, more specifically in the recirculation region, its value drops below 4 due to the small particle displacement. The same region is characterized by the highest deviation between the instantaneous velocity measured by STB and DF, which reaches peaks of $\sim 20\%$, as shown in figure 4.9 (right).

To evaluate the performance of the static 4P-2F method, the following timing strategy is selected: $\Delta t_0 = \Delta t_{\mathrm{STB}}$ and $\Delta t_1 = 2\Delta t_{\mathrm{STB}}$. Once the four particles are selected from each of the STB tracks, a second-order polynomial fit is evaluated through the raw positions of the selected particles. The adoption of a multi-exposure strategy leads to an increase in the obtainable local DVR, as shown in figure 4.10 (left). As for the DF method, the peak of DVR is reached in the freestream region above the cylinder. In this region, the increase of particle displacement doubles the obtainable DVR, reflecting the 100% increase of T. The effect of the time extension can be detected also in the recirculation region, where the obtainable DVR doubles as well, from ~ 5 to ~ 10. Figure 4.10 (right) presents the average deviation between the velocity calculated by STB and by the static 4P-2F method. A general reduction of $2-3\%$ is obtained in the entire field when compared to the DF method. To determine the pairs $[\Delta t_0, \Delta t_1]_n$ to be used for the adaptive 4P-2F method, the pdf of the distribution of absolute velocities of the predictor field (DF field in this case) has to be evaluated and is

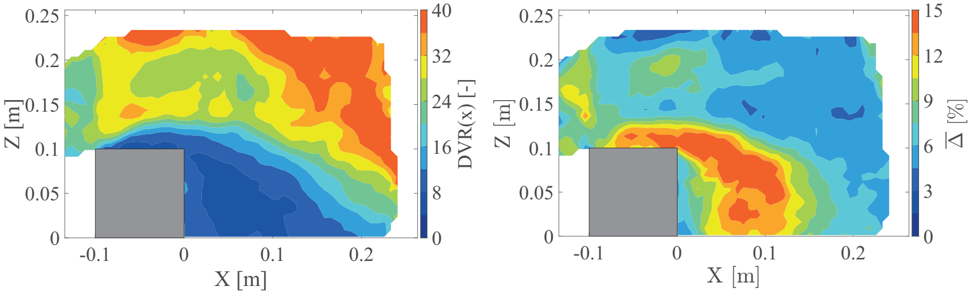

Figure 4.10: (Left) Contour of the local DVR obtained by static 4P-2F at $Y = 0$ mm. (Right) Contour of the mean deviation $\overline{\Delta}$ between static 4P-2F result and the reference, as a percentage of the freestream velocity.

Table 4.1: Distribution of pulse separation time pair given the local velocity.

Region #	Local flow velocity	Δt_0	Δt_1	T_n
1	$\lvert\mathbf{U}\rvert/U_\infty > 0.9$	Δt_{STB}	$2\Delta t_{STB}$	$5\Delta t_{STB}$
2	$0.45 < \lvert\mathbf{U}\rvert/U_\infty < 0.9$	Δt_{STB}	$4\Delta t_{STB}$	$9\Delta t_{STB}$
3	$\lvert\mathbf{U}\rvert/U_\infty < 0.45$	Δt_{STB}	$8\Delta t_{STB}$	$17\Delta t_{STB}$

shown in figure 4.11 (left). The entire range of velocities is equally divided into N subgroups and for each of them, a reference velocity V_n at the middle of the subrange is selected. The correspondent T_n is then evaluated using equation 4.5. It is decided to set N=3 to consider three pairs of $[\Delta t_0, \Delta t_1]_n$. Table 4.1 shows the pulse separation times selected in the three regions of different velocities.

Following the indication given in table 4.1, figure 4.11 (right) shows the regions where the different pulse separation time pairs are used. While in the freestream the time strategy is equal to the one used for the static 4P-2F method, the total time is stretched up to three times in the recirculation region to increase the particle displacement and in turn the DVR.

The increase in total displacement improves the precision of the velocity determination, as illustrated by the distribution of the local DVR shown in figure 4.12 (left). When compared to the DF strategy, the local DVR in the recirculation region increases by ≈ 150% while, compared to the static 4P-2F method, an increase of ∼ 50% is obtained. The increase in precision is detectable also when the deviation from the reference $\overline{\Delta}$ is evaluated, as shown in figure 4.12 (right). The increment of the total displacement allows for an increase in the precision of the

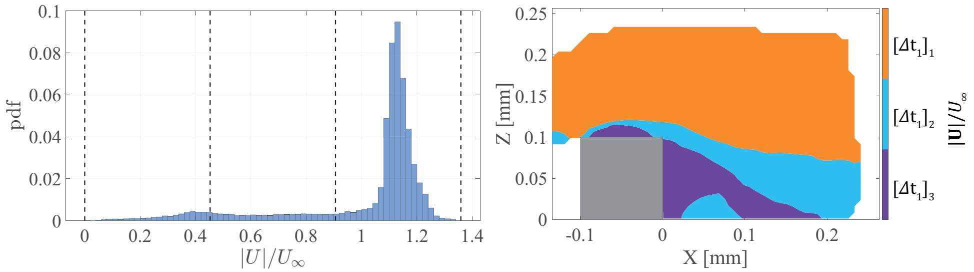

Figure 4.11: (Left) Distribution of the normalized absolute velocity |**U**| obtained by analysing the reference velocity field. (Right) Illustration of the spatial distribution of the time extension applied by the proposed methodology.

particle fit and reduces the discrepancy from the reference velocity, quantifiable in 28% in the wake region where the time stretching reaches the maximum.

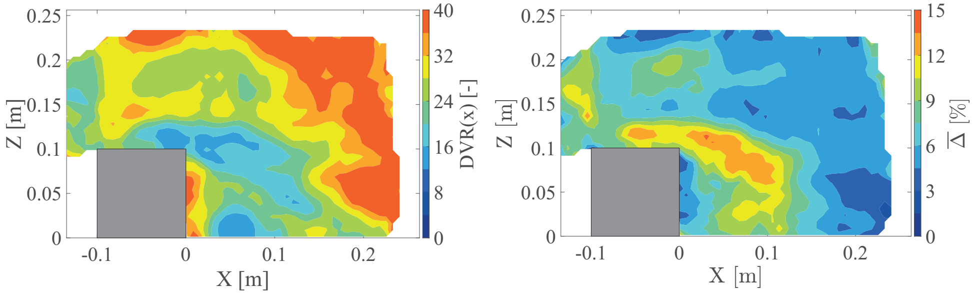

Figure 4.12: (Left) Contour of the local DVR obtained by the adaptive 4P-2F at $Y = 0$ mm. (Right) Contour of the mean deviation $\overline{\Delta}$ between the adaptive 4P-2F and the reference, as a percentage of the freestream velocity.

4.7. CONCLUSIONS

In this chapter, a new adaptive acquisition strategy has been presented. The method is based on a multi-step approach. Firstly, a double-frame single-exposure acquisition is analyzed and Reynolds decomposition is applied to the calculated flow field to obtain the time-averaged velocity . The use of a double-frame single-exposure strategy allows determining the velocity field in a robust but low precision manner. The predicted velocity field is used then to obtain a series of pulse separation times for the successive acquisition of a series of double-frame double-exposure datasets. The time separation pairs are selected to obtain a rather constant particle displacement across the measurement volume. Finally, the tracks computed analysing the different acquisitions are merged to produce the final description of the flow field. The proposed methodology has been tested considering the near-wake of a truncated cylinder. To quantitatively evaluate the performance of the mentioned algorithms, a reference has been constructed with the Lagrangian Particle tracking algorithm shake-the-box applied to a highly sampled dataset. The results show the benefit obtained by the increment of particle displacement in the region characterized by low velocities in terms of measurement precision. Further studies on the effect of particle concentration and truncation errors will be carried out in the future.

5

OUTLIER DETECTION BASED ON TURBULENCE TRANSPORT

Parts of this chapter have been published in:

- Saredi E, Sciacchitano A & Scarano F (2022) Outlier detection for PIV statistics based on turbulence transport. *Exp. Fluids* 63(1): 1-10

5.1. BACKGROUND

In Particle Image Velocimetry (PIV), outliers are spurious vectors that exhibit large unphysical variations in magnitude and direction from neighbouring valid vectors (Westerweel, 1994). Despite the above definition, most proposed and used approaches for outliers detection are not based on flow physics, but rather on statistical data analysis, as described in section 1.7.

The outlier detection methods presented are typically effective for the instantaneous velocity fields where a single vector or a cluster thereof largely departs in magnitude and direction from the neighbouring points. Such outliers need to be detected and replaced, or omitted, when estimating statistical flow properties like the mean value and its fluctuations. If not, they yield erroneous flow statistics, whereby the outliers depart less markedly from the neighbouring vectors and therefore are not easily detectable with state-of-the-art outlier detection approaches.

An early attempt to use constitutive equations for outlier detection is due to Song et al. (1999) who invoked compliance to the continuity equation, numerically evaluated from a Delaunay tessellation of the domain. For experiments in the incompressible flow regime, outliers would produce unphysical nonzero values of the velocity divergence. However, a unique value of the threshold that separates outliers from other acceptable sources of error (e.g. small amplitude measurement noise) could not be identified, as deductible from the data presented by Azijli, Dwight (2015). The advent of three-dimensional PIV techniques (Raf-

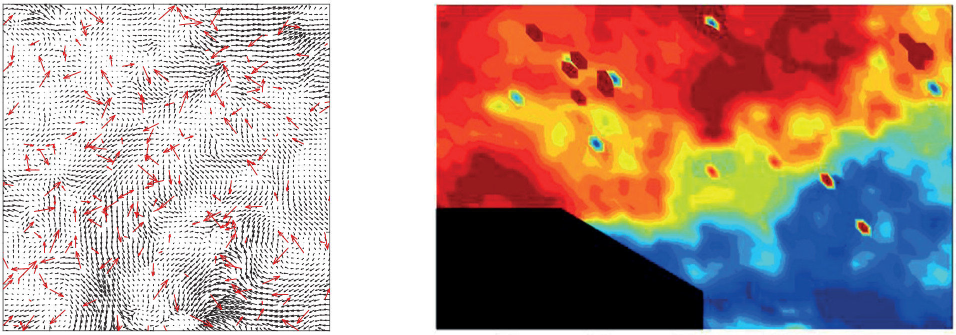

Figure 5.1: Example of the presence of outlier in PIV velocity fields. Results reproduced from Higham et al. (2016).

fel et al., 2007) and in particular particle-based analysis (Shake-The-Box, STB, Schanz et al., 2016) has established new approaches to evaluating the flow statistics from experiments. The instantaneous flow velocity is obtained directly at the sparse positions occupied by the particle tracers. Therefore, ensemble statistics are obtained by partitioning the domain into cubic voxels (or bins) arranged on a Cartesian grid and evaluating locally the ensemble average and fluctuations from all particle velocities belonging to the considered voxel. Techniques that perform accurately this operation have been devised by Agüera et al. (2016) and more recently by Godbersen, Schröder (2020).

The occurrence of outliers in PTV data is notably more frequent than in data produced with cross-correlation analysis (2nd PIV challenge, Stanislas et al., 2005), thus bringing forward the problem of outliers detection from ensemble statistics of 3D-PTV data. In the present work, the principle of using constitutive equations for the detection of outliers from statistical datasets is revised, invoking the turbulence transport equation as a consistent choice.

5.2. TURBULENT TRANSPORT DETECTION CRITERION

5.2.1. WORKING PRINCIPLE

Let us consider a statistical dataset whereby the measured velocity is represented by means of the Reynolds decomposition into the mean and fluctuating part. Taking for instance the streamwise velocity component u, such decomposition reads as:

$$u = \overline{u} + u' \tag{5.1}$$

The turbulent kinetic energy (TKE, here denoted by the symbol k) considers the statistical fluctuations from all velocity components:

$$k = \frac{1}{2}(\overline{u'}^2 + \overline{v'}^2 + \overline{w'}^2) \tag{5.2}$$

and its behaviour is governed by the turbulence transport equation (Hinze, 1967):

$$\frac{Dk}{Dt} = T + P - \varepsilon \tag{5.3}$$

The above expression states that the variation of TKE of a fluid parcel is governed by transport T, production P and dissipation ε. The main question raised here is to what extent can the occurrence of a statistical outlier be detected by invoking the above physical principle. For further use, the terms of equation 5.3 are explained below:

$$\frac{Dk}{Dt} = \frac{\partial k}{\partial t} + A \text{ material derivative of } k, \tag{5.4}$$

$$A = u_i \frac{\partial k}{\partial x_i} \text{ advection,} \tag{5.5}$$

$$P = -\overline{u'_i u'_j}\frac{\partial \overline{u_i}}{\partial x_j} \text{ production,} \tag{5.6}$$

$$T = -\frac{1}{2}\frac{\partial \overline{u'_i u'_i u'_j}}{\partial x_j} + \nu \frac{\partial k^2}{\partial x_i \partial x_j} - \frac{1}{\rho}\frac{\partial \overline{u'_j p'}}{\partial x_i} \text{ transport,} \tag{5.7}$$

$$\varepsilon = \nu \overline{\frac{\partial u'_i}{\partial x_j}\frac{\partial u'_i}{\partial x_j}} \text{ dissipation.} \tag{5.8}$$

From a recent review of studies describing the TKE budget (Ikhennicheu et al., 2020), in turbulent shear flows, a first approximation of the behaviour for the turbulent quantities is that of quasi-equilibrium turbulence, whereby the turbulent properties vary very gradually along a streamline. Under this condition, the production and the dissipation are the dominant terms at the right-hand side of equation 5.3, with the former acting as the upper bound of the convection of TKE along a streamline, since a non-null dissipation reduces the TKE. It is hypothesized here (and illustrated in the considered experiments of section 3) that the presence of data outliers generally leads to an overestimation of TKE and locally biases the RMS fluctuations. This condition can be detected as unphysical, invoking a criterion based on equation 5.3 or a derived form of it as shown in the remainder.

5.2.2. DETECTION CRITERION

The interaction of outliers and turbulence transport is first illustrated schematically. Let us consider the statistical dataset from the measurements around an airfoil at incidence (figure 5.2), which corresponds to one of the experiments presented in the remainder. The measurement yields the statistical description of the velocity field $\overline{\mathbf{V}}$, $\mathbf{V}'$ and an estimate of the velocity fluctuations k. Flow separation from the leading edge results in a large flow recirculation bounded by turbulent shear layers. The laser light refraction at the edges of the transparent airfoil produces regions with no illumination (indicated as A and B in figure 5.2). Additionally, two small regions of outliers are hypothesised (region A ahead of the airfoil and region D in the shear layer) as resulting from background light reflections. In the above regions, a significantly more frequent occurrence of outliers is hypothesized, in turn causing a localised overestimation of the TKE. However, let us recall that along any time-average streamline, the evolution of k must comply with equation 5.3. Therefore, following a streamline that crosses a region of outliers, it is expected that the absolute variation of TKE along the streamline $|\frac{\partial k}{\partial \xi}|$ will largely exceed the value allowed by equation 5.3. When outliers appear featuring a cluster, the principle is violated at its upstream and downstream edges. In the irrotational regions (A, B and C of figure 5.3) k is expected to remain constant and close to null (laminar shear free flow), alongside its spatial derivative along the streamline, i.e. $|\frac{\partial k}{\partial \xi}| = 0$ (light blue line in figure 5.3). The occurrence of outliers in the measurement will produce a visible increase of $|\frac{\partial k}{\partial \xi}|$ at the upstream and downstream edges. Taking into consideration some measurement noise for a threshold level (black dashed line in figure 5.3), a single value of $|\frac{\partial k}{\partial \xi}|$ may allow detecting the data at the upstream boundary as erroneous. In the regime of turbulent shear (region D in figure 5.3-right) instead, the variation of k along the streamline is not expected to be null, with the term P dominating the righthand side of equation 5.3. A threshold must be based on an estimate of the local production of turbulence, which requires the measurement of the shear rate and the Reynolds stress tensor. Based on the above discussion, one can define a criterion that states the admissible value for TKE advection along a streamline, compared to an estimation of TKE production:

$$\rho_{TT} = \frac{|A|}{|P|} \tag{5.9}$$

Such admissible values of ρ_{TT} are to be of O(1) or smaller. Moreover, con-

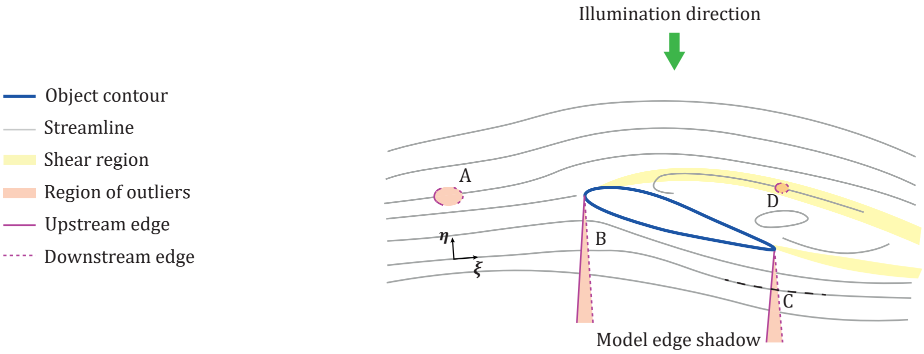

Figure 5.2: Flow around an airfoil at incidence. The separated region at the suction side is bounded by free shear layers. Outlier regions are highlighted in light red: A, B and C in the external flow around the airfoil; D inside the shear layer. Red continuous and dashed lines mark the upstream and downstream edges of each region.

sidering that the estimation of P, performed considering the unscrutinised velocity field, is affected by measurement noise, the production term in equation 5.9 is replaced with the median P_m of the adjacent vectors in a kernel 5×5, in analogy to (Westerweel, Scarano, 2005). Similarly, to avoid the ratio losing significance when the production is null (for instance in regions of laminar flow, free of shear), an additive term ρ_{TT} is included on the denominator that scales with the uncertainty on the numerator A of equation 5.9. With the latter modifications, equation 5.9 becomes:

$$\rho_{TT} = \frac{|A|}{|P_m| + \gamma_{TT}} < 5 \tag{5.10}$$

Due to the statistical nature of the terms of equation 5.10, it must be underlined that the presented approach is only meant for flow statistics and cannot be directly applied to instantaneous velocity fields. A suitable value for the term γ_{TT} can be estimated assuming that the velocity is measured with uncertainty not exceeding 5% of a reference velocity, e.g. V_∞:

$$\gamma_{TT} = \frac{(0.05 V_\infty)^3}{\Delta} \tag{5.11}$$

with Δ representing the pitch of the grid where the velocity vector field is evaluated. Equation 5.10 is written already in the form of a detection criterion, whereby

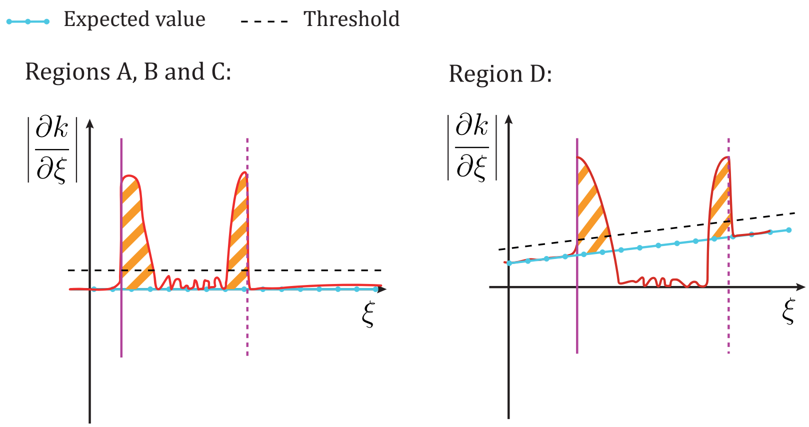

Figure 5.3: Schematic representation of the expected variation of turbulent kinetic energy along a streamline. At the boundaries of the erroneous region, an unphysical increase of TKE flags erroneous vectors.

a threshold value of 5 is proposed here that separates admissible (unit order of magnitude) from non-admissible (higher order of magnitude) values of ρ_{TT}. The above choice is scrutinised with the application of the criterion to data gathered in wind tunnel experiments.

5.3. EXPERIMENTAL ASSESSMENT

5.3.1. SELECTED DATASETS

Three experimental datasets have been considered: the 2D velocity field around a NACA 0012 airfoil, the near-wake of a truncated cylinder and that of the Ahmed body (Ahmed et al., 1984). Planar, two-component PIV measurements are taken for the airfoil case. The flow is seeded with water–glycol droplets of 1 μm median diameter. Illumination is provided by a Quantel *Evergreen* 200 Nd:YAG laser (2 × 200 mJ at 15 Hz), and the illuminated particles are imaged by a LaVision Imager sCMOS camera (2560 × 2160 pixels, 16 bits). A description of the setup can be found in Adatrao et al. (2021). Figure 5.4a shows an instantaneous recording featuring, aside from uniform seeding concentration, shadow region emanating from the leading edge. Multi-pass, 2D cross-correlation analysis is used to evaluate the particles' motion. For the near-wake of the cylinder, a tomo-

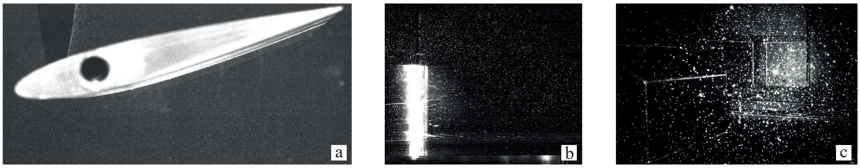

Figure 5.4: Raw images from the three experiments. **a** NACA 0012 airfoil; **b** near-wake of a truncated cylinder; **c** near-wake of the Ahmed body.

graphic PIV system was used. In order to achieve a measurement volume of 6 L, sub-millimetre helium-filled-soap-bubbles (HFSB) have been used as tracer particles (Faleiros et al., 2019; Scarano et al., 2015a). The illumination was provided by a Quantronix *Darwin Duo* Nd:YLF laser (2×25 mJ at 1 kHz). The imaging system comprised four high-speed Photron FASTCAM SA1 cameras (1024×1024 pixels, 10 bits) featuring a tomographic system with a large aperture (Schneiders et al., 2016). The region of interest is illuminated from downstream, and the round shape of the cylinder surface produces strong reflection towards two of the cameras, placed at the same height as the model. A raw image with such reflection is shown in figure 5.4b. The recordings were analysed with the STB algorithm (Schanz et al., 2016), yielding the particles' velocity along their trajectory. Ensemble-average over cubic bins was performed returning the time-average velocity and its fluctuations on a Cartesian grid. The near-wake of Ahmed body was investigated by Saredi et al. (2020) using robotic volumetric PIV (Jux et al., 2018). HFSB were used to seed the flow stream. The technique makes use of a coaxial volumetric velocimeter (Schneiders et al., 2018), whereby the laser light propagates approximately along the same direction as that of the four CMOS imagers composing the LaVision Minishaker (1920×1200 pixels, 10 bits). As a result, the recorded images tend to collect light reflected from objects and the illuminated background. The situation is illustrated in figure 5.4c. The particle motion is obtained with STB in a way similar to the previous case. The main experimental parameters of the three considered datasets are listed in Table 5.1.

Table 5.1: Measurement parameters for the three considered experiments

Experiment	NACA 0012	Near-wake truncated cylinder	Near-wake Ahmed body
2D/3D	2D	3D	3D
N. snapshots	1000	2000	10000
Seeding	Fog droplets ($d_p = 1$ µm)	HFSB ($d_p = 300$ µm)	HFSB ($d_p = 300$ µm)
Illumination	Nd:YAG laser (2 × 200 mJ @ 15 Hz)	Nd:YLF laser (2 × 25 mJ @ 1 kHz)	Nd:YLF laser (2 × 25 mJ @ 1 kHz)
Rec. device	sCMOS (2560 × 2160 px^2, 16 bits, 6.5 µm pixel pitch)	CMOS (1021 × 1024 px^2, 12 bits, 20 µm pixel pitch)	CMOS (1021 × 1024 px^2, 12 bits, 20 µm pixel pitch)
Rec. method	Double frame single exposure	Time-resolved single exposure	Time-resolved single exposure
Proc. tech.	Cross-correlation	STB	STB

5.3.2. VELOCITY FIELD STATISTICS

The error sources described above introduce outliers at random time instants. This process is illustrated in the example of figure 5.5 in the left column, where the instantaneous measurement features isolated outliers and, more importantly, regions of finite extent with a large fraction of unphysical data. The cross-correlation analysis fails in the shadow region above the airfoil, which leads to random velocity vectors. For the cylinder case, the strong reflection on the surface of the body causes the appearance of erroneous particle tracks along one of the tomographic lines of sight. These tracks feature high-amplitude errors. The unphysical values extend also inside the solid object. The background reflection in the case of the Ahmed body wake introduces erroneous tracks in the free-stream region. Also, in this case, this region extends along the viewing direction. The outliers that appear in the instantaneous fields are markedly departing from the correct measurements. When the statistical dataset is built to evaluate the time-average velocity field (figure 5.5, centre-column), such departure becomes less evident as a result of the statistical averaging between spurious and correct data. For the 2D-wing case, the region corresponding to both the shadow and the perspective section of the wing is characterized by erroneous low velocity. For the cylinder case, laser reflections generate invalid vectors inside the cylinder geometry. Furthermore, a region of flow characterized by quasi-null streamwise velocity can be spotted in the area corresponding to the erroneous tracks. Such areas are highlighted with dashed ellipses in figure 5.5. Similarly, the presence of spurious tracks in the near-wake of the Ahmed body produces an unphysical region of deceleration and acceleration at $X = 0.2$ m in the free-stream region of the ensemble-averaged flow field. The effect of instantaneous velocity outliers affects even more markedly the RMS velocity fluctuations (figure 5.5, right column). This effect is illustrated here by displaying the quantity $\sqrt{k}/V_\infty$. All outlier regions feature a sharp increase of TKE with respect to the surrounding. It can be noted that the extent and the shape of the outlier regions are more visible for the velocity fluctuations rather than for the time-averaged velocity. However, the TKE alone can hardly be used as a criterion for outliers detection, because its values are not bounded by criterion and the threshold for admissible values varies greatly among experiments. For instance, while for the airfoil case, $\sqrt{k}/V_\infty < 0.4$ would be an appropriate criterion to identify the entire erroneous data caused by the shadow, the same threshold would introduce false positives (i.e. flag correct measurements as erroneous) in the shear region of the cylinder wake.

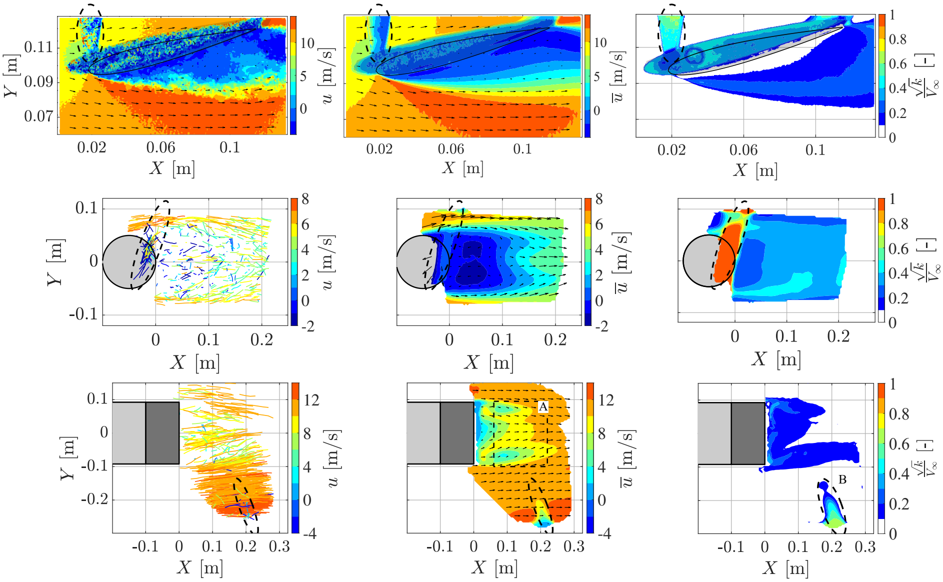

Figure 5.5: Left: Instantaneous velocity vectors or tracks. Centre: time-averaged velocity vectors; region A is used for determining η_{fp} (figure 5.7). Right: normalized fluctuations, $\sqrt{k}/V_\infty$. Outliers regions are highlighted by a dashed ellipse; region B is used to determine η_d (figure 5.7). For the 3D datasets, the data are presented in a slice crossing the outlier region ($Z = 0.13$ m for the Ahmed body, $Z = 0.05$ m for the cylinder).

5.3.3. COMPARISON WITH STATE-OF-THE-ART OUTLIER DETECTION

The effectiveness of the turbulence transport-based criterion is compared to the universal outlier detection (UOD, Westerweel, Scarano, 2005). Firstly, the principle of the latter are here discussed. In their work, the authors proposed a new methodology where outliers are identified by a median-based residual r_0^* defined as:

$$r_0^* = \frac{|V_0 - V_m|}{r_m + \gamma_{UOD}} \tag{5.12}$$

where V_0 is the considered velocity vector, V_m the median value across its neighbourhood, r_m the median of the neighbours' residuals defined as $r_i = |V_i - V_m|$, and γ_{UOD} is the minimum normalization level, often set to 0.1 pixels. The UOD criterion has been postulated, based on experiments as $r_0^* > 2$ and the same threshold value is used in the present analysis. In the original paper, the criterion has been tested considering a variety of velocity fields obtained by 2D PIV. The application of the two outliers indicators to the present data, namely ρ_{TT} of equation 5.10 and the residual r_0^* of equation 5.12, is presented in figure 5.6. The condition $r_0^* > 2$ does not detect false vectors for the airfoil and the cylinder case. In the former, only a small region at the leading edge of the shadow would be considered erroneous.

In the latter, the area affected by reflection is not detected as erroneous, with only some vectors at the edges of the flow domain indicated as outliers. The same criterion does detect erroneous vectors in Ahmed body wake. However, also correct measurements in the shear layers are labelled as outliers (false positives). In the right column of figure 5.6 the ρ_{TT} criterion is displayed. The highest value is attained at the edges of the erroneous regions, ($\rho_{TT} > 10$), well separated, by approximately one order of magnitude, with respect to the adjacent correct measurements. The edges of the airfoil shadow region and the edges of the area blocked by the perspective view are clearly detected as false vectors. The edges of the erroneous region in the cylinder wake are also clearly detected, again with a large separation to the correct portion of the flow where $\rho_{TT} \sim 1$. In the Ahmed body wake, ρ_{TT} correctly detects the boundary of the erroneous region highlighted by the dashed ellipse in figure 5.6 (right). Two regions at the back edge of the Ahmed body are also highlighted as erroneous, suggesting the presence of false positives for ρ_{TT} too, in those regions.

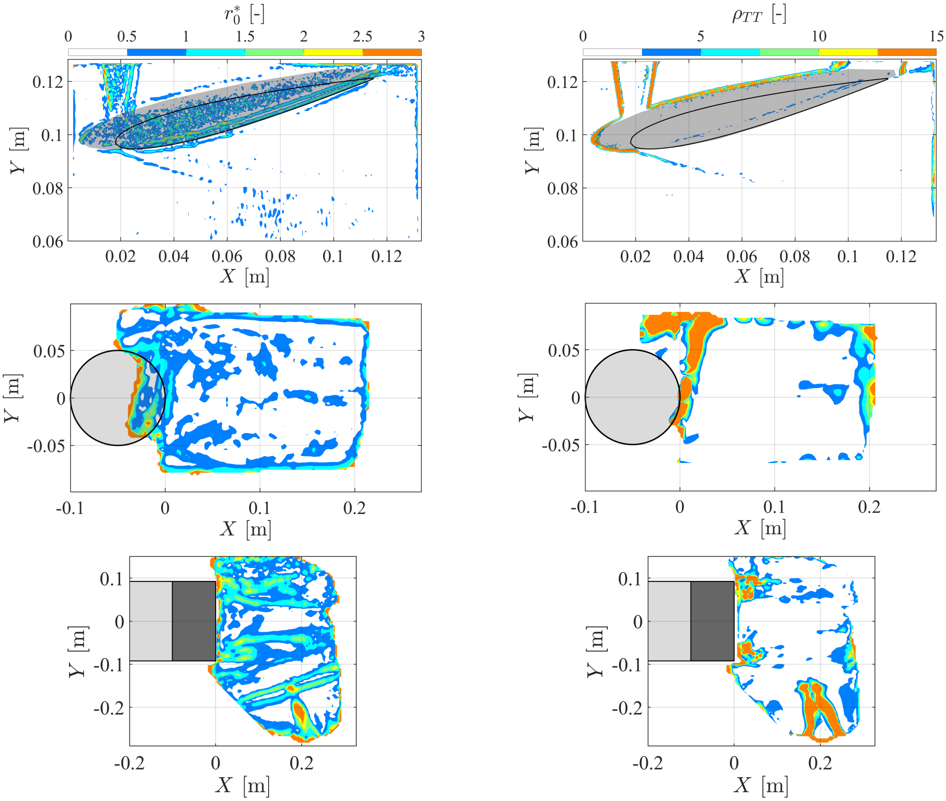

Figure 5.6: Left: normalized residual r_0^* of the UOD criterion (Westerweel, Scarano, 2005). Right: turbulence transport ratio ρ_{TT} defined by equation 5.10. For the 3D datasets, the data are presented in a slice crossing the outlier region ($Z = 0.13$ m for the Ahmed body, $Z = 0.05$ m for the cylinder).

5.3.4. DETECTION RATIO AND FALSE POSITIVE

The performance of the above detection methods is assessed by introducing the detection and false positive rates η_d and η_{fp}, respectively. The former is defined as the number of spurious vectors correctly flagged as erroneous divided by the total number of outliers. The false positive rate η_{fp} is defined as the ratio of correct vectors flagged detected as outliers and the total number of correct vectors. The criterion robustness is defined by how constant the above two parameters remain by varying the threshold. It is chosen to vary the UOD criterion between

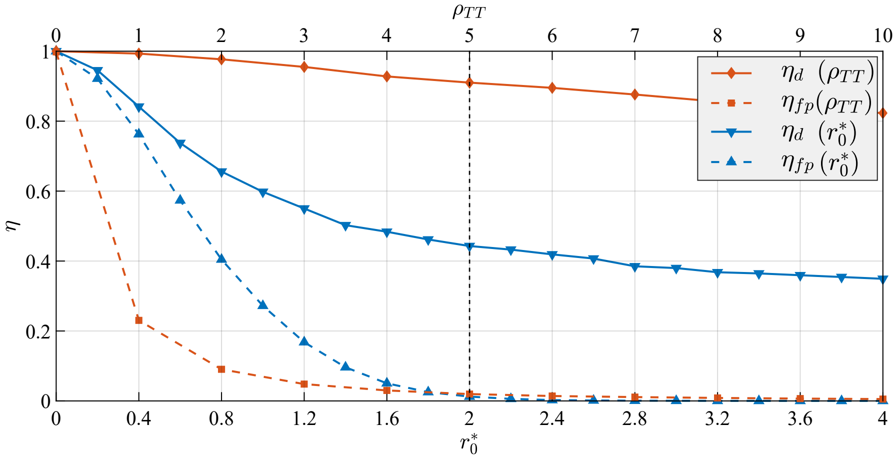

Figure 5.7: Comparison of the detection ratio η_d and the false positive ratio η_{fp} obtained by UOD and ρ_{TT}. Data extracted from Ahmed body near wake.

0 and 4 and ρ_{TT} between 0 and 10. A portion of the dataset in the near-wake of the Ahmed body has been considered where the presence of erroneous vectors can be clearly excluded, yet the flow exhibits significant shear and turbulence. The planar section of the considered volume is indicated as region A in figure 5.5 (centre). Instead, for the estimation of η_d erroneous vectors need to be known with a high level of confidence. In this case, the area circled and indicate as region B in figure 5.5 (right) has been considered. The proposed principle aims to detect erroneous vectors at the edge of correct measurement regions; only the vectors located at the edge of the faulty area have been considered. Once isolated, this group of vectors, the amount of them flagged as erroneous by the UOD and by the turbulence transport-based outlier detection has been calculated. The results obtained in terms of η_d and η_{fp} by the two methods, varying the corresponding thresholds, are presented in figure 5.7. It has to be noted that the optimal values of η_{fp} and η_d are 0 and 1, respectively. It is expected that, when increasing the value of the threshold for both criteria, the correct detection probability decreases, alongside the false positive rate. Both criteria yield the same expected behaviour. The UOD criterion features a rapidly declining detection rate, with a value of approximately 50% for $r_0^* = 2$. At this point, the fraction of less than 5% for the false positives is acceptably small. The turbu-

lence transport-based criterion detects approximately 90% of the erroneous vectors with a threshold of 5, with a fraction of false positives similar to that of UOD. Moreover, the difference subtended between η_d and η_{fp} remains rather in a wide range of values for the threshold: $\Delta\eta > 0.8$ when $\rho_{TT} \in [1,10]$. In contrast, such difference is limited to 0.4 for UOD in the range $r_0^* \in [1,3]$.

An additional indication of the outlier detection stability can be obtained by examining the fraction of detected outliers with respect to a variation of the threshold. The histograms of r_0^* and ρ_{TT} are shown in figure 5.8. Similarly to the results in figure 5.7, both methods yield a decreasing number of detected vectors with an increasing value of the threshold. A significant difference is observed in the slope of the curves corresponding to the two criteria. While for the UOD criterion, a unit change of r_0^* causes a variation by a decade in the histogram (slope 10^{-1}), the same change of ρ_{TT} introduces a negligible variation of detected outliers (slope $10^{-1/6}$). It is thus concluded that the detection of outliers based on the turbulence transport principle is a significantly more stable estimator of sta-

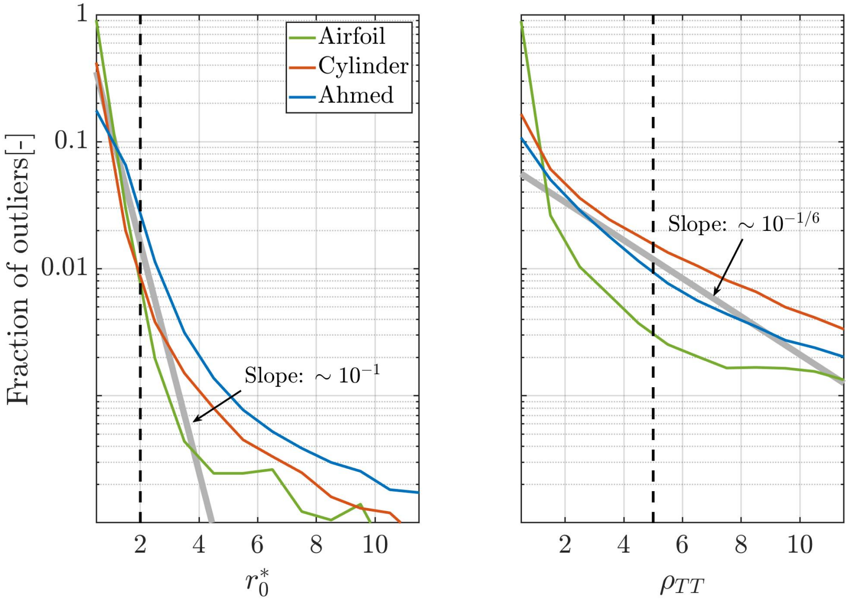

Figure 5.8: Histogram of detected outliers by UOD (left) and ρ_{TT} (right) and their commonly selected threshold value (vertical dashed black line). Thick grey lines indicate the average slope of curves.

tistical outliers alongside yielding minimal occurrence of false positives.

5.4. CONCLUSIONS

A novel outlier detection criterion is presented that invokes the physical principle of turbulence transport and applies to the flow statistics evaluated by PIV or PTV, preferably in 3D datasets. The approach relies on the fact that the measured velocity fluctuations are bound to comply with the governing equation of turbulent kinetic energy transport. The ratio of advected turbulent kinetic energy with the production term along a given trajectory is at the basis of the proposed criterion. A robust implementation of the method applies the median operator for the production term and an additive term that avoids a null denominator. The method is verified with data from three different experiments, including planar, tomographic 3D-PTV and 3D-PTV measurements by coaxial volumetric velocimetry. The outlier detection principle based on turbulence transport detects the edges of regions of outliers, mostly caused by extensive regions of light reflection or shadows in the measurements. The method compares favourably with the state-of-the-art UOD from the analysis of the experimental datasets. Considering the two optimal thresholds, $r_0^* = 2$ and $\rho_{TT} = 5$, the latter yields a significantly higher detection ratio η_d with a comparable and small amount of false positives (η_{fp}). For extended regions of outliers, the method requires multiple erosion iterations.

6

DATA ASSIMILATION WITH TIME-AVERAGED 3D-PIV DATA

Parts of this chapter have been published in:

- Saredi E, Ramesh NT, Sciacchitano A & Scarano F (2021) State observer data assimilation for RANS with time-averaged 3D-PIV data. *Comp. Fluids* 218: 104827

6.1. BACKGROUND

The state observer algorithm, originally proposed by Luenberger (1964) is nowadays a key concept of the control theory, based on a feedback term in the modelling equation. The intensity of the feedback is a function of the difference between the model results and the reference (viz. experimental) data multiplied by a gain factor. The latter is usually tuned to maximise the convergence rate. The design of the feedback and its law of application is the key point of a state observer algorithm (Hayase, 2015). Hayase, Hayashi (1997) applied a state observer algorithm to improve the simulation of a fully developed turbulent square duct. The authors modified the pressure boundary conditions at the inlet and the outlet with a proportional law in order to reduce the error between the simulation and the ground truth, which in that case was a pre-calculated numerical solution performed on the same mesh with a different initial condition. The application of the feedback gave an accelerated convergence of the simulation and a reduction of one order of magnitude in the final error across the whole domain. This approach alleviates the errors given by the erroneous boundary conditions but is not able to tackle the error given by the approximation performed in the turbulence modelling.

Imagawa, Hayase (2010) performed a Measurement-Integrated (MI) simulation for the turbulent flow along a square duct and applied feedback by means of a body force term in the momentum equation. The forcing term was linearly proportional (DASOP, which stands for data assimilation state observer proportional) to the difference between the velocity returned by the unsteady simulation and that from a reference simulation performed with the same numerical schemes on the same grid but with different initial conditions. The application of the feedback led to a reduction of the steady state error by four orders of magnitude when all the velocity components were forced at all the grid points. However, interrupting the assimilation during the simulation caused the system to converge again towards the non-assimilated solution. The authors also considered the case of a limited density of forcing points, forcing from one plane every four down to only one plane. They concluded that, with their forcing term, tuning the gain factor, it was possible to obtain the same error reduction considering one plane every four. Furthermore, by disabling the forcing term at a quarter of the total running time, the simulation was naturally converging towards the not assimilated simulation, with the effect of the forcing term effect that was vanishing. This shows a typical behaviour of a proportional controller, with the efficacy of the forcing term that reduces when the error reduces. Neeteson, Rival (2020) applied the state observer algorithm to the Karman vortex shedding problem at Re = 10^2, using a computational reference. They introduced a Proportional-Integral-Derivative (PID) control in the pressure equation, which was formulated as feedback law. The latter was more elaborate than the sole proportional law used in most previous works and aimed at solving the reduction of effectiveness of the forcing term at the low error stages. The application of the PID control law (DASOPID) improved the results compared to those given by the sole proportional feedback law, returning a vortex shedding behaviour closer to that of the reference data in terms of shedding frequency. The state observer algorithm has been used also with experimental data as a reference. Yamagata et al. (2008) studied the unsteady behaviour of the Karman vortex street behind a truncated cylinder at Re = 1.2×10^3 performing a MI simulation with planar PIV data input. The assimilation allowed the reproduction of the large-scale unsteadiness which is not obtained by ordinary simulations. The discussion above shows that the state observer data assimilation has been considered to enhance the accuracy of RANS-based CFD simulations, mainly in the unsteady flow regime and at low Re number. However, many applications of industrial aerodynamics are primarily concerned with the accuracy of the steady-state flow solution. Moreover, many relevant problems involve high Reynolds number flows and a fully turbulent regime for which many questions about the applicability and the potential of DA remain unanswered. This study considers steady-state simulations of the flow around a wall-mounted bluff obstacle, representing the geometry of a simplified car mirror presented by De Villiers (2006). The problem is studied at Re = 8×10^4. The reference time-averaged velocity field is obtained from experiments that make use of Robotic Volumetric PIV Jux et al., 2018. Two formulations of the State Observer forcing term are considered, namely Data-Assimilation-State-Observer-Proportional (DASOP) and Data-Assimilation-State-Observer-Proportional-Integral (DASOPI). Moreover, the work investigates the extent of the regions affected by the forcing point, to identify a criterion for optimum data assimilation forced points density. Finally, a metric is introduced to quantify the effect of DA methods and parameters on the accuracy of the assimilated solutions with respect to the reference velocity.

6.2. STATE OBSERVER DATA ASSIMILATION FOR RANS

Reynolds-averaged Navier-Stokes (RANS) equations are considered here as the framework for the numerical simulation of incompressible turbulent fluid flows. The *baseline simulation* is intended as the process leading to a solution (*baseline solution*) with no use of a-priori information from the experiments. The working principle of data assimilation is to introduce a certain amount of reference data, indicated here as $\mathbf{u}_{\mathrm{ref}}$, and force the simulation to comply with it. In this work, the resulting process is called the *assimilated simulation*, which returns the *assimilated solution*. The objective is to drive the assimilated solution towards a more correct evaluation of the relevant features present in the flow field (e.g. flow topology, separation, reattachment, pressure gradient distribution, aerodynamic loads and forces), thus minimising simulation errors, such as the ones associated with the turbulence modelling. The underlying concepts and equations of data assimilation through a state observer (DASO) algorithm are recalled here. Applying Reynolds decomposition and time averaging, the dynamic behaviour of a steady, incompressible, viscous and turbulent flow can be described by the RANS equations, formed by the combination of the conservation of mass and momentum, respectively:

$$\nabla \cdot \overline{\mathbf{u}} = 0 \tag{6.1}$$

$$(\overline{\mathbf{u}} \cdot \nabla)\overline{\mathbf{u}} = -\nabla \overline{p} + \nu \Delta \overline{\mathbf{u}} - \nabla \cdot \mathbf{R} \tag{6.2}$$

imposing consistent initial conditions (IC) and boundary conditions (BC) and where $\mathbf{R}_{ij} = \overline{u'_i u'_j}$ represents the Reynolds stress tensor. Due to the incompressible flow condition, p represents the static pressure divided by the constant density. As shown by Imagawa, Hayase (2010), the assimilation of the data through a state observer algorithm is achieved by introducing a body force term $\mathbf{f}$ into the momentum equation:

$$(\overline{\mathbf{u}}\cdot\nabla)\overline{\mathbf{u}} = -\nabla\overline{p} + \nu\Delta\overline{\mathbf{u}} - \nabla\cdot\mathbf{R} + \mathbf{f} \tag{6.3}$$

Under the hypothesis of steady flow conditions, in the following discussion the overbar indicating the time-average operation has been omitted, although all the quantities are meant to be time-averaged. The relative strength of the body force term represents the feedback and it is proportional to the local difference **e** between the simulation and the experimental time-averaged velocities:

$$\mathbf{e} = (\mathbf{u}^*_{\mathrm{ref}} - \mathbf{u}) \tag{6.4}$$

where $\mathbf{u}^*_{\mathrm{ref}} = \mathscr{P}(\mathbf{u}_{\mathrm{ref}})$, with $\mathscr{P}$ being the operator that projects velocity information from the experimental grid to the computational grid. Further information on $\mathscr{P}$ is given in section 6.4.1. In this work, two different forms of the feedback term have been considered: data assimilation based on state observer with proportional feedback (DASOP) and on proportional-integral feedback (DASOPI). The feedback control law used in the DASOP method reads as:

$$\mathbf{f}_{DASOP} = \frac{K_p}{D}\mathbf{e}\circ|\mathbf{e}| \tag{6.5}$$

where K_p is the proportional feedback gain, the symbol $\circ$ represents the Hadamard product (Styan, 1973) and $|\mathbf{e}|$ is the component-wise absolute value of the error $|\mathbf{e}| = [|e_x|, |e_y|, |e_z|]^T$. The forcing term for the DASOPI method reads as:

$$\mathbf{f}_{DASOPI} = \frac{K_p}{D}\mathbf{e}\circ|\mathbf{e}| + \frac{K_i}{D}\sum_{n=1}^{N-1}\mathbf{e}_n\circ|\mathbf{e}_n| \tag{6.6}$$

where N is the current iteration and K_i is the integral feedback gain and $\mathbf{e}_n$ is the local error vector at the iteration n. While state observers are typically applied to unsteady systems and act in the time domain, in the methodology here proposed the state observer acts in the iteration domain, for the determination of a steady-state solution. The gains K_p and K_i are scalars as they are assumed equal for each component of the error and constant along the simulation and spatially in the entire simulation domain. The values corresponding to cells where $\mathbf{u}^*_{\mathrm{ref}}$

is not available are set to 0, thus disabling the forcing term. The quadratic term implemented in both the proposed feedback terms resembles an error-squared controller, as proposed in Shinskey (1996). Its advantage is that the forcing term is strengthened with respect to a linear controller when the error is large, penalizing the regions where the difference between the reference and the simulated velocity is lower. The result obtained at the end of the simulation represents the assimilated solution. The presented methodology implies the usage of a single simulation to reach the final assimilated solution, contrary to ensemble Kalman filters and variational methods, which require multiple simulations to reach the final assimilated solution.

6.3. SETUP OF THE REFERENCE DATASET EXPERIMENT

6.3.1. WIND TUNNEL AND MODEL

Experiments are performed at the TU Delft Aerodynamics Laboratories in an open-jet open-circuit low-speed wind tunnel (W-tunnel). The tunnel features a 4:1 area contraction, after which the air flow reaches the free-stream velocity $U_\infty = 12$ m/s in a cross-section of 60×60 cm^2. A flat plate 1.5 m long is installed at 10 cm height above the bottom edge of the exit (Fig. 6.1). The plate has a sharp leading edge and is equipped with a zig-zag tripping device at 5 cm past the leading edge that forces the boundary layer to the turbulent regime. The model is a half cylinder of diameter $D = 10$ cm topped by a quarter sphere (figure 6.1) with a total height of 15 cm, as that used in the investigations of De Villiers (2006). The Reynolds number based on the model diameter is $\mathrm{Re}_D = 8 \times 10^4$. This geometry represents a benchmark for automotive aerodynamics for the study of the flow around appendices and in particular the side mirror. It reproduces the essential features of juncture flow and bluff body aerodynamics, including horseshoe vortex, sharp separation at the back, and large-scale fluctuations of the wake and of the reattachment location (De Villiers, 2006).

6.3.2. ROBOTIC VOLUMETRIC PIV

The three-dimensional velocity field is measured by Robotic Volumetric PIV (Jux et al., 2018), the system described in chapter 1. An illustration of the system con-

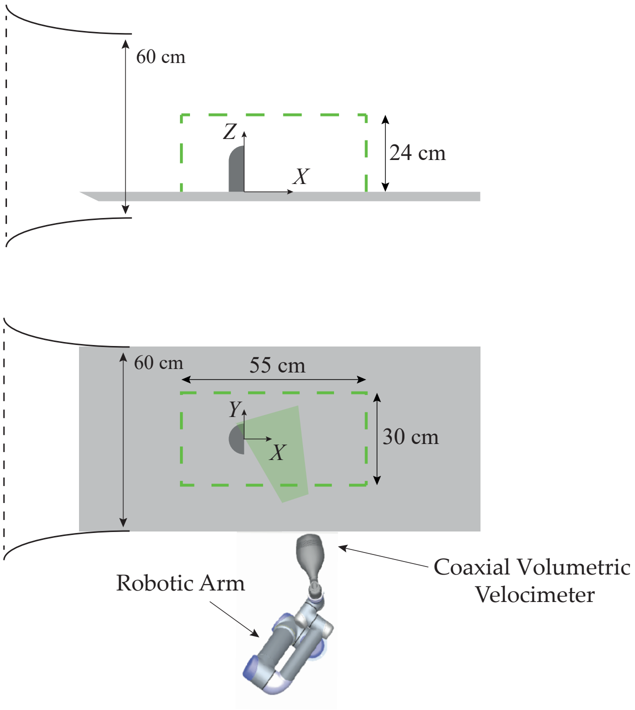

Figure 6.1: Side view (top) and top view (bottom) of the experimental setup. The dashed green line schematically represents the total measurement volume. The shadowed green region indicates the instantaneous measurement volume for a given robot position.

figuration during the experiments is shown in figure 6.1. The system is composed of a coaxial volumetric velocimeter (CVV), containing 4 high-speed cameras, and laser illumination through optic fiber. The CVV is installed on a robotic arm, UR5 from Universal Robots. The robot motion sequence is programmed through the proprietary software RoboDK and operated through the LaVision software DaVis 10. Synchronization of illumination and image acquisition is made through a programmable timing unit (LaVision PTU 9). Helium-Filled-Soap-Bubbles (HFSB) are used as flow tracers (Bosbach et al., 2009; Scarano et al., 2015a; among others). The bubbles are nearly neutrally buoyant with a median diameter of approximately 0.3 mm (Faleiros et al., 2019). A rake composed of 10 vertical elements hosting 200 bubble generators (Caridi, 2018) is installed in the settling chamber of the wind tunnel. Soap, air and helium supply is con-

Table 6.1: Characteristics of the Robotic Volumetric system and the experimental parameters.

Seeding	Neutrally buoyant HFSB, ~ 300µm diameter
Illumination	Quantronix Darwin-Duo Nd:YLF laser (2 × 25 mJ @ 1 kHz)
Recording device	*LaVision MiniShaker* Aero system 4× CCD cameras (640 × 452 @ 857 Hz) 4.8µm pitch
Imaging	$f = 4$ mm, $f_p = 8$
Acquisition frequency	$f_{TR} = 857$ Hz
Pulse separation time	Time-resolved: $\Delta t = 1/f_{TR} = 1.17$ ms
Magnification factor	$M \sim 0.01$ at 30 cm distance
Number of recordings per region	$N = 20000$

trolled through a LaVision fluid supply unit (FSU). The flow is seeded at a concentration of approximately 0.3 bubbles/cm^3. Table 6.1 summarises the experimental parameters. The reader is referred to the works of Jux et al. (2018), Jux et al. (2020) and Schneiders et al. (2018) for a deeper discussion of the working principles of this measurement technique. Here the experimental procedure is discussed. Prior to the measurements, a calibration of the robot position w.r.t. the measurement domain (wind tunnel, plate and object) is performed. Each measurement volume spans approximately 30 × 20 × 40 cm^3. At each robot position, 20000 recordings are acquired in time-resolved mode at a frequency of 857 Hz ($T_{\text{rec}} \sim 23$s). The time elapsed from one position to the subsequent is approximately 270 s. The overall measurement encompasses 15 views, where the measurement system is directed by robotic arm manipulation. At the end of the measurements, the raw data features coverage of the measurement domain with the datasets obtained from each viewing position. The procedure for data processing and reduction is discussed in the next section.

6.3.3. DATA PROCESSING AND REDUCTION

The raw images are pre-processed to reduce background reflections using the Butterworth high-pass filter (Sciacchitano, Scarano, 2014). The tracer motion analysis is performed with the Lagrangian particle tracking algorithm Shake-The-Box (Schanz et al., 2016). Tracks containing more than six appearances of the particle tracer are deemed as valid. At each recording, a sparse measurement of the tracers' velocity is obtained in the sub-volume. The measurements from different robot positions are merged into a single dataset using the robot calibration data. The resulting domain is interrogated within cubic voxels (or bins) of 15 mm side length. Within each bin, the tracers' velocity is ensemble-averaged, yielding the time averaged velocity vector distribution in a Cartesian grid. The averaging process inside the bin follows a spatially weighted algorithm with respect to the centroid of the bin. A Gaussian weighting function (with a width of half the bin size) is applied, following Agüera et al. (2016). Partial overlap by 3:4 of neighbouring voxels yields velocity vectors spaced by 3.75 mm. The result is rendered in a domain of $55 \times 30 \times 25$ cm^3 (figure 6.1) with a grid of $151 \times 84 \times 69$ data points describing the time-average velocity $\mathbf{u}_{\mathrm{ref}}$ for use in the data assimilation procedure.

6.4. NUMERICAL SIMULATIONS

Both *baseline* and *assimilated simulations* are based on a RANS solver using the open-source C++ toolbox *OpenFoam 1706* (Jasak, 2009). Equations 6.1 and 6.2 are discretised using the finite volume method on a collocated grid and solved using the SIMPLE algorithm (Patankar, Spalding, 1972). For the baseline simulation, the steady solver *simpleFoam* implemented in OpenFoam is used. For the assimilated simulations, the feedback term is included within an in-house developed version of the same solver. Turbulence modelling is based on the $k-\omega$ SST model (Menter, 1993). The computational domain is a square cuboid with dimensions $30 \times 20 \times 10$ diameters. The object is placed along the centreline of the domain, with the origin of the coordinate system posed at the intersection between the rear surface of the car mirror and the ground. The orientation of the coordinate system is shown in figure 6.1. An inlet condition is imposed at $X/D = -10$ and an outlet condition is imposed at $X/D = 20$. No-slip condition is imposed at the ground floor and the object surfaces, whereas slip conditions are applied to the top and side faces of the domain. A summary of the boundary and initial condition is reported in Table 2. The same hexahedral mesh is used for both the baseline and the assimilated simulations, formed by ~ 18.5 M cells and created with the commercial software *CFMesh* +. The region close to the surface of the object ($-7 < X/D < 15$ and $-7 < Y/D < 7$) is refined at several stages, as shown in figure 6.2, where the cell dimension reduces from 10 mm to 0.78 mm, corresponding to $y^+ < 5$. All the simulations advance for 5000 iterations and convergence is verified by reaching a relative variation of the averaged drag coefficient of the object $|\overline{C}_{d,n} - \overline{C}_{d,n-1}|$ below 10^{-3}, where the average is performed in the interval $[n-500\ldots n]$. The same interval is used to average the velocity field to take out numerical oscillations.

Table 6.2: Boundary and initial conditions of the simulations for velocity and pressure.

	Velocity	Pressure
Inlet	Dirichlet, $u = (12,0,0)$	Neumann, $\partial p \partial x = 0$
Outlet	Neumann, no backflow $\partial u/\partial x = 0$	Dirichlet, $p = 0$ Pa
Object surface	no-slip condition	
Bottom wall	no-slip condition	
Lateral walls	slip condition	
Top of the domain	slip condition	
Initial condition	u = (12,0,0) m/s	$p = 0$ Pa

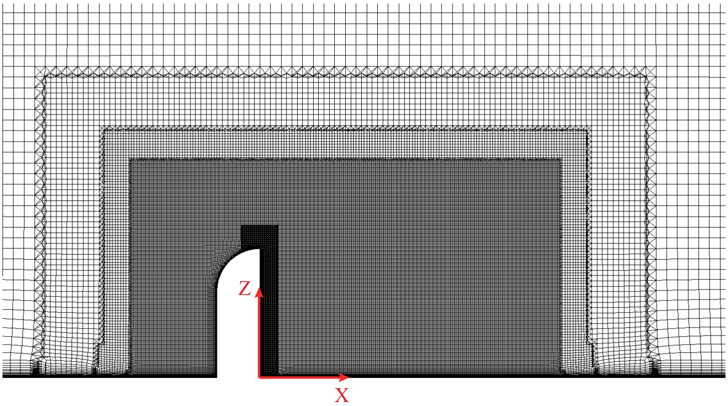

Figure 6.2: Computational mesh around the object along the symmetry plane of the simulation domain.

6.4.1. ASSIMILATION PROCEDURE

After conducting the baseline simulation, several assimilated simulations are run to investigate the effects of assimilation. The analysis presented here aims at de-

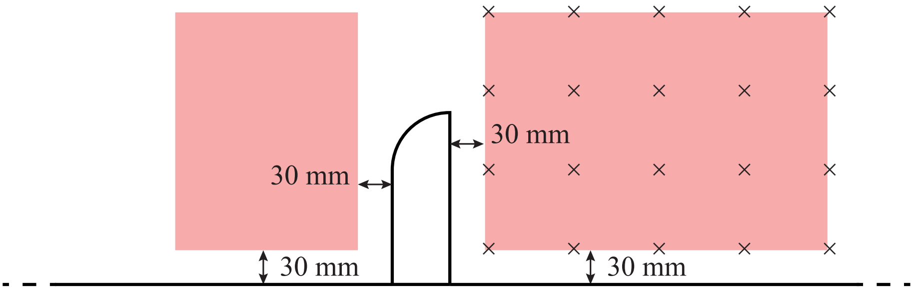

Figure 6.3: Section at $Y = 0$ of the forced region. Crosses represent the points forced to evaluate the response function presented in section 6.5.3.

termining the effect of sparse forcing varying the concentration of forced cells. The latter is represented in terms of the normalised mean distance between neighbouring forcing cells $\gamma = \lambda / D$, where λ is the mean distance between neighbouring forcing points. In order to evaluate λ, the following equation is used:

$$\lambda = \sqrt[3]{\frac{4}{3\pi C}} \tag{6.7}$$

where $C = N_f / V$, with N_f equal to the number of forced cells, selected randomly, and V the total forced volume. The small positional mismatch between cells where forcing is applied and the locations where experimental data is available is accommodated by linear interpolation to the closest experimental data points, obtaining the velocity field $\mathbf{u}^*_{\text{ref}}$. This operation is then fully justified in cases in which the expected interpolation error are negligible, as in the case considered in this work. Furthermore, in order to damage the assimilated solution, outliers have to be removed from $\mathbf{u}^*_{\text{ref}}$ before the interpolation step. In the other cells, both the values of $\mathbf{u}^*_{\text{ref}}$ and e are set to zero. At each iteration of the assimilated simulation, the velocity field $\mathbf{u}^*_{\text{ref}}$ is compared with the velocity field $\mathbf{u}^{n-1}$ of the previous iteration and the error field e is explicitly constructed according to equations 6.5 and 6.6, respectively for the DASOP and DASOPI feedback law. The limited spatial resolution of the ensemble-averaged PIV velocity data close to the wall leads to prescribed reference velocity $\mathbf{u}^*_{\text{ref}}$ too high and not compatible with the no-slip condition assigned to the walls of the simulation. For this reason, PIV data closer than 3 cm (two averaging sub-volumes in the PIV analysis) have not been considered to build the forcing term **f**. In relation to this, figure 6.3 shows a section along the symmetry plane of the regions where the forcing term was activated, with different forcing cell density, depending on the choice of γ.

6.5. RESULTS AND DISCUSSION

6.5.1. REFERENCE FLOW FIELD

The measured velocity field $\mathbf{u}_{\text{ref}}$ is visualized in figure 6.4, where the streamwise velocity component $\mathbf{u}_{\text{ref}}$ is shown at the symmetry plane and in a wall-parallel plane at a height $Z/D = 0.5$. The potential flow region in front of the object is visible, where the flow decelerates and eventually stagnates at the obstacle due to the adverse pressure gradient (figure 6.4, bottom). The boundary layer that has developed along the plate is also visible in section $Y = 0$ (figure 6.4, top). Acceleration atop the obstacle is consistent with the streamlines curvature that follows the object head (figure 6.4, top). The local velocity in this region exceeds the free-stream value by approximately 20%. The boundary layer developing along the object surface separates abruptly due to the sharp truncation of the object at the trailing edge. Within the separated zone, a reverse flow region is formed. This feature has been observed past a number of wall-mounted obstacles and reported frequently in the literature (Martinuzzi, Tropea, 1993; De Villiers, 2006; Yakhot et al., 2006; among others).

The separated region terminates downstream with a ground-reattachment line with its most downstream position at X_R in the symmetry plane. In the present experiment, the length of separation is observed to be $X_R/D = 2.4$. At the edge of the shear layer and the backflow region, from figure 6.4 (bottom) is also possible to visualize two counter-rotating vortices from the streamlines pattern. The correspondent foci are labelled F_2 and F_3 in figure 6.4 and in the rest of this work. As reported by De Villiers (2006), these are part of a U-shaped structure that appears in the time-averaged velocity field, positioned upside-down w.r.t. the object and tilted towards the back surface of the mirror. The point in which this structure crosses the symmetry plane is detectable in figure 6.4 (top)

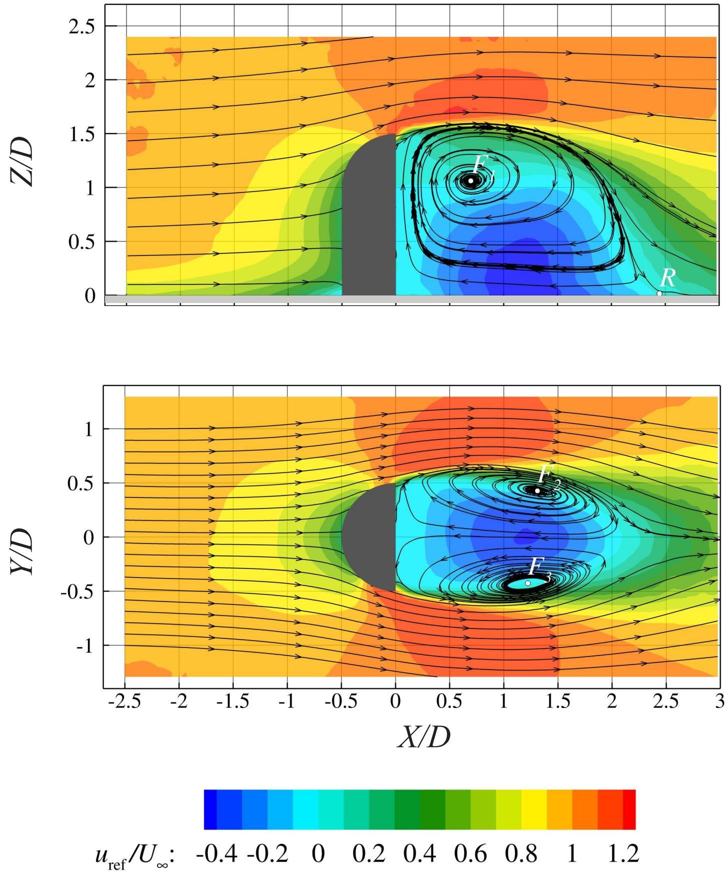

Figure 6.4: Visualization of the normalized time-averaged streamwise velocity u_{ref}/U_∞ with superimposed streamlines, measured by Robotic Volumetric PIV: (top) at the symmetry plane and (bottom) at $Z/D = 0.5$.

by the foci named F_1. The analysis of the vorticity field, illustrated in figure 6.5, provides further insights into the reference flow topology. The adverse pressure gradient at the front of the object causes the boundary layer to detach from the ground and form the horseshoe vortex (Simpson, 2001), which develops around the object, eventually aligning streamwise and further developing downstream of the object wake. The development from the front of the object of the horseshoe vortex is shown in figure 6.5 by the two portions of the iso-surface where the

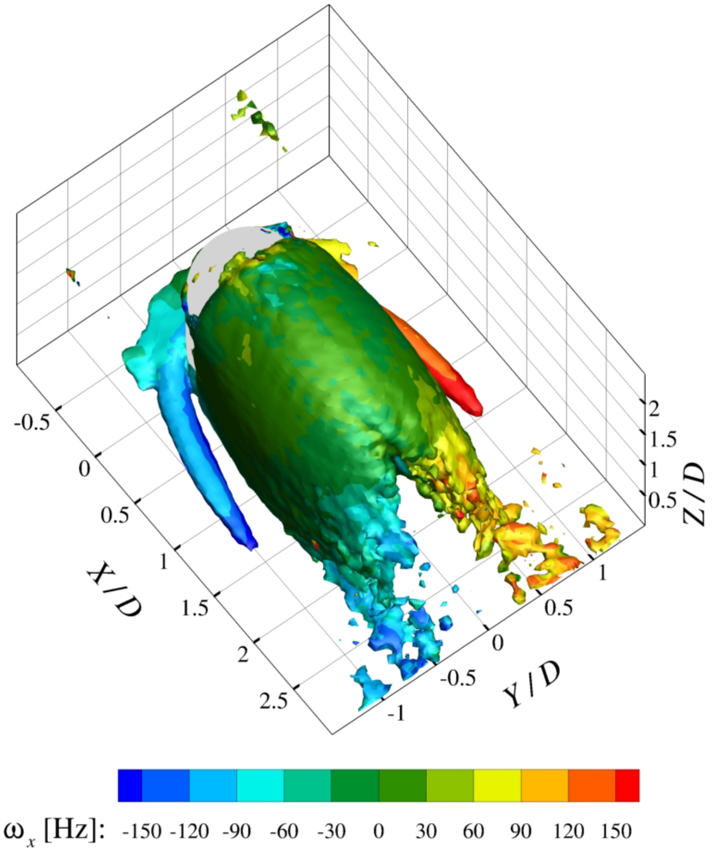

Figure 6.5: Iso-surface of vorticity magnitude $|\omega| = 200$ Hz, coloured by streamwise vorticity ω_x.

magnitude of the streamwise vorticity $|\omega_x| > 200$ Hz. As described by De Villiers (2006), the time-averaged separation region is bounded by an arc-like free shear layer, which develops downstream and bounds a region of flow recirculation that also features an arc-like shape.

6.5.2. BASELINE SOLUTION

The flow field topology returned by the baseline simulation, as shown in figure 6.6 (left), largely follows the flow pattern observed in the experiments. The boundary layer development under the adverse pressure gradient caused by the obstacle is visible, with the formation of a small recirculation ahead of the object

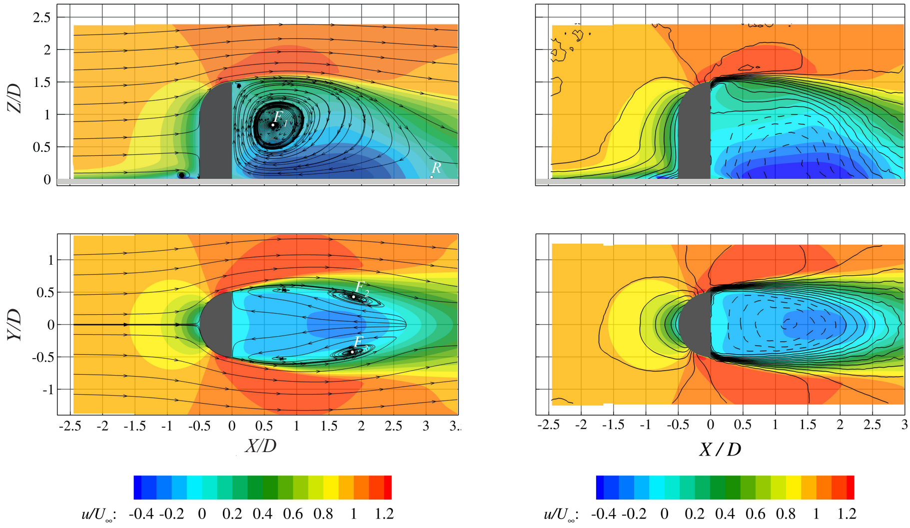

Figure 6.6: (Left) Streamwise velocity contour obtained by the baseline simulation with overlapping streamlines: (top) at the symmetry plane and (bottom) at $Z/D = 0.5$. (Right) Colour contours of streamwise velocity from the baseline solution and over-lapping iso-lines of the reference velocity field (dashed contour lines for negative values). (top) Symmetry plane and (bottom) at $Z/D = 0.5$.

(head of the horse-shoe vortex) at approximately $X/D = -0.8$. The overall flow deceleration ahead of the object and subsequent acceleration towards the trailing edge are also visible by regions at a velocity exceeding the free-stream value. In the region upstream of the object, the result obtained by the baseline simulation complies rather well with the reference, as visible in figure 6.6 (right). This is expected since RANS are able to predict accurately flow features in potential flow regions. A notable exception is instead the region close to the ground, where the simulation is not forced. The topological differences are discussed in the remainder. The flow separation at the sharp trailing edge is also well reproduced. Whereas the most significant discrepancy with respect to the reference velocity field is produced in the separated flow region and the reattachment region in particular. The RANS data predict a longer wake, as clearly visible in figure 6.6 (right), with a reattachment occurring at $X_R/D = 3.1$, along the symmetry plane. This behaviour has already been reported in previous works (Lübcke et al., 2001; among others), where RANS simulations tend to overestimate the length of the wake of a bluff body. Together with the elongation of the wake behind the object, other topological features in the wake are distorted. As visible in figure 6.7, combining the information obtained by the two sections, it is possible to infer the presence of the arc-shaped vortex. The latter has, however, a pronounced offset (judged from the location of the two foci at $Z/D = 0.5$) from $X/D = 1.25$ of the reference data to $X/D = 1.85$. In the symmetry plane instead, the focus F_1 is located closer to the ground ($Z/D = 0.8$ in the simulation, compared to $Z/D = 1.05$ of the reference data). The resulting arc-vortex in the baseline simulation is more elongated in the streamwise direction and with a lower position of its top portion. The latter is also visible considering the region of reverse flow (in figure 6.6-right by the dashed line of the reference data is superimposed to the baseline simulation) appearing flattened towards the ground. Further small differences are the upstream separation forming the head of the horseshoe vortex, a small recirculation region at the free end of the object and a small region of accelerated flow close to the object trailing edge (figure 6.6-left). These features are, however, not captured within the experiments due to the limited spatial resolution of the measurements. An L-2 metric is introduced to quantify the discrepancy between the *baseline simulation* and the reference data. The following relative error normalised with the free stream velocity U_∞ has been used:

$$\varepsilon = \frac{\sqrt{(u-u_{\text{ref}})^2+(v-v_{\text{ref}})^2+(w-w_{\text{ref}})^2}}{U_\infty} \tag{6.8}$$

The reference data is available on a grid that does not coincide with that of the numerical simulations. The value of ε is therefore obtained by linear interpolation of the numerical simulations onto the grid of the reference data. The spatial distribution of ε at the symmetry plane is shown in figure 6.7. The relative error distribution can be clustered in four different regions. The widest region of error can be found for $X/D > 2$ around the centerline, where $\varepsilon > 0.3$ is reached. The source of this error lies in the length of the wake, having the reference flow already recovered momentum at that stage compared to the simulation. Another region of high relative error is centred at $X/D = 1.25$ and $Z/D = 0.55$. This is related to the height of the backflow region. Since the simulation predicts a backflow region shorter in height with respect to the reference, this causes a deficit of momentum and an increase of ε in that flow region. Furthermore, ε peaks in close proximity to the object. This is due to the lack of resolution for the experimental data previously mentioned. Because the discrepancies in the latter region cannot be ascribed to the numerical simulations, an integral evaluation of the relative error will exclude the regions close to the object surface and the ground wall.

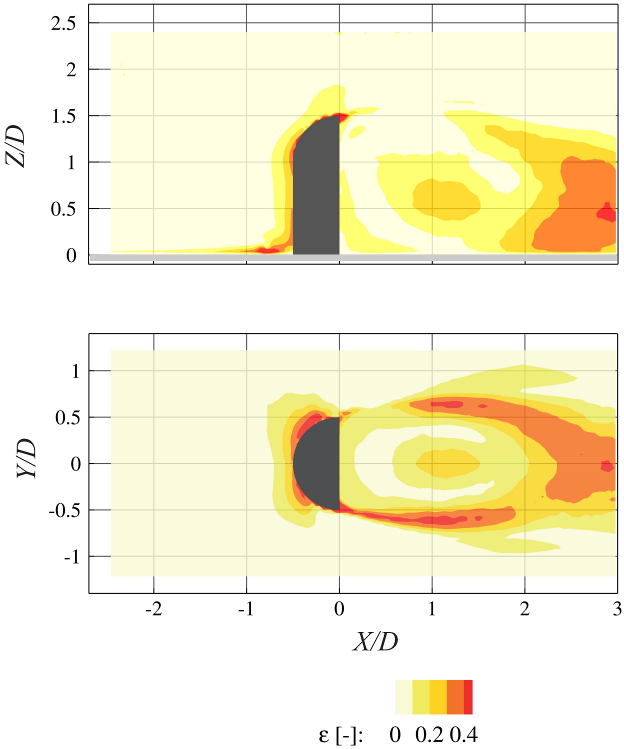

Figure 6.7: Relative error ε of the baseline simulation: (top) at the symmetry plane and (bottom) at $Z/D = 0.5$.

6.5.3. ASSIMILATED SIMULATIONS

Before presenting the results of the assimilated simulations, the local response to the forcing function at individual points is discussed. The effect of the forcing is expressed through the response function $H = |(\mathbf{u}_{\text{bas}} - \mathbf{u})/(|\mathbf{u}_{\text{bas}} - \mathbf{u}^*_{\text{ref}}|)|$, where $\mathbf{u}_{\text{bas}}$ represents the baseline solution and u the assimilated solution. The analysis

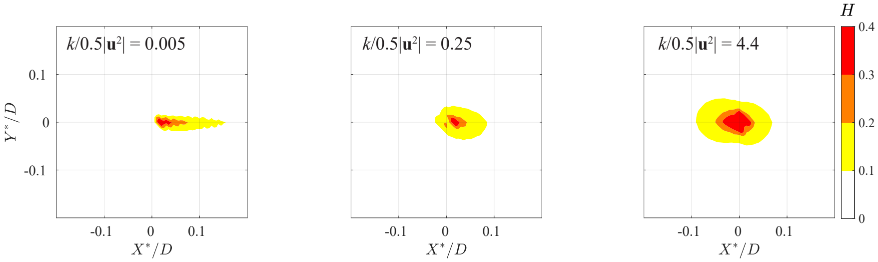

Figure 6.8: Region of influence of DASOPI for points in the external flow (left); inside the shear layer (middle) and in the separated region (right). Coarse distribution of forcing points $\gamma = 0.5$ (distance of 5 cm).

is performed on cells widely separated spatially ($\gamma = \lambda/D = 0.5$ or 5 cm distance between forced cells), as illustrated in figure 6.3. This is done to consider the result that only depends on the local forcing, with no interference among neighbouring forced points. For each forced cell with center $\mathbf{X}_c = (X_c, Y_c, Z_c)$, a $5\times5\times5$ cm^3 cube is considered, with its center on X_c, and discretized with $101\times101\times101$ elements. For each cube, the effect of the forcing is averaged over a local coordinate system $\mathbf{X}^* = (X - X_c, Y - Y_c, Z - Z_c)$ permitting the alignment of results among different points.

The parameter H is evaluated around X_c. Because the forcing term is introduced in the momentum equation, the extent and shape of the region affected by the forcing are expected to follow local diffusion and convection. To assess the region of influence of the forcing, three flow regimes are considered, namely: a) the outer (potential) flow at approximately free-stream velocity; b) the shear layer emanating from the object trailing edge; c) the recirculating flow inside the separated region. Figure 6.8 shows the spatial distribution of H for the three considered regions obtained by applying DASOPI. The local effect of the forcing algorithm extends to a region with a length not exceeding 2 cm ($0.2D$). Such localised effect of the forcing has been also observed in previous works, namely, in the study by Imagawa, Hayase (2010). This result suggests in advance that data assimilation at values of $\gamma > 0.2$ may result in localised rather than global modifications of the simulation result. The extent and shape of the region neighbouring the forced location appear to be affected by the local flow properties. In the outer flow region, the effect of the forcing is comparatively weak and highly elongated along the convection direction. In the regions of lower local velocity and high turbulent diffusion, such as the shear and the recirculation regions, the spatial response function is close to isotropic. In figure 6.9, also the local value of the turbulent kinetic energy k normalised by the local kinetic energy is presented. The extent and shape of H follow that of k. A similar analysis performed with the DASOP method yields no visible change in velocity, with values of H typically below 0.1%. In the remainder of this work, the location of the forcing points is chosen randomly with a distribution controlled through the density parameter $\gamma = [0.01 \ldots 0.45]$; the corresponding mean distance λ between forcing points varies between 4.5 cm ($0.45D$) and 1 mm ($0.01D$). Before comparing the results obtained by the two proposed algorithms, the effect of the two parameters K_p and K_i is investigated. The study has been performed using the DASOPI algorithm for the case of $\gamma = 0.03$. In order to evaluate the effectiveness of the chosen values of K_p and K_i, the error ε has been averaged in the volume where experimental data were available; the symbol $\overline{\varepsilon}$ indicates the result of this operation. Since the results have been found to be mostly insensitive to the value of K_p, figure 6.9 shows the obtained $\overline{\varepsilon}$ varying K_i and averaging the results obtained for $0.001 < K_p < 10$. The bars at each data point represent the variation obtained varying K_p for a given K_i. The results show a decay of $\overline{\varepsilon}$ when K_i is increased.

This is expectable, since when K_i is increased, the integral part of the forcing term becomes stronger, with a subsequence stronger correction towards the bias errors of the simulation. When $K_i = 1$, while the simulation results exhibit a lower error with respect to the reference, artificial edge effects start to appear at the boundary of the forced region. For values of $K_i > 1$, the simulations show numerical instability and diverge. For this reason, it has been decided to set the parameters as $K_p = 1$ and $K_i = 0.1$ for all the simulations presented in the remaining part of the manuscript. Figure 6.10 shows the results obtained by both the forcing methods DASOP and DASOPI when $\gamma = 0.03$. As for the baseline simulation, in the potential flow region, both DASOP and DASOPI assimilated results agree well with the reference measurement. Larger differences between the two forcing methods are found in the wake region. The application of the proportional forcing term (DASOP) does lead to a reduction in the length of the recirculation region, and the furthest point of the reattachment line is moved to $X/D = 2.9$,

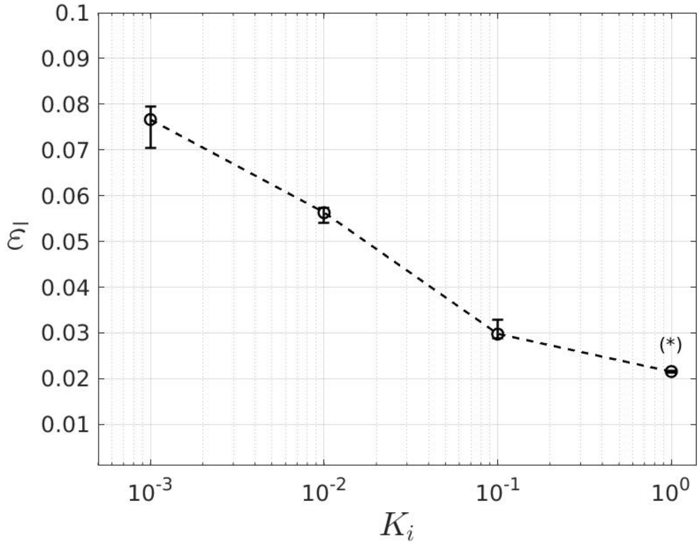

Figure 6.9: Spatial-averaged relative error ($\overline{\varepsilon}$) with respect to the integral and proportional gain (K_p and K_i). Variability of the results as a function of the variation of K_p ($K_p = [0.001, 0.01, 0.1, 1, 10]$) is expressed by the vertical bars (upper bound: maximum error; lower bound: minimum error). Simulations performed with $\gamma = 0.03$. (*) Artifacts appear at the edge of the forced domain.

closer to the reference than that of the baseline simulation. The height of the backflow region, however, remains lower compared to the reference as it can be seen in the section at $Z/D = 0.5$ in figure 6.10; furthermore, the backflow is underestimated by more than 50%. The use of the DASOPI algorithm visibly improves the fidelity of the velocity field obtained by assimilation. The reattachment point upstream to $X/D = 2.4$, practically matching the reference data. The DASOPI result also recovers the topology of the recirculation region given in the reference data for what concerns the position of the foci figure 6.10).

The effect of further refining the density of forcing points (the distance between forcing points is reduced to $0.01D$) is illustrated in figure 6.12. In this case, all grid cells in the selected volume are forced. The DASOP algorithm with a greater number of forced points yields some improvement in terms of similarity to the reference data. While in the potential flow region, no dramatic changes are visible, the length of the wake is shortened, with the reattachment point found

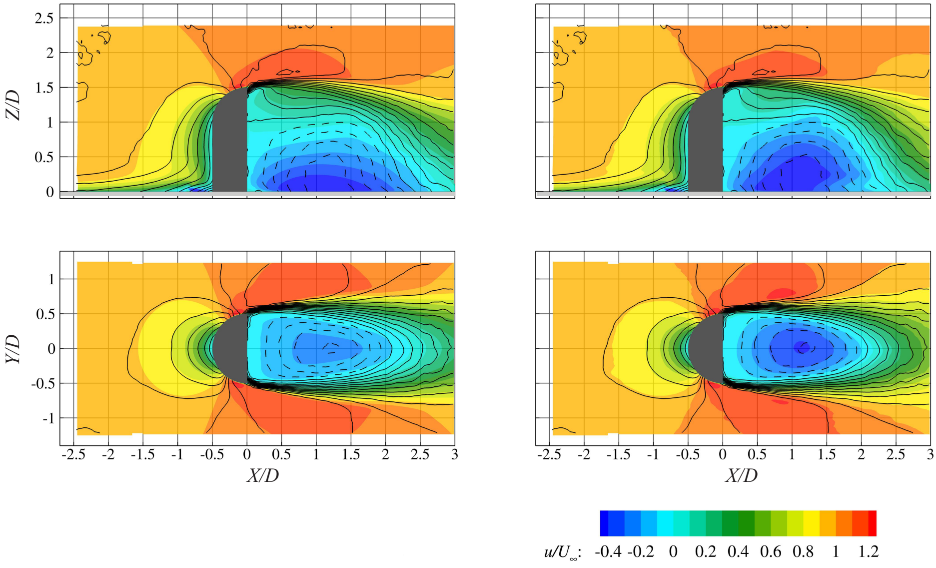

Figure 6.10: Streamwise velocity contours of DASOP (left) and DASOPI (right) *assimilated simulation*. Contours of reference data are superimposed (dashed lines for negative values). $Y/D = 0$ in the top row; $Z/D = 0.5$ in the bottom row. Forcing density by $\gamma = 0.03$.

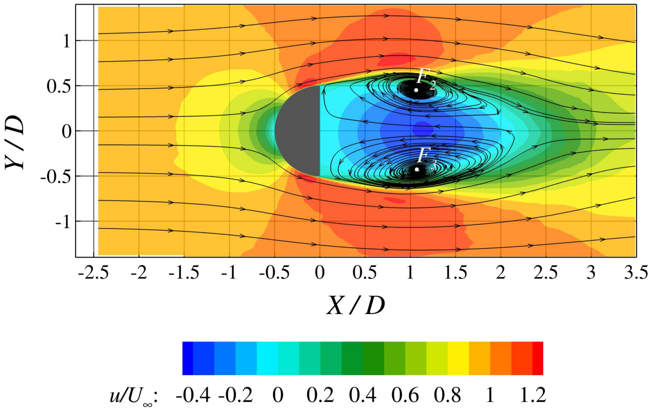

Figure 6.11: Streamwise velocity contour obtained by the assimilated simulation by DASOPI algorithm and $\gamma = 0.03$ with super-imposed streamlines at $Z/D = 0.5$.

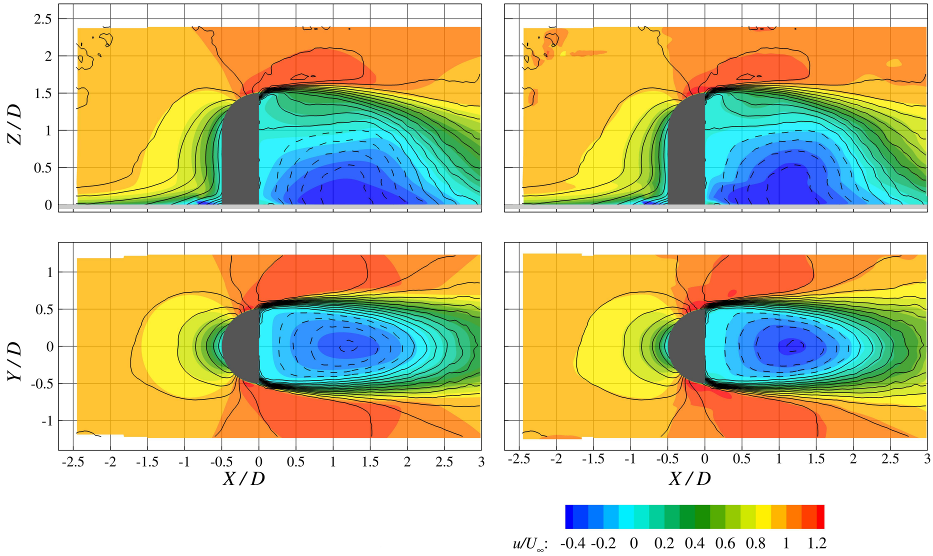

Figure 6.12: Streamwise velocity contours of DASOP (left) and DASOPI (right) in the assimilated simulation. Contours of reference data are superimposed (dashed lines for negative values). $Y/D = 0$ in the top row; $Z/D = 0.5$ in the bottom row. Forcing density $\gamma = 0.01$.

at $X/D = 2.28$ at the symmetry plane. The shortening of the wake is also coupled with an increase of the backflow with respect to the simulation obtained by DASOP with $\gamma = 0.03$. However, at the plane $Z/D = 0.5$, the backflow magnitude peak is still underestimated with respect to the reference. For what concerns the comparison between DASOP and DASOPI, figure 6.12 confirms the trend observed with $\gamma = 0.03$, with DASOPI overperforming. In the region where the forcing is applied, the contour lines of the assimilated solution with DASOPI overlap with the ones representing the reference. It is noticed, however, that the simulation attempts to converge everywhere to the reference data, even where the latter is affected by outliers. This behaviour can be noticed in the top-left corner of the symmetry plane of figure 6.12.

Furthermore, when this density of the forcing point is used, the extension of the volume where the forcing is activated becomes directly visible in the velocity field, with artefacts at its edges. The global behaviour of the error relative to the reference data is quantified for both algorithms with its spatial average ε defined in equation 6.8. The variation of $\overline{\varepsilon}$ as a function of the forcing density γ is represented in figure 6.13. In order to capture the most relevant source of error shown in figure 6.7, the average has been obtained taking into consideration only the volume downstream of the body shown in figure 6.3. The result given by the baseline has been plotted with a dotted line as a reference. The assimilated simulations appear to be too coarsely forced as long as $\gamma \geq 0.1$. Under this condition, both DASOP and DASOPI methods produce an error comparable to the *baseline solution*. The distance between the forcing points is too high to have a global reduction of the error compared to the baseline and the effect of the forcing remains local. When $\gamma < 0.1$, the behaviour of the two methods differs. DASOP method is not able to reduce the error until $\gamma < 0.05$. If γ is further reduced, the error reduces, reaching $\overline{\varepsilon} = 0.06$ when $\gamma = 0.01$. Compared to the baseline error, an error reduction of 28% is obtained. The DASOPI algorithm becomes effective for $\gamma < 0.1$. As also shown in figures 6.10 and 6.12, DASOPI is more effective

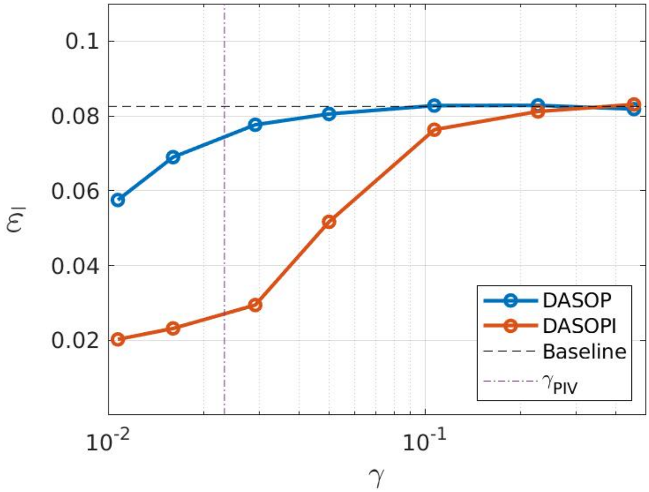

Figure 6.13: Spatial-averaged relative error $\overline{\varepsilon}$ as a function of the relative mean forced point distance γ. The horizontal dashed line represents the relative error of the baseline simulation. The vertical dashed-dotted line represents the vector spacing of the PIV measurements ($\gamma_{PIV} = 0.023$).

than DASOP, yielding lower error values in a wider range of values for γ. When $\gamma = 0.05$, the relative mean error becomes $\overline{\varepsilon} = 0.055$.

Further reducing γ to 0.01, yields $\overline{\varepsilon} = 0.023$, corresponding to a reduction of 72% compared to the baseline. The reduction of $\overline{\varepsilon}$ at decreasing γ can be explained by the response function shown by figure 6.8. When γ decreases, the amount of the flow field that is affected by the assimilation increases. The dimension of the volume affected by the forcing proportional-integral forcing term shown in figure 6.8 explains the behaviour of ϵ for what concerns DASOPI. The majority of the source of ϵ is concentrated in wake of the object. Since the av-

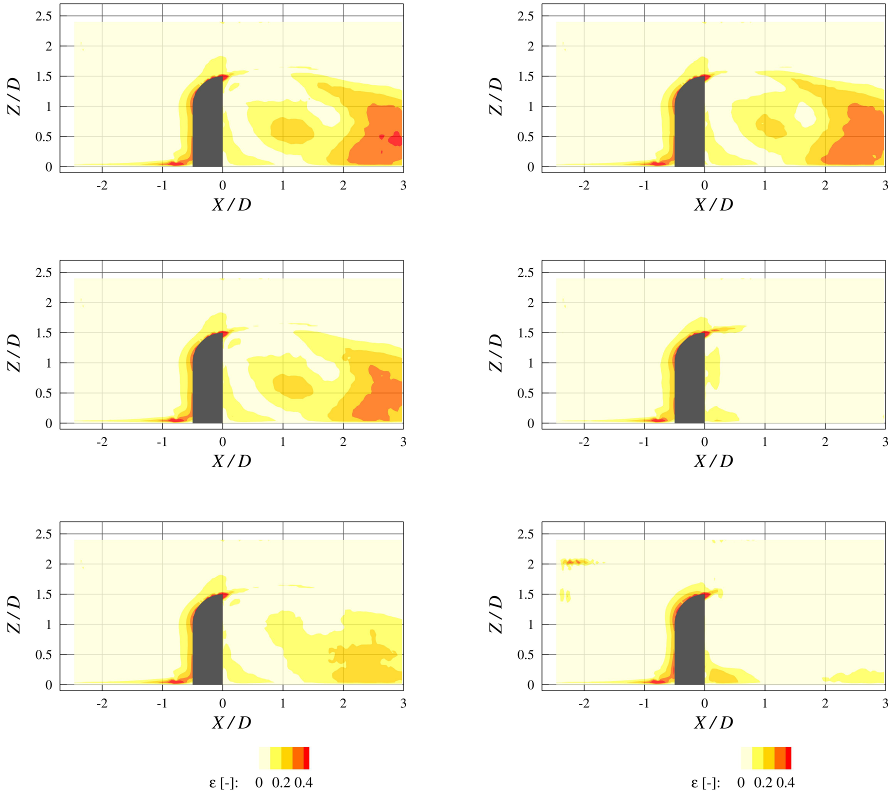

Figure 6.14: Local relative error ε (equation 6.8) at the symmetry plane $Y = 0$ for: (first row) DASOP and DASOPI with $\gamma = 0.1$, left and right respectively (second row) DASOP and DASOPI with $\gamma = 0.03$, left and right respectively (third row) DASOP and DASOPI with $\gamma = 0.01$, left and right respectively.

erage volume of effectiveness can be represented as a sphere with diameter $O(1$ cm), the method starts being effective when such volumes start overlapping, corresponding to the condition $\gamma < 0.1$. Figure 6.14 compares the spatial distribution of the relative error ϵ for the baseline simulation, DASOP and DASOPI, with $\gamma = [0.1, 0.03, 0.01]$. The spatial distribution of ϵ illustrates that the error is confined in specific regions of the flow: in close proximity to the object; around the reattachment region; within the recirculating flow. For $\gamma = 0.1$, the spatial distribution of ϵ presented by the assimilated simulations is close to that given by the baseline, with a small reduction shown by DASOPI in the recirculation region and the far wake. When γ is reduced to 0.03, both DASOP and DASOPI yield a reduction of ϵ compared to the baseline. While DASOP still shows areas characterized by $\epsilon > 0.2$ in the recirculation region and the far wake, DASOPI achieves $\epsilon < 0.05$ everywhere except in proximity of the object and in the shear layer close to separation. Finally, for $\gamma = 0.01$, a further reduction of ϵ is noticed in the entire field. It can be noted that, for what concerns DASOPI, some regions of high error outside the forcing area arise, as introduced in the previous paragraph. The optimisation of the location of the forcing points to minimise the error of the assimilated simulation will be investigated in future works.

Overall considerations on the effect of data assimilation to the flow topology can be done considering the horseshoe and the arc-vortex axis lines, alongside the specific velocity contour $u = 0$ at $Z/D = 0.5$ (figure 6.15). Considering the horseshoe vortex, none of the simulations reproduces the path shown by the reference. With a larger separation distance (Gazi, Afzal, 2020), the horseshoe vortex showed by the simulations presents an offset toward negative X values with respect to the reference. The assimilation, both through DASOP and DASOPI, does not influence the path of the horseshoe vortex before $X/D < 1$. It must be noted that, being the horseshoe vortex close to the ground, it lays outside the region where the forcing is active, as represented by figure 6.3. For $X/D > 1$, the assimilation through DASOPI of the flow above the vortex influences its path, reducing its distance with respect to the reference. The continuous line in figure 6.15 represents the contour line $u = 0$ at $Z/D = 0.5$. At this location, inside the forced region, the assimilations performed both with DASOP and with DASOPI reduce the distance between simulation and reference. As shown by figure 6.13,

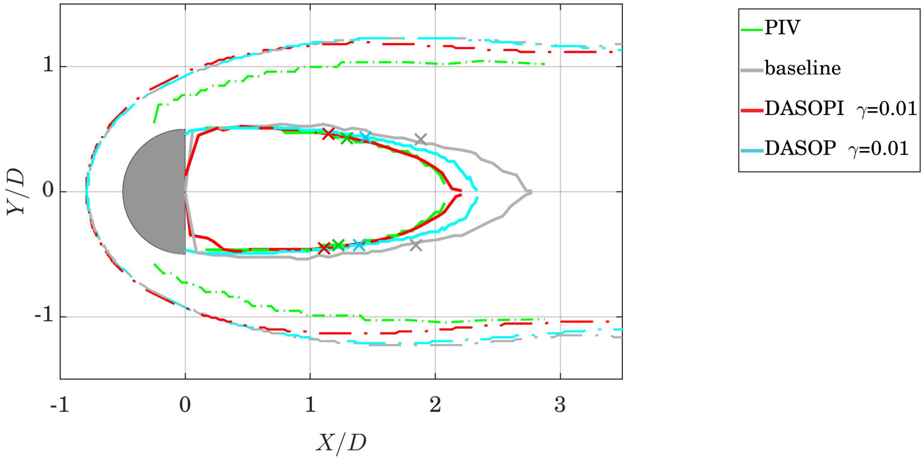

Figure 6.15: Comparison of the topology obtained by PIV (reference), baseline simulation, DASOP with $\gamma = 0.01$ and DASOPI with $\gamma = 0.01$. Dash-dotted lines represent the (X,Y) projection of the trajectory of the horseshoe vortex. Continuous lines represent the contour line $u = 0$ at $Z/D = 0.5$. Crosses represented the position of the foci F_2 and F_3 at $Z/D = 0.5$.

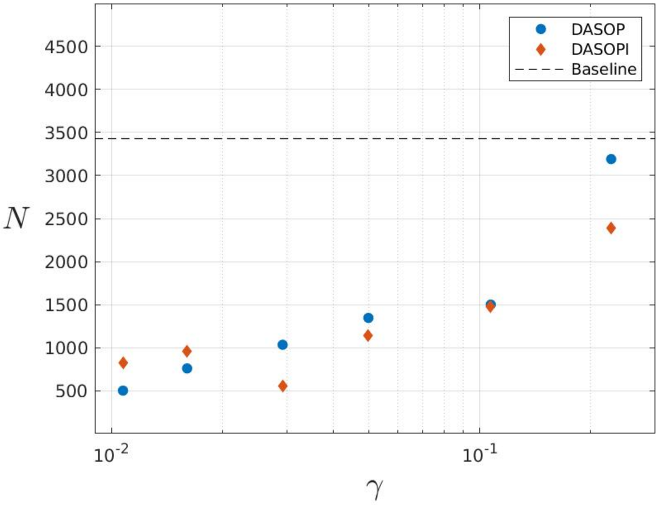

Figure 6.16: Number of iterations required to reach convergence as a function of the forcing spacing γ.

DASOPI overcomes DASOP in reproducing the wake shape of the reference. The shortening of the wake brought by the assimilation causes also a reduction in the distance between the foci F_2 and F_3 between reference and assimilated simulations, foci that are represented by the crosses in figure 6.15. The assimilation has also an effect on the convergence rate of the simulation. A simulation has been considered converged when the moving standard deviation (kernel equal to 500 iterations) of the model drag coefficient C_d falls below a threshold value chosen equal to 10^{-3}. Figure 6.16 shows the number of iterations required to reach convergence with respect to the relative mean forced point distance γ. For both DASOP and DASOPI, the amount of iterations for convergence is lower than in the baseline simulation (dashed line in figure 6.16). Also in this case, decreasing γ has a positive effect, yielding a reduction in the number of iterations required. It must be noted however that for $\gamma < 0.03$, the number of iterations needed by DASOPI does not decrease anymore, which is ascribed to the appearance of the aforementioned edge effects.

6.6. CONCLUSIONS

In this chapter, a data assimilation framework based on a state observer algorithm has been presented. Two forcing terms, proportional (DASOP) and integral-proportional (DASOPI), have been considered. The performances of the proposed algorithms are based on an experimental dataset consisting of the time-average 3D velocity field around a simplified car mirror geometry. The measurements have been conducted with Robotic Volumetric PIV. Both the forcing terms proposed are functions of the difference between the simulated velocity and the reference experimental data. The local response function of the forcing term has been evaluated, confirming the results of Imagawa, Hayase (2010), where the effect is limited to the region close to the forced location and the shape and extent of the affected region depend on the local convection and diffusion. The data assimilation of the entire domain of interest is parametrised with respect to the spatial concentration of forced points or forcing density γ. Both DASOP and DASOPI produce a reduction of the error compared to the baseline simulation. DASOP requires $\gamma < 0.05$ to produce significant effects, while DASOPI yields a comparable error reduction at already $\gamma = 0.1$, as a result of the higher strength, given the integral formulation of the forcing term. For $\gamma < 0.1$, DASOPI reduces progressively the error of the assimilated simulation. The maximum error reduction is obtained at the maximum forcing density ($\gamma = 0.01$), where the error of the assimilated simulation is approximately 25% of the one of the baseline simulation. The topological analysis based on the reattachment point, the arc-vortex and horseshoe vortex axes confirms that the data assimilation by DASOPI produces a realignment of the simulation towards the experimental reference, also in those regions where the forcing is not applied locally. The latter suggests that the convective-diffusive nature of the forcing mechanism may extrapolate the effects of the assimilated region beyond the domain where experimental data is available.

7

CONCLUSIONS AND PERSPECTIVES

In this dissertation three main topics have been addressed: the increase of DVR through multi-step measurements, the outlier detection based on constitutive equations and the data assimilation of PIV data to numerical simulations. In this chapter, the main conclusions for each of these topics are summarized. In addition, possible directions for future research are discussed, based on the current limitation of the proposed approaches.

7.1. MAIN CONCLUSIONS

7.1.1. INCREMENT OF DVR THROUGH MULTI-STEP APPROACHES

The increment of the achievable dynamic velocity range is a classical topic in the PIV community. Modern hardware and the exploitation of the time component have made it possible to reach a high level of DVR. However, when considering high-speed and complex aerodynamic flows, the limitations in DVR become more strict due to the necessity of adopting low-aperture, low-speed acquisition systems, such as coaxial volumetric velocimetry. To overcome these limitations, a new multi-step approach has been proposed. The core of the new method is the idea that to obtain the final time-averaged velocity field, multiple acquisitions can be combined.

Firstly, a combination of two double-frame single-exposure acquisitions has been considered. With a first acquisition characterized by a low pulse separation Δt_0, a robust but not precise predictor field is obtained. Employing the Reynolds decomposition on these velocity data is possible to extract the time-averaged and the fluctuating components. Using this information, the images acquired in a second acquisition with a larger Δt_1 are analyzed. The availability of the predictor field in terms of both average particle displacement and turbulence level allows for an increase in the pulse separation time, with a consequent increase in the DVR.

The methodology has been proven to be effective considering two experimental cases: the flow behind a truncated cylinder, acquired by means of a large tomographic aperture system, and the near-wake of an Ahmed body, in which the robotic volumetric PIV has been used. In both cases, the methodology has allowed an increase of achievable DVR, with major results obtained along the coaxial component in the low aperture case, where the errors are decreased by one order of magnitude.

Finally, through an a-posteriori analysis of the results, it has been possible to design a criterion for the selection of the two pulse separation times. For the first acquisition, the Δt_0 has to be chosen low enough to guarantee the condition $R_S < 0.5\lambda$ to be satisfied. The extension of the time separation of the second acquisition has not to exceed the following value: $\Delta t_1 = 0.25\lambda/|\sigma_V|$.

A further step forward has been proposed, with the design of a new adaptive multi-step methodology. Also, in this case, the core idea is that in order to optimize the velocity field calculation, only one measurement is not enough. As for the first proposed methodology, a first double-frame single-exposure acquisition is performed to construct a predictor field. However, in the second step, a two-frame two-exposure strategy is selected, which allows an increase of DVR due to the regularization of the particle track along the four exposures and the possibility to evaluate acceleration. The main bottleneck of this kind of acquisition is the appearance of overlapping particles in regions characterized by low displacement. From here, the necessity of a multi-step algorithm arises. The analysis performed on the predictor field, through the creation of N regions with decreasing particle displacement, determines N local pairs $[\Delta t_0, \Delta t_1]$, respectively the inter-frame and intra-frame pulse separation time. After having performed N double-frame double-exposure acquisitions adopting the correspondent pair of $[\Delta t_0, \Delta t_1]$, the correspondent particle tracks are merged and the final time-averaged velocity field is obtained.

The methodology has been preliminary benchmarked on a truncated cylinder test case. Results of the method have been compared to the standard methodologies presented in the literature, having as the time-resolved STB results as a reference. The adoption of the adaptive methodology has proven to be able to recover DVR in the region of low displacement, removing the concerns for overlapping particles. Further studies are planned to determine the most suitable way of practically implementing the concept behind the proposed methodology.

7.1.2. OUTLIER DETECTION BASED ON CONSTITUTIVE EQUATIONS

The availability of dense measurement in a 3D volume permits the exploitation of constitutive equations to determine the presence of outliers in a statistical representation of the flow field. From this perspective, a novel outlier detection criterion based on the physical principle of turbulence transport has been presented. The measured velocity fluctuations are bound to comply with the governing equation of turbulent kinetic energy transport. Based on this, the ratio between the advected turbulent kinetic energy and the production term has been demonstrated as a robust indicator for the presence of outliers. To increase the level of robustness, a median operator has been applied to the production term and an additive term has been inserted in the denominator to avoid the exponential growth of the indicator in laminar regions.

Three datasets have been considered for the benchmark of the methodology: planar PIV around a NACA 0012, tomographic 3D-PTV of a truncated cylinder and 3D-PTV measurements of the near-wake of an Ahmed body by coaxial volumetric velocimetry. The proposed outlier detection principle has been able to detect the edges of the outlier regions. A comparison between the proposed approach and the state-of-the-art universal outlier detector has been carried out. Considering the two optimal thresholds, $r_0^* = 2$ and $\rho_{TT} = 5$, the former yields a significantly higher detection ratio η_d (90% vs 50%) with a comparable and small amount of false positives ($\eta_{fp} < 5\%$).

As mentioned, the approach proposed in this dissertation is able to detect only the contour of an erroneous region, losing physical meaning inside the latter.

7.1.3. DATA ASSIMILATION BASED ON STATE-OBSERVERS

The assimilation of experimental data into the numerical simulation in aerodynamics is quite a new but really active field of research. In this dissertation, a data assimilation framework based on a state observer algorithm has been presented. An integral-proportional approach (DASOPI) has demonstrated the ability to assimilate experimental data into RANS simulations, improving the fidelity of the latter. This analysis is based on an experimental dataset consisting of the time-average 3D velocity field around a simplified car mirror geometry obtained by the use of robotic volumetric PIV. The choice of an experimental test case has been driven by the will to not neglect measurement uncertainties in the assimilation process. However, the boundary conditions have been carefully measured in order to allow maximum compatibility between the simulation and the measurement.

The local response function of the forcing term has been evaluated, confirming the results of Imagawa, Hayase (2010), where the effect is limited to the region close to the forced location and the shape and extent of the affected region depend on the local convection and diffusion. This result confirms the necessity of dense measurement in order to produce a significant effect when assimilated into the numerical simulation. Indeed, the maximum error reduction is obtained at the maximum forcing density ($\gamma = 0.01$), where the error of the assimilated simulation is approximately 25% of the one of the baseline simulation. The beneficial effect of the assimilation is not only detectable in the velocity field but also in the topological features, such as the reattachment point, the arc-vortex and horseshoe vortex axes.

However, the proposed methodology presents several limitations and it is far from being used in a practical scenario. One of the requirements of its application is a dense measurement of the desired velocity field, which arises questions on the necessity of doing the assimilation itself.

7.2. PERSPECTIVES AND RECOMMENDATIONS

In this thesis, several different topics, different aspects of the large-scale PIV measurement technique, have been investigated. three different macro areas can be individuated: acquisition strategy, outlier detection and data assimilation. The level of maturity of the new methodologies proposed varies between the said areas. For this reason, the following developments are envisaged:

- *Multi-step learning measurement strategy*

  In chapter 3 and 4 of this thesis, two novel measuring strategies have been proposed. One of their main novel aspects is the adoption of a multi-step approach. The idea of performing a measurement, analysing it, and repeating the measurement with improved parameters it is not new, however, its algorithmic application is. This concept could be explored even further. During the research phase, it appears clear that the optimal timing strategy is dependent on multiple aspects, such as measured velocity or seeding density. The presented multi-step approach uses a fixed measurement strategy (2 or 4 pulse acquisitions) with variable parameters (mainly the pulse separation time Δt). The use of two or more steps allows for designing an algorithm that selects the proper acquisition strategy based on results or a quick analysis of the previous step. For example, selecting the illumination strategy of the second step between 2 or 4 pulses based on the particle density of the former step.

- *Dynamic analysis for Robotic Volumetric PIV*

  All the results presented in this thesis are limited to the analysis of the time-average velocity field. The nature of the Robotic Volumetric PIV, which employs the volume scanning approach, makes it impossible to extract instantaneous information in the entire measured 3D field, which would be useful to infer the dynamics of the flow. The dynamic component, however, can be recovered by applying mathematical tools such as Proper Orthogonal Decomposition (POD). Cortina-Fernández et al. (2021) presented a methodology to apply the POD to sparse velocity vector obtained by PTV measurements. The ability to use such a technique on Robotic Volumetric PIV measurements depends on the capability of pairing the modes obtained in each cone and reconstructing the entire modal field and should be a topic of further research.

- *Detection of internal regions for the physics-based UD*
  Results from chapter 5 show the ability of the proposed physic-based outlier detection principle to detect the edges of the erroneous region in a time-average velocity field. Due to its Lagrangian approach, the principle becomes unsuited for regions where the velocity vectors are incorrect already upstream of the point of interest. However, methods that treat extended regions of outliers (likely by iterative erosion) can be further developed based on the proposed principle. Furthermore, the same trajectory cannot be considered valid. For this reason, the application of clustering techniques able to detect vector clusters inside the detected boundary by the presented principle is envisaged.

- *Holistic approach for outlier detection from reflection in 3D PIV*
  The methodology presented in this thesis needs as input the time-averaged velocity field to individuate the spurious vectors. The detection mechanism does not consider any information that stems from other steps of the PIV processing, such as the raw images. Reflections, shadows regions or lack of seeding are among the main reasons for the appearance of wrong vectors. It is common that an experienced PIV user, who is fully trained in the measurement technique, is normally able to couple the appearance of an erroneous region of vector to one of the reasons mentioned before just looking at the raw images. It would be insightful to study the possibility of creating a holistic algorithm for outlier detection coupling statistical approaches, such as the Universal Outlier Detection by Westerweel, Scarano (2005) or the one presented in this dissertation, and information coming from the direct observation of the raw images.

This list of possible future developments is the final section of this thesis. The author hopes that it will inspire young researchers to pick up the challenge and continue the development of large-scale PIV.

CURRICULUM VITAE

Edoardo Saredi

07-04-1993	Born in Genova, Italy

Education

2012-2015	Bachelor of Science, Aerospace Engineering Politecnico di Torino (IT) *Thesis*: Aerodynamic model for the morpho-geometric characterization of a bio-mimetic wing
2012-2018	Master of Science, Aerospace Engineering Delft University of Technology (NL) *Thesis*: Extending the velocity range of Robotic Volumetric PIV: Design and application of a multi-Δt approach
2018-2023	PhD Aerospace Engineering, Aerodynamics Delft University of Technology (NL) *Thesis*: Advancements in Large-Scale Volumetric PIV and PTV

Professional experiences

2016	Internship, Aerodynamics Engineer Renault F1 (UK)
2023-Present	Aerodynamicist Alpine F1 (UK)

LIST OF PUBLICATIONS

JOURNAL PUBLICATIONS

1. **Saredi E**, Sciacchitano A, Scarano F (2020) Multi-Δt 3D-PTV based on Reynolds decomposition. *Measurement Science and Technology* 8:084005

2. Kim D, Kim M, **Saredi E**, Scarano F, Kim KC (2020). Robotic PTV study of the flow around automotive side-view mirror models. *Experimental Thermal and Fluid Science* 199:110202

3. **Saredi E**, Ramesh NT, Sciacchitano A, Scarano F (2021) State observer data assimilation for RANS with time-averaged 3D-PIV data. *Computers and Fluids* 218:104827

4. **Saredi E**, Sciacchitano A, Scarano F (2022) Outlier detection for PIV statistics based on turbulence transport. *Experiments in Fluids* 63:14

5. **Saredi E**, Sciacchitano A, Scarano F; A novel multi-step multi-exposure PTV algorithm with adaptive time separation. *In preparation for Measurement Science and Technology*

CONFERENCE PUBLICATIONS AND PRESENTATIONS

1. **Saredi E**, Sciacchitano A and Scarano F (2019) Multi-Δt 3D-PTV based on Reynolds decomposition, *13th International Symposium on Particle Image Velocimetry*, Munich, Germany, July 22-24

2. **Saredi E**, Sciacchitano A and Scarano F (2020) State Observer data assimilation for RANS with time-averaged 3D-PIV data, *3rd Workdhop and Challenge on Data Assimilation & CFD Processing for PIV and LPT*, November 19-20

3. **Saredi E**, Sciacchitano A and Scarano F (2021) Physics-based universal outlier detector for flow statistics, *14th International Symposium on Particle Image Velocimetry*, Illinois, USA, August 1-4

4. **Saredi E**, Sciacchitano A and Scarano F (2022) A Novel Multi-Step Multi-Exposure PTV Algorithm With Adaptive Time Separation, *20th International Symposium on Applications of Laser and Imaging Techniques to Fluid Mechanics*, Lisbon, Portugal, July 11 - 14

BIBLIOGRAPHY

Adatrao, S, Bertone, M, Sciacchitano, A (2021). Multi-Δt approach for peak-locking error correction and uncertainty quantification in PIV. *Measurement Science and Technology* 32.5, p. 054003.

Adrian, RJ (1984). Scattering particle characteristics and their effect on pulsed laser measurements of fluid flow: speckle velocimetry vs particle image velocimetry. *Applied Optics* 23.11, pp. 1690–1691.

Adrian, RJ (1991). Particle-imaging techniques for experimental fluid mechanics. *Annual Review of Fluid Mechanics* 23.1, pp. 261–304.

Adrian, RJ (1997). Dynamic ranges of velocity and spatial resolution of particle image velocimetry. *Measurement Science and Technology* 8.12, pp. 1393–1398.

Adrian, RJ, Westerweel, J (2011). Particle image velocimetry. 30. Cambridge university press.

Agüera, N, Cafiero, G, Astarita, T, Discetti, S (2016). Ensemble 3D PTV for high resolution turbulent statistics. *Measurement Science and Technology* 27.12, p. 124011.

Ahmed, SR, Ramm, G, Faltin, G (1984). Some salient features of the time-averaged ground vehicle wake. *SAE transactions*, pp. 473–503.

Alvarez, R, Christensen, KT (2013). Wall-parallel stereo particle-image velocimetry measurements in the roughness sublayer of turbulent flow overlying highly irregular roughness. *Physics of Fluids* 25.11, p. 115109.

Argyropoulos, CD, Markatos, NC (2015). Recent advances on the numerical modelling of turbulent flows. *Applied Mathematical Modelling* 39.2, pp. 693–732.

Arroyo, MP, Greated, CA (1991). Stereoscopic particle image velocimetry. *Measurement Science and Technology* 2.12, pp. 1181–1186.

Arroyo, MP, Hinsch, KD (2007). Recent Developments of PIV towards 3D Measurements. *Particle Image Velocimetry*. Berlin, Heidelberg: Springer Berlin Heidelberg, pp. 127–154.

Azijli, I, Dwight, RP (2015). Solenoidal filtering of volumetric velocity measurements using Gaussian process regression. *Experiments in Fluids* 56.11, p. 198.

Barros, JM, Christensen, KT (2014). Observations of turbulent secondary flows in a rough-wall boundary layer. *Journal of Fluid Mechanics* 748, R1.

Bastiaans, RJM, Van der Plas, GAJ, Kieft, RN (2002). The performance of a new PTV algorithm applied in super-resolution PIV. *Experiments in Fluids* 32.3, pp. 346–356.

Berg, J van den, Bazuin, R, Jux, C, Sciacchitano, A, Westerweel, J, Water, W van de (2021). The effect of hand posture on swimming efficiency. *Experiments in Fluids* 62.12, p. 245.

Boillot, A, Prasad, AK (1996). Optimization procedure for pulse separation in cross-correlation PIV. *Experiments in Fluids* 21.2, pp. 87–93.

Bosbach, J, Kühn, M, Wagner, C (2009). Large scale particle image velocimetry with helium filled soap bubbles. *Experiments in Fluids* 46.3, pp. 539–547.

Brücker, C (1995). Digital-Particle-Image-Velocimetry (DPIV) in a scanning light-sheet: 3D starting flow around a short cylinder. *Experiments in Fluids* 19.4, pp. 255–263.

Brücker, C (1997). 3D scanning PIV applied to an air flow in a motored engine using digital high-speed video. *Measurement Science and Technology* 8.12, pp. 1480–1492.

Cardano, D, Carlino, G, Cogotti, A (2008). PIV in the Car Industry: State-of-the-Artand Future Perspectives. *Particle Image Velocimetry: New Developments and Recent Applications.* Berlin, Heidelberg: Springer Berlin Heidelberg, pp. 363–376.

Caridi, GCA (2018). Development and application of helium-filled soap bubbles: For large-scale PIV experiments in aerodynamics. PhD thesis. Delft University of Technology.

Cierpka, C, Kähler, CJ (2012). Particle imaging techniques for volumetric three-component (3D3C) velocity measurements in microfluidics. *Journal of visualization* 15, pp. 1–31.

Cierpka, C, Lütke, B, Kähler, CJ (2013). Higher order multi-frame particle tracking velocimetry. *Experiments in Fluids* 54.5, p. 1533.

Cierpka, C, Rossi, M, Segura, R, Kähler, CJ (2011). On the calibration of astigmatism particle tracking velocimetry for microflows. *Measurement Science and Technology* 22.1, p. 015401.

Cierpka, C, Segura, R, Hain, R, Kähler, CJ (2010). A simple single camera 3C3D velocity measurement technique without errors due to depth of correlation and spatial averaging for microfluidics. *Measurement Science and Technology* 21.4, p. 045401.

Cortina-Fernández, J, Vila, CS, Ianiro, A, Discetti, S (2021). From sparse data to high-resolution fields: ensemble particle modes as a basis for high-resolution flow characterization. *Experimental Thermal and Fluid Science* 120, p. 110178.

Da Ronch, A, Panzeri, M, Drofelnik, J, D'Ippolito, R (2020). Sensitivity and calibration of turbulence model in the presence of epistemic uncertainties. *CEAS Aeronautical Journal* 11.1, pp. 33–47.

Davidson, L, Peng, S H (2003). Hybrid LES-RANS modelling: a one-equation SGS model combined with a $k-\omega$ model for predicting recirculating flows. *International Journal for Numerical Methods in Fluids* 43.9, pp. 1003–1018.

De Villiers, E (2006). The potential of large eddy simulation for the modelling of wall bounded flows. PhD thesis. Imperial College of Science, Technology and Medicine.

Duncan, J, Dabiri, D, Hove, J, Gharib, M (2010). Universal outlier detection for particle image velocimetry (PIV) and particle tracking velocimetry (PTV) data. *Measurement Science and Technology* 21.5, p. 057002.

Duraisamy, K, Iaccarino, G, Xiao, H (2019). Turbulence Modeling in the Age of Data. *Annual Review of Fluid Mechanics* 51.1, pp. 357–377.

Ehirim, OH, Knowles, K, Saddington, AJ (2019). A review of ground-effect diffuser aerodynamics. *Journal of Fluids Engineering* 141.2.

Elsinga, GE, Scarano, F, Wieneke, B, Oudheusden, BW van (2006). Tomographic particle image velocimetry. *Experiments in Fluids* 41.6, pp. 933–947.

Fahringer, TW, Lynch, KP, Thurow, BS (2015). Volumetric particle image velocimetry with a single plenoptic camera. *Measurement Science and Technology* 26.11, p. 115201.

Faleiros, DE (2021). Soap bubbles for large-scale PIV. PhD thesis.

Faleiros, DE, Tuinstra, M, Sciacchitano, A, Scarano, F (2018). Helium-filled soap bubbles tracing fidelity in wall-bounded turbulence. *Experiments in Fluids* 59.3, p. 56.

Faleiros, DE, Tuinstra, M, Sciacchitano, A, Scarano, F (2019). Generation and control of helium-filled soap bubbles for PIV. *Experiments in Fluids* 60.3, p. 40.

Ferziger, JH, Perić, M, Street, RL (2020). Computational Methods for Fluid Dynamics. Cham: Springer International Publishing.

Fincham, A, Delerce, G (2000). Advanced optimization of correlation imaging velocimetry algorithms. *Experiments in Fluids* 29.7, S013–S022.

Foures, DPG, Dovetta, N, Sipp, D, Schmid, PJ (2014). A data-assimilation method for Reynolds-averaged Navier–Stokes-driven mean flow reconstruction. *Journal of Fluid Mechanics* 759, pp. 404–431.

Gazi, AH, Afzal, MS (2020). A review on hydrodynamics of horseshoe vortex at a vertical cylinder mounted on a flat bed and its implication to scour at a cylinder. *Acta Geophysica* 68.3, pp. 861–875.

Gibeau, B, Ghaemi, S (2018). A modular, 3D-printed helium-filled soap bubble generator for large-scale volumetric flow measurements. *Experiments in Fluids* 59.12, p. 178.

Godbersen, P, Schröder, A (2020). Functional binning: improving convergence of Eulerian statistics from Lagrangian particle tracking. *Measurement Science and Technology* 31.9, p. 095304.

Grandemange, M, Cadot, O, Gohlke, M (2012). Reflectional symmetry breaking of the separated flow over three-dimensional bluff bodies. *Physical Review E* 86.3, p. 035302.

Hain, R, Kähler, CJ (2007). Fundamentals of multiframe particle image velocimetry (PIV). *Experiments in Fluids* 42.4, pp. 575–587.

Hart, DP (2000). PIV error correction. *Experiments in Fluids* 29.1, pp. 13–22.

Hassan, YA, Canaan, RE (1991). Full-field bubbly flow velocity measurements using a multiframe particle tracking technique. *Experiments in Fluids* 12-12.1-2, pp. 49–60.

Hayase, T (2015). Numerical simulation of real-world flows. *Fluid Dynamics Research* 47.5, p. 051201.

Hayase, T, Hayashi, S (1997). State Estimator of Flow as an Integrated Computational Method With the Feedback of Online Experimental Measurement. *Journal of Fluids Engineering* 119.4, pp. 814–822.

Higham, JE, Brevis, W, Keylock, CJ (2016). A rapid non-iterative proper orthogonal decomposition based outlier detection and correction for PIV data. *Measurement Science and Technology* 27.12, p. 125303.

Hinsch, KD (1995). Three-dimensional particle velocimetry. *Measurement Science and Technology* 6.6, pp. 742–753.

Hinze, JO (1967). Secondary Currents in Wall Turbulence. *Physics of Fluids* 10.9, S122.

Ikhennicheu, M, Druault, P, Gaurier, B, Germain, G (2020). Turbulent kinetic energy budget in a wall-mounted cylinder wake using PIV measurements. *Ocean Engineering* 210, p. 107582.

Imagawa, K, Hayase, T (2010). Numerical experiment of measurement-integrated simulation to reproduce turbulent flows with feedback loop to dynamically compensate the solution using real flow information. *Computers & Fluids* 39.9, pp. 1439–1450.

Jahn, T, Schanz, D, Schröder, A (2021). Advanced iterative particle reconstruction for Lagrangian particle tracking. *Experiments in Fluids* 62.8, p. 179.

Jasak, H (2009). OpenFOAM: Open source CFD in research and industry. *International Journal of Naval Architecture and Ocean Engineering* 1.2, pp. 89–94.

Jeon, YJ, Chatellier, L, David, L (2014). Fluid trajectory evaluation based on an ensemble-averaged cross-correlation in time-resolved PIV. *Experiments in Fluids* 55.7, p. 1766.

Jones, Cassandra, Clifford, Chris, Thurow, Brian S., Mears, Lee, Arora, Nishul, Alvi, Farrukh S. (2018). Two Camera Plenoptic PIV Applied to Shock Wave-Boundary Layer Interactions. *2018 Fluid Dynamics Conference*. Reston, V: American Institute of Aeronautics and Astronautics.

Jux, C (2022). Development of robotic volumetric PIV. PhD thesis. TU Delft.

Jux, C, Sciacchitano, A, Scarano, F (2020). Flow pressure evaluation on generic surfaces by robotic volumetric PTV. *Measurement Science and Technology* 31.10, p. 104001.

Jux, C, Sciacchitano, A, Schneiders, JFG, Scarano, F (2018). Robotic volumetric PIV of a full-scale cyclist. *Experiments in Fluids* 59.4, p. 74.

Kähler, CJ, Kompenhans, J (2000). Fundamentals of multiple plane stereo particle image velocimetry. *Experiments in Fluids* 29.7, S070–S077.

Kalman, RE (1960). A New Approach to Linear Filtering and Prediction Problems. *Journal of Basic Engineering* 82.1, pp. 35–45.

Kato, H, Yoshizawa, A, Ueno, G, Obayashi, S (2015). A data assimilation methodology for reconstructing turbulent flows around aircraft. *Journal of Computational Physics* 283, pp. 559–581.

Keane, RD, Adrian, RJ, Zhang, Y (1995). Super-resolution particle imaging velocimetry. *Measurement Science and Technology* 6.6, p. 754.

Lazar, E, DeBlauw, B, Glumac, N, Dutton, C, Elliott, G (2010). A Practical Approach to PIV Uncertainty Analysis. *27th AIAA Aerodynamic Measurement Technology and Ground Testing Conference*. Reston, Virigina: American Institute of Aeronautics and Astronautics.

Li, Y, Chen, H, Tan, D, Katz, J (2019). On the Effects of Tip Clearance and Operating Condition on the Flow Structures Within an Axial Turbomachine Rotor Passage. *Journal of Turbomachinery* 141.11.

Lignarolo, LEM, Ragni, D, Scarano, F, Simão Ferreira, CJ, Bussel, GJW van (2015). Tip-vortex instability and turbulent mixing in wind-turbine wakes. *Journal of Fluid Mechanics* 781, pp. 467–493.

Loenhout, MTJ van, Kerssemakers, JWJ, De Vlaminck, I, Dekker, C (2012). Non-bias-limited tracking of spherical particles, enabling nanometer resolution at low magnification. *Biophysical journal* 102.10, pp. 2362–2371.

Lübcke, H, Schmidt, S, Rung, T, Thiele, F (2001). Comparison of LES and RANS in bluff-body flows. *Journal of Wind Engineering and Industrial Aerodynamics* 89.14-15, pp. 1471–1485.

Luenberger, DG (1964). Observing the State of a Linear System. *IEEE Transactions on Military Electronics* 8.2, pp. 74–80.

Lynch, KP, Fahringer, T, Thurow, B (2012). Three-dimensional particle image velocimetry using a plenoptic camera. *50th AIAA Aerospace Sciences Meeting Including the New Horizons Forum and Aerospace Exposition.* Reston, V: American Institute of Aeronautics and Astronautics.

Lynch, KP, Scarano, F (2013). A high-order time-accurate interrogation method for time-resolved PIV. *Measurement Science and Technology* 24.3, p. 035305.

Lynch, KP, Scarano, F (2014). Material acceleration estimation by four-pulse tomo-PIV. *Measurement Science and Technology* 25.8, p. 084005.

Maas, HG, Gruen, A, Papantoniou, D (1993). Particle tracking velocimetry in three-dimensional flows. *Experiments in Fluids* 15.2, pp. 133–146.

Malik, NA, Dracos, T (1993). Lagrangian PTV in 3D flows. *Applied Scientific Research* 51.1-2, pp. 161–166.

Martinuzzi, R, Tropea, C (1993). The Flow Around Surface-Mounted, Prismatic Obstacles Placed in a Fully Developed Channel Flow (Data Bank Contribution). *Journal of Fluids Engineering* 115.1, pp. 85–92.

Masullo, A, Theunissen, R (2016). Adaptive vector validation in image velocimetry to minimise the influence of outlier clusters. *Experiments in Fluids* 57.3, pp. 1–21.

Mead, CJ, Wrighton, C, Britchford, K (2015). An Experimental Study of Coaxial Jets Using Acoustic PIV and LDA Methods (CoJeN). *21st AIAA/CEAS Aeroacoustics Conference*. Reston, Virginia: American Institute of Aeronautics and Astronautics.

Melling, A (1997). Tracer particles and seeding for particle image velocimetry. *Measurement Science and Technology* 8.12, pp. 1406–1416.

Menter, F (1993). Zonal Two Equation k-w Turbulence Models For Aerodynamic Flows. *23rd Fluid Dynamics, Plasmadynamics, and Lasers Conference*. Reston, Virigina: American Institute of Aeronautics and Astronautics.

Mertens, C, Rojas Cordero, T de, Sodja, J, Sciacchitano, A, Oudheusden, BW van (2022). Aeroelastic characterization of a flexible wing using particle tracking velocimetry measurements. *AIAA Journal* 60.1, pp. 276–286.

Merzkirch, W (2012). Flow visualization. Elsevier.

Meynart, R (1983). Instantaneous velocity field measurements in unsteady gas flow by speckle velocimetry. *Applied Optics* 22.4, pp. 535–540.

Mitrotta, FMA, Sodja, J, Sciacchitano, A (2022). On the combined flow and structural measurements via robotic volumetric PTV. *Measurement Science and Technology* 33.4, p. 045201.

Mons, V, Chassaing, J-C, Gomez, T, Sagaut, P (2016). Reconstruction of unsteady viscous flows using data assimilation schemes. *Journal of Computational Physics* 316, pp. 255–280.

Nakagawa, M, Michaux, F, Kallweit, S, Maeda, K (2016). Unsteady flow measurements in the wake behind a wind-tunnel car model by using high-speed planar PIV. Fachhochschule Aachen.

Narasimha, R, Prasad, AK (1994). Leading edge shape for flat plate boundary layer studies. *Experiments in Fluids* 17.5, pp. 358–360.

Navon, IM (2009). Data Assimilation for Numerical Weather Prediction: A Review. *Data Assimilation for Atmospheric, Oceanic and Hydrologic Applications.* Berlin, Heidelberg: Springer Berlin Heidelberg, pp. 21–65.

Neeteson, NJ, Rival, DE (2020). State observer-based data assimilation: a PID control-inspired observer in the pressure equation. *Measurement Science and Technology* 31.1, p. 014003.

Nogueira, J, Lecuona, A, Nauri, S, Legrand, M, Rodríguez, PA (2009). Multiple Δt strategy for particle image velocimetry (PIV) error correction, applied to a hot propulsive jet. *Measurement Science and Technology* 20.7, p. 074001.

Nogueira, J, Lecuona, A, Nauri, S, Legrand, M, Rodríguez, PA (2011). Quantitative evaluation of PIV peak locking through a multiple Δt strategy: relevance of the rms component. *Experiments in Fluids* 51.3, pp. 785–793.

Novara, M, Scarano, F (2013). A particle-tracking approach for accurate material derivative measurements with tomographic PIV. *Experiments in Fluids* 54.8, p. 1584.

Novara, M, Schanz, D, Geisler, R, Gesemann, S, Voss, C, Schröder, A (2019). Multi-exposed recordings for 3D Lagrangian particle tracking with Multi-Pulse Shake-The-Box. *Experiments in Fluids* 60.3, p. 44.

Novara, M, Schanz, D, Reuther, N, Kähler, CJ, Schröder, A (2016). Lagrangian 3D particle tracking in high-speed flows: Shake-The-Box for multi-pulse systems. *Experiments in Fluids* 57.8, p. 128.

Oudheusden, BW van (2013). PIV-based pressure measurement. *Measurement Science and Technology* 24.3, p. 032001.

Patankar, SV, Spalding, DB (1972). A calculation procedure for heat, mass and momentum transfer in three-dimensional parabolic flows. *International Journal of Heat and Mass Transfer* 15.10, pp. 1787–1806.

Pereira, F, Stüer, H, Graff, EC, Gharib, M (2006). Two-frame 3D particle tracking. *Measurement Science and Technology* 17.7, pp. 1680–1692.

Persoons, T, O'Donovan, TS (2010). High Dynamic Velocity Range Particle Image Velocimetry Using Multiple Pulse Separation Imaging. *Sensors* 11.1, pp. 1–18.

Prasad, AK (2000). Stereoscopic particle image velocimetry. *Experiments in Fluids* 29.2, pp. 103–116.

Raffel, M, Willert, CE, Scarano, F, Kähler, CJ, Wereley, ST, Kompenhans, J (2018). Particle Image Velocimetry. Cham: Springer International Publishing.

Raffel, M, Willert, CE, Wereley, ST, Kompenhans, J (2007). Particle Image Velocimetry. Berlin, Heidelberg: Springer Berlin Heidelberg.

Raiola, M, Discetti, S, Ianiro, A (2015). On PIV random error minimization with optimal POD-based low-order reconstruction. *Experiments in Fluids* 56.4, p. 75.

Rossi, M, Kähler, CJ (2014). Optimization of astigmatic particle tracking velocimeters. *Experiments in fluids* 55, pp. 1–13.

Saredi, E, Sciacchitano, A, Scarano, F (2020). Multi-Δt 3D-PTV based on Reynolds decomposition. *Measurement Science and Technology* 31.8, p. 084005.

Scarano, F (2013). Tomographic PIV: principles and practice. *Measurement Science and Technology* 24.1, p. 012001.

Scarano, F, Ghaemi, S, Caridi, GCA, Bosbach, J, Dierksheide, U, Sciacchitano, A (2015a). On the use of helium-filled soap bubbles for large-scale tomographic PIV in wind tunnel experiments. *Experiments in Fluids* 56.2, p. 42.

Scarano, F, Ghaemi, S, Caridi, GCA, Bosbach, J, Dierksheide, U, Sciacchitano, A (2015b). On the use of helium-filled soap bubbles for large-scale tomographic PIV in wind tunnel experiments. *Experiments in Fluids* 56.2, p. 42.

Scarano, F, Poelma, C (2009). Three-dimensional vorticity patterns of cylinder wakes. *Experiments in Fluids* 47.1, p. 69.

Schanz, D, Gesemann, S, Schröder, A (2016). Shake-The-Box: Lagrangian particle tracking at high particle image densities. *Experiments in Fluids* 57.5, p. 70.

Scharnowski, S, Bross, M, Kähler, CJ (2019). Accurate turbulence level estimations using PIV/PTV. *Experiments in Fluids* 60.1, p. 1.

Schneiders, JFG, Caridi, GCA, Sciacchitano, A, Scarano, F (2016). Large-scale volumetric pressure from tomographic PTV with HFSB tracers. *Experiments in Fluids* 57.11, p. 164.

Schneiders, JFG, Scarano, F, Jux, C, Sciacchitano, A (2018). Coaxial volumetric velocimetry. *Measurement Science and Technology* 29.6, p. 065201.

Schreck, S, Robinson, M (2007). Wind turbine blade flow fields and prospects for active aerodynamic control. Vol. 42894, pp. 1129–1140.

Schröder, A, Geisler, R, Elsinga, GE, Scarano, F, Dierksheide, U (2008). Investigation of a turbulent spot and a tripped turbulent boundary layer flow using time-resolved tomographic PIV. *Experiments in Fluids* 44.2, pp. 305–316.

Schröder, A, Schanz, D, Bosbach, J, Novara, M, Geisler, R, Agocs, J, Kohl, A (2022). Large-scale volumetric flow studies on transport of aerosol particles using a breathing human model with and without face protections. *Physics of Fluids* 34.3, p. 035133.

Schröder, A, Willert, CE, Schanz, D, Geisler, R, Jahn, T, Gallas, Q, Leclaire, B (2020). The flow around a surface mounted cube: a characterization by time-resolved PIV, 3D Shake-The-Box and LBM simulation. *Experiments in Fluids* 61.9, p. 189.

Sciacchitano, A (2014). Uncertainty quantification in particle image velocimetry and advances in time-resolved image and data analysis.

Sciacchitano, A (2019). Uncertainty quantification in particle image velocimetry. *Measurement Science and Technology* 30.9.

Sciacchitano, A, Scarano, F (2014). Elimination of PIV light reflections via a temporal high pass filter. *Measurement Science and Technology* 25.8, p. 084009.

Sciacchitano, A, Scarano, F, Wieneke, B (2012). Multi-frame pyramid correlation for time-resolved PIV. *Experiments in Fluids* 53.4, pp. 1087–1105.

Sciacchitano, A, Wieneke, B (2016). PIV uncertainty propagation. *Measurement Science and Technology* 27.8, p. 084006.

Sellappan, P, Alvi, FS, Cattafesta, LN (2020). Lagrangian and Eulerian measurements in high-speed jets using Multi-Pulse Shake-The-Box and fine scale reconstruction (VIC). *Experiments in Fluids* 61.7, p. 157.

Sheng, J, Malkiel, E, Katz, J (2008). Using digital holographic microscopy for simultaneous measurements of 3D near wall velocity and wall shear stress in a turbulent boundary layer. *Experiments in Fluids* 45.6, pp. 1023–1035.

Shinskey, F (1996). Process control systems: application, design, and tuning. McGraw-Hill Co. *Inc., New York, NY.*

Simpson, RL (2001). Junction flows. *Annual Review of Fluid Mechanics* 33.1, pp. 415–443.

Soloff, SM, Adrian, RJ, Liu, ZC (1997). Distortion compensation for generalized stereoscopic particle image velocimetry. *Measurement science and technology* 8.12, p. 1441.

Song, X, Yamamoto, F, Iguchi, M, Murai, Y (1999). New tracking algorithm of PIV and removal of spurious vectors using Delaunay tessellation. *Experiments in Fluids* 26.4, pp. 371–380.

Spoelstra, Alexander, Martino Norante, Luigi de, Terra, Wouter, Sciacchitano, Andrea, Scarano, Fulvio (2019). On-site cycling drag analysis with the Ring of Fire. *Experiments in Fluids* 60.6, pp. 1–16.

Stanislas, M, Okamoto, K, Kähler, CJ, Westerweel, J (2005). Main results of the Second International PIV Challenge. *Experiments in Fluids* 39.2, pp. 170–191.

Styan, GPH (1973). Hadamard products and multivariate statistical analysis. *Linear Algebra and its Applications* 6, pp. 217–240.

Sun, B, Ahmed, A, Atkinson, C, Soria, J (2020). A novel 4D digital holographic PIV/PTV (4D-DHPIV/PTV) methodology using iterative predictive inverse reconstruction. *Measurement Science and Technology* 31.10, p. 104002.

Symon, S, Dovetta, N, McKeon, BJ, Sipp, D, Schmid, PJ (2017). Data assimilation of mean velocity from 2D PIV measurements of flow over an idealized airfoil. *Experiments in Fluids* 58.5, p. 61.

Tropea, C, Yarin, AL, Foss, JF (2007). Springer Handbook of Experimental Fluid Mechanics. Ed. by Cameron Tropea, Alexander L. Yarin, John F. Foss. Berlin, Heidelberg: Springer Berlin Heidelberg.

Utkin, Vadim, Guldner, Jürgen, Shi, Jingxin (2017). Sliding mode control in electromechanical systems. CRC press.

Vogel, A, Lauterborn, W (1988). Time resolved particle image velocimetry. *Optics and Lasers in Engineering* 9.3-4, pp. 277–294.

Wang, HP, Gao, Q, Feng, LH, Wei, RJ, Wang, JJ (2015). Proper orthogonal decomposition based outlier correction for PIV data. *Experiments in Fluids* 56.2, pp. 1–15.

Wein, L, Kluge, T, Seume, JR, Hain, R, Fuchs, T, Kähler, CJ, Schmierer, R, Herbst, F (2020). Validation of RANS Turbulence Models for Labyrinth Seal Flows by Means of Particle Image Velocimetry. *Volume 10A: Structures and Dynamics.* American Society of Mechanical Engineers.

Westerweel, J (1994). Efficient detection of spurious vectors in particle image velocimetry data. *Experiments in Fluids* 16-16.3-4, pp. 236–247.

Westerweel, J, Scarano, F (2005). Universal outlier detection for PIV data. *Experiments in Fluids* 39.6, pp. 1096–1100.

Wieneke, B (2013). Iterative reconstruction of volumetric particle distribution. *Measurement Science and Technology* 24.2, p. 024008.

Willert, CE (1997). Stereoscopic digital particle image velocimetry for application in wind tunnel flows. *Measurement Science and Technology* 8.12, pp. 1465–1479.

Willert, CE, Gharib, M (1992). Three-dimensional particle imaging with a single camera. *Experiments in Fluids* 12, pp. 353–358.

Xiao, H, Cinnella, P (2019). Quantification of model uncertainty in RANS simulations: A review. *Progress in Aerospace Sciences* 108, pp. 1–31.

Yakhot, A, Liu, H, Nikitin, N (2006). Turbulent flow around a wall-mounted cube: A direct numerical simulation. *International Journal of Heat and Fluid Flow* 27.6, pp. 994–1009.

Yamagata, T, Hayase, T, Higuchi, H (2008). Effect of Feedback Data Rate in PIV Measurement-Integrated Simulation. *Journal of Fluid Science and Technology* 3.4, pp. 477–487.

Yeh, Y, Cummins, HZ (1964). Localized fluid flow measurements with an He–Ne laser spectrometer. *Applied Physics Letters* 4.10, pp. 176–178.

Zhang, J, Tao, B, Katz, J (1997). Turbulent flow measurement in a square duct with hybrid holographic PIV. *Experiments in Fluids* 23.5, pp. 373–381.

Zhang, Z, Menq, CH (2008). Three-dimensional particle tracking with subnanometer resolution using off-focus images. *Applied optics* 47.13, pp. 2361–2370.